Nuclear Isobar Separation for Penning Trap Mass Measurements at TRIUMF

by

Devin Short

B.Sc., University of Washington, 2012

Thesis Submitted in Partial Fulfillment of the
Requirements for the Degree of
Master of Science

in the
Department of Chemistry
Faculty of Science

SIMON FRASER UNIVERSITY
Spring 2018

Approval

Name:	**Devin Short**
Degree:	**Master of Science (Chemistry)**
Title:	**Nuclear Isobar Separation for Penning Trap Mass Measurements at TRIUMF**
Examining Committee:	**Chair:** Michael Eikerling Professor
	Dr. Corina Andreoiu Senior Supervisor Associate Professor
	Dr. George R. Agnes Supervisor Professor
	Dr. John D'Auria Supervisor Professor
	Dr. Jens Dilling Research Scientist TRIUMF
	Dr. Paul Haljan Internal Examiner Associate Professor Department of Physics
Date Defended:	**April 10, 2018**

Abstract

Nuclear mass values are an important experimental input for research in nuclear theory, astrophysics, and fundamental symmetries. Penning trap experiments such as TRIUMF's Ion Trap for Atomic and Nuclear Science (TITAN) have produced the most precise mass values available for many exotic nuclei. TITAN has measured masses for nuclei with half-lives as short as 8 ms with a relative precision down to 10^{-8}. TITAN has recently installed a multiple reflection time of flight (MR-ToF) mass separator to isolate rare isotopes for mass measurements even when they are obscured by intense isobaric backgrounds.

The MR-ToF can act as a mass filter, producing isobarically pure samples, and it can also operate as a mass spectrometer, destroying a sample to rapidly produce a mass spectrum of an entire ion beam. In the following I provide a pedagogical introduction to the operating principles of the system and report on the results of initial commissioning.

Keywords: Nuclear; isobar; time of flight; mass; spectrometer; separator

Dedication

For Kristina

I'm so excited for all our adventures still to come.

Acknowledgements

I would like to thank my supervisors Corina Andreoiu and Jens Dilling for supporting me at both Simon Fraser University and TRIUMF. In addition to my graduate study in Vancouver, they funded a one year internship for me to participate in initial work on this project with collaborators at Justus-Liebig-Universität-Gießen in Germany.

All of the ion optical designs for components in this work were coordinated by the IONAS group in Gießen, and I benefited greatly from their knowledge and expertise. Christian Jesch participated in the design and construction in Gießen and got the system running after it was shipped to TRIUMF. Wolfgang Plaß came up with the idea for the cubic RFQ switch discussed in section 3.2, and Timo Dickel and Florian Greiner began work on that device before I arrived in Germany. After completing his Ph.D. in the IONAS group, Pascal Reiter took a post-doctoral position at TRIUMF in 2015 and supervised the final stages of the work presented here. Many of the results discussed in chapter 5 would not have been completed for this thesis without Pascal's guidance.

Kyle Leach and Andrew Finlay both worked on this project during and after the transition to TRIUMF. Andrew solved several problems with the C++ code for the simulations discussed in chapter 4 and the appendix. Mel Good made too many expert contributions to list, but I especially appreciate his modular design for the patch panel discussed in section 3.7. Thanks to Carla Babcock for editing early drafts of my thesis, and also to Mikhail Yavor for helping me find an algebra mistake when comparing my derivations in chapter 2 to his textbook.

I especially want to thank the people who have given me the strength and support to consider globe-trotting graduate study, much less complete it. Thanks to Barbara Ballard and Leroy Searle for their careful attention, and to Richard Crooks for extremely generous foresight. Thanks most of all to my parents Jim Short and Judy Moore for their tireless commitment, and to my brother Nick, who's always there when I need him.

Table of Contents

List of Tables

List of Figures

Chapter 1

Introduction

In what follows I report on a multiple reflection time of flight mass spectrometer and separator I helped construct during my master's degree, however this thesis is not only meant to be a technical description of the device we built. My hope is that this document might be provided to a new researcher working with the apparatus as both a conceptual and a practical introduction to the systems I've worked with during my graduate study. In this chapter I develop some background on time of flight mass spectrometry in general as well as the particular experimental challenges which led to the current work. Chapter 2 is an overview of the theoretical problems encountered in multiple reflection systems, including derivations of several beam focusing properties relevant to our spectrometer. The treatment of theoretical concepts in this text is perhaps more detailed than necessary, however there are a number of concepts such as "turnaround time" and "isochronous reflection" that a student like myself may not encounter before solving problems with a multiple reflection spectrometer; if I can save anyone some effort in understanding these concepts in the future I will consider myself a success. Chapter 3 is a detailed description of the spectrometer including electronic subsystems. The cubic ion beam switch described in chapter 3 is a novel device developed by collaborators at Justus-Liebig-Universität Gießen in Germany and implemented for the first time during this work. Nearly all ion optical systems of this complexity require numerical simulations of ion trajectories, and chapter 4 covers simulations of ion motion developed for this project (appendix A provides much of the code required to run the simulations). Chapter 5 discusses the results achieved with our spectrometer as of autumn 2016. The conclusion briefly discusses my particular contributions to this project, summarizes work that's been done since I began writing my thesis, and points to some improvements which could be made in the future.

1.1 A brief history of mass spectrometry in nuclear science

In a lecture published by the Royal Society of London in 1913, English physicist Joseph Thomson claimed that "There can, therefore, I think, be little doubt that what has been

called neon is not a simple gas but a mixture of two gases, one of which has an atomic weight about 20 and the other about 22" [53]. Thomson's assertion meant that a single chemical element actually represented many different substances. This was, according to historian of science Gerald Holton, "... contrary to the most fundamental assumptions of... all chemical thinking in the 19th century" [27, p 552]. The periodic table, established in its modern form only a few decades previous, was a remarkably effective catalog of nearly everything scientists knew about matter, one that's still used to anticipate the properties of undiscovered elements. In fact it's quite odd that the periodic table has proven to be such a useful tool. Again from Holton,

> It is as if a librarian were to put all his books in one heap, weigh them individually, and then place them on a set of shelves according to increasing weight—and find that on each shelf the first book is on Art, the second on Philosophy, the third on Science, the fourth on Economics, and so on. Our librarian may not understand in the least what the underlying explanation for this astonishing regularity is, but if he now discovers on one of these shelves a sequence Art-Science-Economics, he will perhaps be very tempted indeed to leave a gap between the two books on Art and Science and look about for a missing Philosophy book of the correct weight to fill the gap [27, p 421].

It was understood from the outset that explaining the astonishing regularity of the periodic table would require new discoveries and new theories about subatomic structures, but Thomson was talking about something altogether different. Thomson and his colleagues, along with a few radiochemists around the same time, were uncovering a new category of matter hidden not within atoms themselves but within the concept of "element," which had been thought to represent perfectly identical atoms. Language relating this new category to the periodic table was established by Frederick Soddy in the same year as Thomson's lecture,

> Writing a book in 1913 on the chemistry of the radio-elements I got tired of writing "elements chemically identical and non-seperable by chemical methods" and coined the name *isotope*, signifying the same place, to express their nature in the light of the new interpretation of the periodic law. It was clear that the "places" of the latter expressed unit difference of charge in the atomic constitution, a conception which the researches of Moseley... later extended throughout the whole table [54].

With "isotope," Soddy firmly established the idea that each element on the periodic table truly represents a whole stack of different kinds of atoms, each with a different mass but the same electric charge on the atomic nucleus. This idea fundamentally changed our understanding of matter and brought the nascent field of mass spectrometry into its own as a powerful probe of the microscopic world.

Some of the first experiments manipulating particles the size of an atom had been performed only recently, in the 1880's, using cathode ray tubes. There had been significant debate about whether these rays were particles or rather some kind of wave [52]. Thomson received the Nobel prize for his work around the turn of the century, in which he unambiguously resolved the debate from a particle standpoint; when subjected to an electric field under vacuum, cathode rays behaved exactly like bullets under the influence of a gravitational field [52]. By analyzing their trajectories, Thomson correctly determined that cathode rays were in fact streams of particles we now know as electrons. During these investigations, Thomson showed that his cathode ray devices also generated beams of positive particles [52]. This phenomenon had no simple explanation. The scientific community had agreed upon an atomistic view of matter nearly one hundred years before, but by around 1910 there was still no clear picture of atomic structure [27, ch 19]. After exhaustive experiments, Thomson demonstrated that these "rays of positive electricity" where most likely atoms of residual gas which lost some negative charge when cathode rays were fired through a vacuum chamber [53]. Thomson and his colleague Francis Aston rapidly developed better experimental tools which could generate a positive beam, deflect it in static electric and magnetic fields, and focus it onto a photographic plate for analysis. In passing through electromagnetic fields, light, highly charged ions would be deflected more than heavy ions with low charge, and a series of lines representing different masses and charge states would appear in the photographs. The mass lines were reminiscent of colored lines in optical spectroscopy, and spectroscopic terminology was quickly adopted for this new field of study. By 1913, mass spectrometry had developed to the point where Thomson was ready to claim that even a pure beam of neon atoms contained multiple masses, and in the following years many beams of a single element were shown to contain multiple isotopes. In a meeting of the Royal Society in 1921, Soddy reflected on these developments,

> As far back as 1910 I summed up the situation that has been reached in my Annual Report on Radioactivity to the Chemical Society:—
>
> "The recognition that elements of different atomic mass may possess identical chemical properties seems destined to have its most important application in the region of inactive elements, where the absence of a second radioactive nature totally unconnected with the chemical nature makes it impossible for chemical identities to be individually detected. Chemical homogeneity is no longer a gaurantee that any supposed element is not a mixture of several of different atomic weights, or that any atomic weight is not merely a mean number... The absence of simple numerical relationships between the atomic weights becomes a matter of course rather than a surprise." ....
>
> The results we have been listening to have shown what a powerful new weapon has been developed for the detection of isotopes among common ele-

> ments not in actual course of [radioactive] change. Sir Joseph Thomson alluded to chlorine as the most dramatic example of isotopes, but, personally, I consider the discovery of metaneon, an isotope of neon, by himself and Mr. Aston, deserves that title. Coming in 1913, just as the theory of the radioactive isotopes had been [elucidated], it constituted a most striking and suggestive confirmation, in a region of the periodic table remote from that in which the conception originated [54].

Early radiochemistry by Soddy and others dealt with heavy radioactive atoms with masses an order of magnitude greater than Neon, but Thomson and Aston's work had provided independent confirmation that isotopes exist and that they exist throughout the periodic table. The importance of their new laboratory technique was obvious, and experts immediately set about developing more powerful mass spectrometers. A detailed discussion of what came after Thomson and Aston's initial work is not relevant here, but I will summarize two important historical contributions.

First, Arthur Dempster, a Canadian-American physicist working in Chicago, published "A new method of positive ray analysis" in 1918 [14]. Dempster had taken a method developed to measure the charge to mass ratio of the electron and applied it to studies of isotopes. In Dempster's device, ions were accelerated along an electric field and then deflected in a perpendicular magnetic field. The essential difference between Dempster's method and Thomson's was that Thomson had no acceleration stage—after ions were emitted from a source, Thomson used both electric and magnetic fields to deflect the path of the ions in two directions [53]. Thomson's method was useful for spreading a mass spectrum across a photographic plate; in Dempster's spectrometer, ions of a single charge to mass ratio were focused through a narrow slit so that only one isotope could be observed at a time. By tuning the acceleration potential, Dempster could sweep ions of different charge to mass ratios across the slit and construct a mass spectrum by recording the electric potential when ions passed through [14]. This separation technique proved to be far more precise as technology improved and it is still used as a primary mass separation stage in research facilities around the world. Dempster's paper reveals that modern ion sources were also under development by 1918. Thomson and Aston had used radiation or an electric discharge to ionize gases [53, 54] but Dempster reports on two other ionization methods. In one, he placed material on a metal strip and heated the strip until the sample began to emit ions; thermal ion sources operating on the same principle are commercially available today for many applications. Dempster's second ion source involved bombarding a solid sample with electrons moving fast enough to knock ions out of the sample; this is a standard tool in many laboratories today and it's referred to as an electron impact ion source.

The second important publication came from A. E. Cameron and D. F. Eggers at a laboratory in Oak Ridge, Tennessee in 1948 [8]. Cameron and Eggers referred to their spectrometer as a "velocitron", and it did not operate on the same principle as Thomson's

or Dempster's. The velocitron was a purely electrostatic device and it relied on a pulsed beam rather than a continuous stream of ions. In the velocitron, a small cloud of ions was accelerated through an electric potential into a field-free drift tube where it would fly with constant velocity. Every ion in the pulse acquired roughly the same kinetic energy in the electric field, so ions with a small charge to mass ratio would cross the drift tube slower than ions with a high charge to mass ratio. A detector on the opposite side of the drift tube would record the time of arrival for each ion, constructing what we now call a time of flight mass spectrum. The velocitron relied on advanced technology compared to earlier mass spectrometers. Since ions move quickly when accelerated under vacuum, Cameron and Eggers needed circuits that could switch the voltage on an electrode for a few microseconds to generate an ion pulse, and they needed an oscilloscope which could record low intensity voltage pulses from the ion detector which were tens of microseconds long [8]. The velocitron was one of the first time of flight spectrometers, and while timing still represents one of the greatest technological challenges in time of flight mass spectrometry, fast response time is also the primary advantage of the time of flight technique. In their initial report, Cameron and Eggers already reported some success identifying impurities in samples of volatile chemicals whose composition may change during analysis. Today, time of flight spectrometers are used to probe fast chemical reactions, to quickly process large quantities of sample material, and in applications where a sample rapidly decays after it is produced. This thesis is concerned with a new generation of time of flight mass spectrometers designed to analyze samples of radioactive nuclei which decay in milliseconds [43, 48, 58, 60, 15].

The subject of this paper is a mass spectrometer called a multiple reflection time of flight (MR-ToF) spectrometer. The difference between Cameron and Eggers' system and an MR-ToF device is conceptually simple; the drift tube is just made longer. However, instead of extending the drift region with a longer vacuum chamber, switchable electric fields are applied in the drift tube so that ions may be reflected back and forth across the drift region many times before hitting the detector (see figure 1.1). This is analogous to reflecting a laser beam between two mirrors until a shutter is opened at one end. In fact the description of ion beams is so similar to the description of beams of light that as the body of knowledge surrounding ion beams developed it became known as ion optics, and much of the terminology from optics was adopted for ion optical systems. The ion optical description of an MR-ToF spectrometer is not terribly complicated compared to many modern systems like storage rings; we can usually limit ourselves to discussing only static electric fields, there are no internal magnetic fields, and relativistic corrections are not required [61, 63]. In addition, the system developed in this project allows for both destructive measurements of mass spectra and non-destructive separation of single isobars by mass.

While the theoretical barriers to the MR-ToF technique were not particularly high, the technological ones were, and the immediate ancestor of MR-ToF devices (called the reflectron) didn't appear until the 1970's [63, p 115]. MR-ToF spectrometers like the one presented

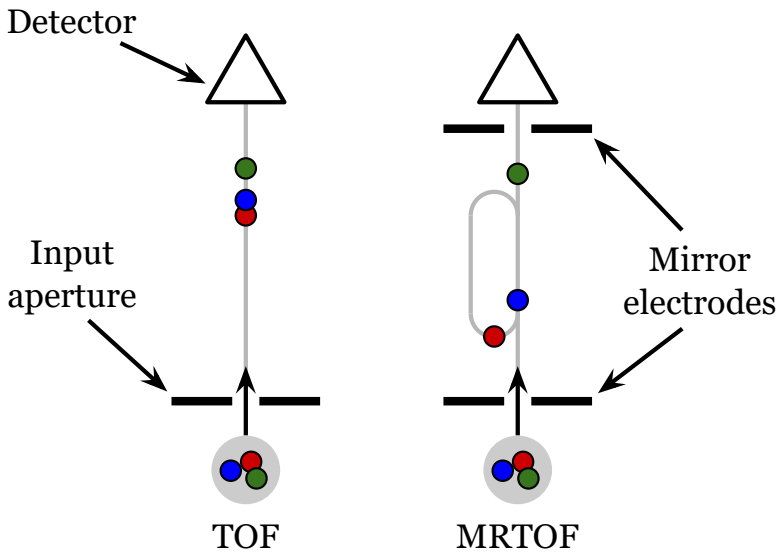

Figure 1.1: In ToF spectrometry (left), ions are accelerated to equal kinetic energy and flown through a field free drift region. Light ions (green) outpace heavy ions (red), and a time of flight spectrum is formed at the detector. In MR-ToF spectrometry (right), additional optics reflect ions across the drift space multiple times, increasing the time of flight and therefore the separation between masses.

here demand advanced electronics which were not readily available until even more recently, and an MR-ToF spectrometer wasn't realized in the lab until around 1990 [62]. A high resolution MR-ToF spectrometer demands that lens and mirror voltages must be switched across hundreds or thousands of volts in less than a microsecond, it requires voltages which are as stable and repeatable as possible, and it must have specialized electronics to switch voltages with precise timing. Overcoming these challenges is an ongoing task, but modern MR-ToF spectrometers can maintain a focused ion beam about a millimeter wide while reflecting ions over a total path length of hundreds of meters [15]. The TITAN MR-ToF spectrometer was designed and constructed by collaborators in the IONAS[1] group at the University of Giessen in Germany. The IONAS group has produced two previous MR-ToF spectrometers, one for nuclear mass measurements at the GSI Helmholtz Center for Heavy Ion Research in Darmstadt [15], and a second, newer setup for analytical chemistry applications [38]. The ion optics in our time of flight mass analyzer are copied from the second IONAS design.

In the last 10 years, MR-ToF separators and spectrometers have become increasingly common at rare isotope beam facilities around the world because they can quickly distinguish small isobarically pure samples from large quantities of background contaminants, making them very well suited for handling short lived nuclei [9]. The power of high preci-

[1]IonenOptik, Nukleare Astrophysik & Struktur

sion MR-ToF spectrometers was made especially clear in 2013, when researchers at CERN[2] made the first direct mass measurements of ^{53}Ca and ^{54}Ca, rare calcium isotopes whose mass values have important consequences for nuclear theory [58]. Our MR-ToF device will be installed in a facility similar to the one in [58], and it will significantly improve nuclear mass measurement capabilities at TRIUMF, Canada's national laboratory for nuclear and particle physics (see section 1.3).

1.2 The role of mass measurements

Mass measurements have been an essential component of nuclear science since the discovery of the nucleus. As Soddy noted in 1910, isotopes of a chemical element are inseparable by chemical means and must be distinguished by their mass [54]. We now know that the protons and neutrons (collectively known as *nucleons*) inside the nucleus have very similar masses and that electrons are about 2,000 times lighter than the nucleons, so when we talk about separating isotopes by mass what we really care about is the nucleus. When we view nuclei as made up of protons and neutrons, nuclear structure becomes more clear; each nucleus has so many protons and so many neutrons, so we can chart all the different nuclei by laying them out according to their nucleon numbers. This is called the chart of the *nuclides*—the nuclear scientists' periodic table. On the chart of nuclides, chemical elements and their isotopes with equal proton number are rows, while nuclei with an equal number of neutrons, called *isotones*, lie on the columns. Nuclei with the same mass number, or total number of nucleons, are called *isobars* and they run along diagonals of the chart (see figure 1.2).

Nuclear scientists today are in a position similar to chemists' at the end of the 19th century. The chart of nuclides and the data behind it represents a vast catalog of our knowledge about matter in the universe, but we lack a consistent unifying theory that will tell us about the properties of all nuclear matter. We have many theoretical tools which allow us to describe features of the chart quite well, but they are either applicable in only a particular region of the chart or they describe an overall trend with many exceptions [28].

Measuring nuclear masses turns out to be one of the fundamental tests of nuclear models because the nucleus is a bound many-body system. From Einstein's equation $E = mc^2$, we know that any bound system is lighter than the sum of its unbound parts because we have to spend energy to break up the system. Nuclei are so small and tightly bound that binding energy significantly affects the total mass of a nucleus. One of the most dramatic examples is Iron 56, which has the highest binding energy per nucleon. ^{56}Fe has a total mass of about 52,000 MeV/c^2 and its binding energy is around 500 MeV, so the binding energy is equivalent to almost one percent of the nuclear mass [57]. Any modern theory about how nucleons interact has to account for such a large effect, so nuclear masses are

[2]The European Organization for Nuclear Research, Geneva, Switzerland

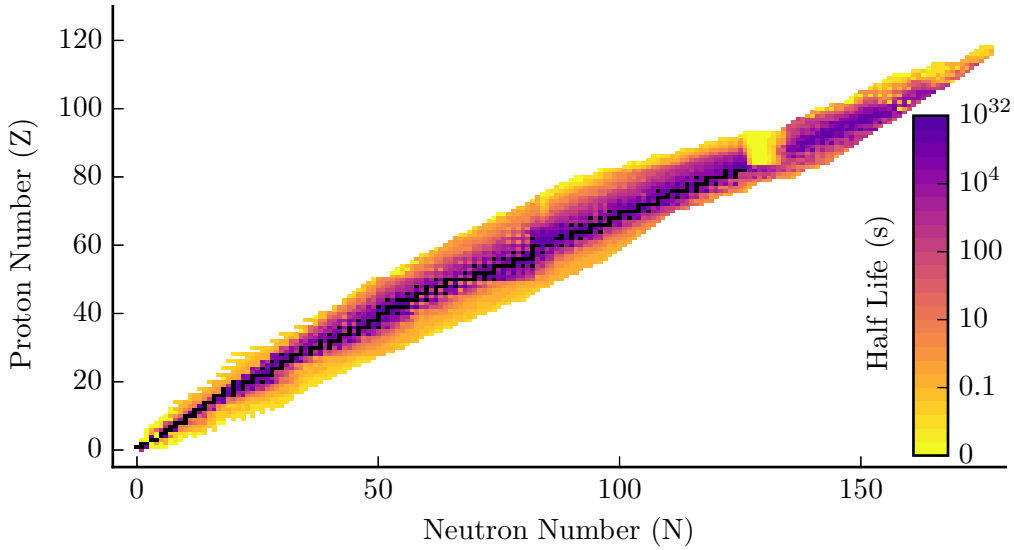

Figure 1.2: Chart of nuclides with half-life indicated by a color scale (stable isotopes are black). Proton number Z increases on the vertical and neutron number N increases on the horizontal. Rows represent isotopes of chemical elements and isobars are diagonals crossing the line of stable nuclides. Data from NuBase 2012 [2].

often a good way to check theoretical calculations. This discussion is obviously relevant if one sets out to understand the nucleus, however nuclear masses and binding energies inform our understanding of many systems.

Researchers in other fields had identified the profound impact nuclear science would have on their work even before the 1921 meeting of the Royal Society in which Soddy declared the importance of Thomson and Aston's discoveries. By 1920, the preeminent astronomer Arthur Eddington was convinced that the source of energy in stars was some kind of nuclear reaction:

> A star is drawing on some vast reservoir of energy by means unknown to us. This reservoir can scarcely be other than the sub-atomic energy which, it is known, exists abundantly in all matter.... Certain physical investigations of the past year... make it probable to my mind that some portion of this sub-atomic energy is actually being set free in stars. F. W. Aston's experiments seem to leave no room for doubt that all the elements are constituted out of hydrogen atoms bound together with negative electrons.... But Aston has further shown conclusively that the mass of the helium atom is less than the sum of the masses of the 4 hydrogen atoms which enter into it.... Now mass can not be annihilated, and the deficit can only represent the mass of the electrical energy set free in the transmutation. We can therefore at once calculate the quantity of energy liberated when helium is made out of hydrogen. If 5 per cent. of a star's mass

> consists initially of hydrogen atoms, which are gradually being combined to form more complex elements, the total heat liberated will more than suffice for our demands, and we need look no further for the source of a star's energy [20].

Eddington identifies nuclear mass measurements as one of the first proofs that nuclear reactions form the heart of the stars, and these efforts remain important to our understanding of the cosmos [26, ch 19]. One of the most active research areas in modern nuclear astrophysics is the search for the *r-process*, one of two processes believed to produce most elements heavier than iron. The r-process is a rapid nuclear reaction which occurs in explosive environments where nuclei are able to capture many free neutrons and then beta-decay. These reactions may occur in supernovae or neutron star mergers but the actual site of the r-process is unknown, and many of the nuclei involved cannot yet be produced in the lab [4]. Precise measurements of all masses relevant to the r-process would enable researchers to calculate the energy requirements and output of an r-process event, leading to a better understanding of stellar evolution and the source of the elements we find on Earth.

Nuclear processes help us understand the life cycle of the stars, objects living on scales so large they challenge the imagination, but we find that they are also useful probes of Standard Model physics—laws governing nature at the smallest scales in the known universe. Nuclear scientists contribute to standard model tests in a variety of ways, but one important parameter that can be determined entirely from nuclear mass measurements is the *Q-value* of a radioactive transition. The Q-value is the energy emitted when an unstable nucleus decays. It can therefore be determined from the difference in mass between a mother and daughter nucleus; the mass difference had to be carried away either as massive particles or as electromagnetic radiation. The total energy emitted, the Q-value, is then the kinetic energy of the particles together with the energy of the radiation. By measuring the mass difference between parent and daughter nuclei, researchers provide constraints on what happens during radioactive transitions. Active research areas requiring better Q-values include a determination of the neutrino mass, the search for neutrinoless double beta-decay, testing the unitarity of the Cabibo-Kobayashi-Maskawa (CKM) quark mixing matrix, and verification of the conservation of the vector current (CVC) hypothesis for heavy nuclei [4].

1.3 TRIUMF and ISAC

A great deal of the experimental work in modern nuclear science is carried out by collaborations at accelerator facilities like TRIUMF. The centerpiece of the TRIUMF experimental program is a cyclotron which is typically used to produce rare isotopes for research into nuclear physics, astrophysics, fundamental interactions, and nuclear medicine. Accelerator methods are generally not selective techniques for producing radioactive ions; large facilities are typically designed to produce as many isotopes as possible to accommodate whatever needs might arise in the experimental community. The method employed to produce ra-

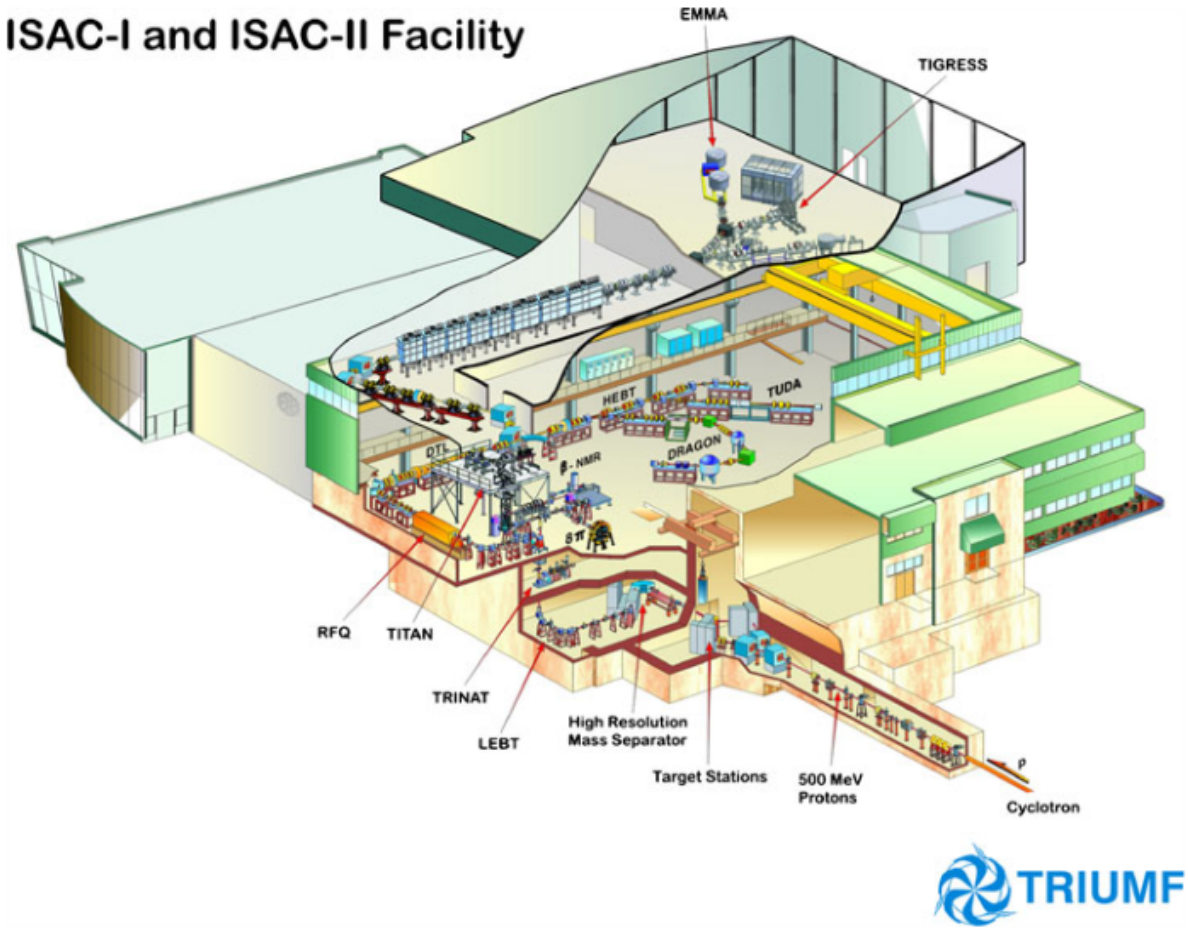

Figure 1.3: A schematic of ISAC at TRIUMF, showing the 500 MeV input beam from the cyclotron, a mass separator similar to Dempster's spectrometer in section 1.1, and various experimental facilities including TITAN. Reprinted from *Hyperfine Interactions*, 225, J. Dilling, R. Krücken, G. Ball, "ISAC overview," 1-8, Copyright (2014), with permission from Elsevier.

dioactive beams at TRIUMF is called Isotope Separation On-Line (ISOL), and TRIUMF's ISOL facility is the TRIUMF Isotope Separator and Accelerator (TRIUMF-ISAC). At ISAC, hydrogen ions are injected into the world's largest cyclotron [3], accelerated to 500 MeV kinetic energy, extracted as protons, and fired into a solid target. A large fraction of the beam energy is dissipated, producing an intensely radioactive plasma in the target. Radioactive nuclei diffuse out of the hot target and are emitted as neutral atoms with thermal energies (tens or hundreds of eV), so they must be ionized and re-accelerated for transport to experiments [1]. After ionization, a magnetic mass separator similar to the one introduced by Dempster selects ions of interest which are then delivered to apparatus in the ISAC experimental halls.

1.4 TITAN

Among the ISAC experiments is TRIUMF's Ion Trap for Atomic and Nuclear science (TITAN), which performs high precision mass measurements of rare isotopes [17, 18, 36]. TITAN currently consists of three main components: a radio frequency quadrupole (RFQ) beam cooler and buncher[3], an electron beam ion trap (EBIT) for breeding highly charged ions (HCI), and a Penning trap for the mass measurements themselves. Mass measurements on HCI are more precise but charge breeding is only possible with ions whose half-life is longer than the charge breeding time; the TITAN platform is set up to allow experimenters to bypass the EBIT for short-lived ions. Most of the TITAN beamline is or will be filled with ion optics, so the MR-ToF mass separator has been designed for an extension of the existing vacuum system which will couple to a pair of open ports (see figure 1.4).

TITAN is designed as a Penning trap experiment, so the parameters of each component are largely dictated by the requirements for high precision in the measurement Penning trap. A Penning trap is a set of cylindrically symmetric electrodes placed in a strong homogeneous magnetic field which is parallel to the beam axis (see figure 1.5). Cyclotron motion around the magnetic field confines ions in the transverse direction while a static electric potential traps ions in the longitudinal direction. To trap ions, the static potential is reduced, an ion bunch is injected into the trap, and the static potential is raised before ions leave the trapping region. At TITAN, mass measurements are performed using the time of flight ion cyclotron resonance (ToF-ICR) technique [23]. In ToF-ICR, trapped ions are driven with a radio frequency signal applied to the central trap electrode. When the ions are driven at their cyclotron frequency, energy from the driver signal will be absorbed into resonant ion motion. The high radial kinetic energy absorbed at resonance may be converted into longitudinal kinetic energy by ejecting ions out of the trap and into a magnetic field gradient

[3]The ion trapping community frequently refers to these devices simply as "RFQs" however they are not to be confused with RFQ linear accelerators, which sometimes go by the same name (as in figure 1.3).

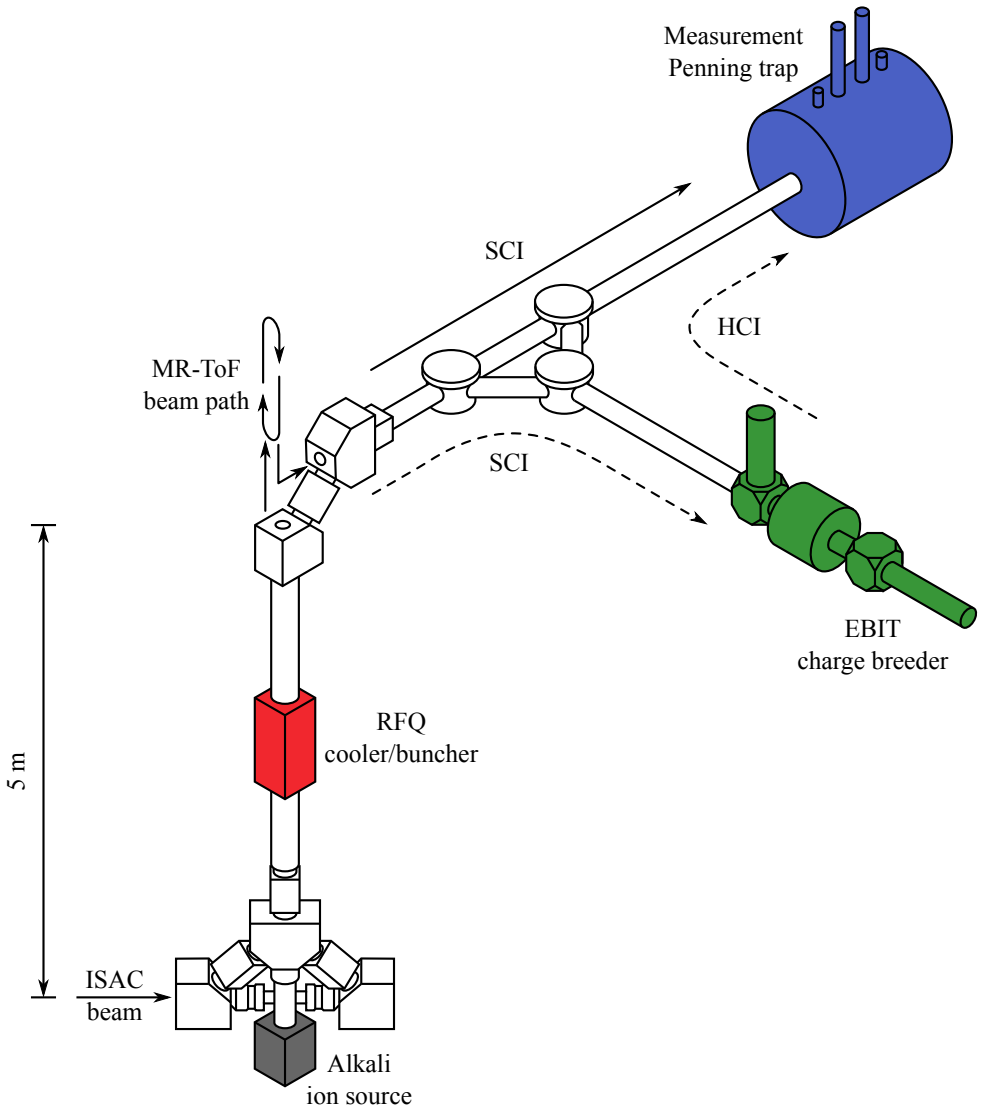

Figure 1.4: A schematic of the TITAN experiment. ISAC delivers a continuous beam of singly charged ions to the RFQ, which provides a cooled and pulsed beam to downstream components. After the RFQ, SCI may be passed directly to the Penning trap for mass measurements or they may be charge bred in the EBIT beforehand and delivered to the Penning trap as highly charged ions (dashed beam path). An ion source for alkali elements is used for diagnostics when TITAN is not taking beam from ISAC. The MR-ToF mass separator is not yet installed on the beamline, but the multiple reflection beam path is shown in its future position.

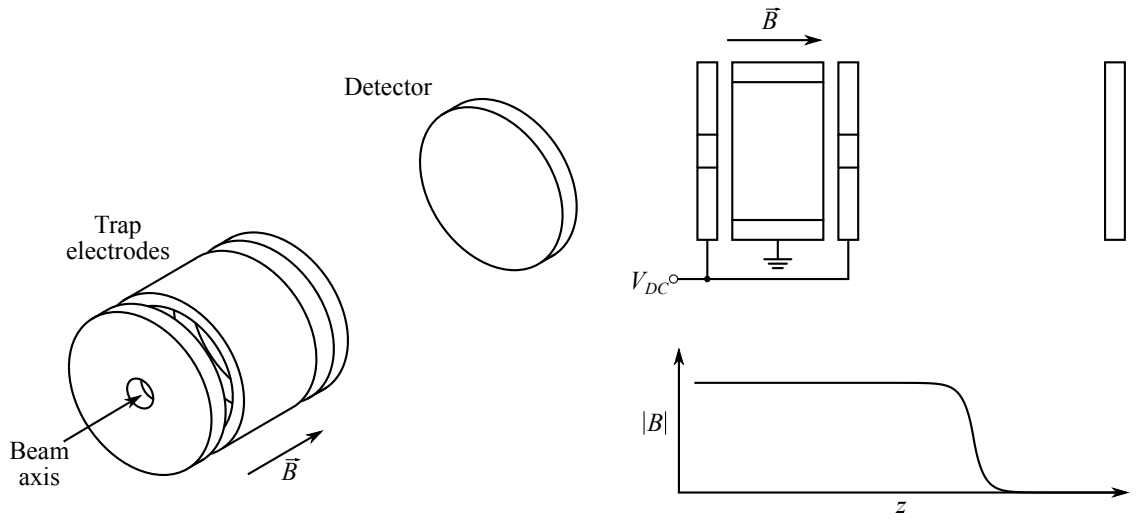

Figure 1.5: Schematic of a cylindrical Penning trap with a detector for ToF-ICR mass measurements. The TITAN Penning trap is cylindrically symmetric but the electrodes are hyberbolas of revolution rather than anular as shown here. The figure is not to scale; the inner volume of a Penning trap is usually a few cubic centimeters, while the distance from trap to detector is typically more than a meter when a superconducting solenoid is used to apply the magnetic field.

(see figure 1.5). The closer the driving frequency is to the cyclotron frequency of the ions, the faster the ion bunch will travel after it leaves the magnetic field. A mass measurement is therefore taken by repeatedly loading the trap with ions of interest, pumping the stored ions at different excitation frequencies, and ejecting them to a detector outside the magnetic field. The ion cyclotron frequency is measured by finding the frequency which minimizes the time between ejection and detection. The mass is then determined from

$$m = \frac{qB}{\omega_c} \tag{1.1}$$

Where m is the ion mass, q is its charge, ω_c is the cyclotron frequency of the ion in the trap, and B is the magnetic field strength in the trap. A complete mass measurement requires a series of ToF spectra taken both for the ion of interest and a calibrant of well known mass; masses must be measured relative to a calibrant in order to control for systematic uncertainties like drifts in the magnetic field around the Penning trap.

The great advantage of Penning trap ToF-ICR mass measurements is their high precision. The relative uncertainty in the mass is not a straightforward calculation, but a widely applicable formula has been determined [5]:

$$\frac{\delta m}{m} \simeq \frac{1}{T\omega_c N^{\frac{1}{2}}} = \frac{m}{TqBN^{\frac{1}{2}}} \tag{1.2}$$

where T represents the amount of time ions experience RF excitation in the trap and N is the number of measured ions. From equation 1.2, it's clear that increasing the in-trap excitation time, the charge state of the ions, the magnetic field, or the number of measurements will increase the precision of a mass measurement. These quantities are limited in significant ways; excitation time is often limited by the half-life of the ion of interest; the charge state of the ion is ultimately limited by the charge of the nucleus, however the actual charge state of measured ions is usually limited by experimental apparatus [36]; and the strongest achievable magnetic fields are in the neighborhood of 10 Tesla, however magnets generating such strong fields are prohibitively expensive (the TITAN Penning trap magnetic field is 3.7 T); finally, the number of measured ions is typically limited by the rate at which a facility can produce rare isotopes and the amount of beam time provided for a particular experiment. At TITAN, 100 measurements of singly charged 100 amu ions would yield a relative uncertainty of approximately one part per million for excitation times below 100 ms. A few thousand measurements with a charge state of 48 and the same excitation time would bring the uncertainty down to a few parts per billion [49].

The TITAN RFQ and EBIT are designed as infrastructure for the Penning trap. ISAC delivers a continuous beam of singly charged ions (SCI) to the TITAN experiment at about 20 keV kinetic energy. The Penning trap requires a small sample of low-energy ions, so the TITAN RFQ stores ions from ISAC in a gas filled linear trap to cool them and deliver a pulsed beam to the TITAN platform [36]. The TITAN RFQ relies on buffer gas cooling; the 20 keV ISAC beam is slowed in an electric potential and injected into a volume filled with a neutral gas which has high ionization potential (typically Helium). A trapping potential is established in the gas-filled region and ions settle into the bottom of the potential as they lose energy through repeated collisions with the buffer gas. At regular intervals, the downstream end of the trapping potential is lowered and a small cloud of cooled ions is emitted from the RFQ.

RFQs are common for cooling and bunching beams, but TITAN is currently the only Penning trap facility in the world which operates an EBIT to "breed" highly charged ions for precision mass measurements [36]. The EBIT is a second cylindrical ion trap where ions are stored and exposed to an intense electron beam. The electron beam both attracts positive ions and knocks bound electrons out of them, confining ions radially and increasing their total positive charge. After charge breeding, ions are extracted from the EBIT and delivered to the Penning trap. Charge breeding increases the mass measurement precision but it heats the ions and reduces beam quality. It is also more difficult to handle ions in high charge states because ion-ion interactions are stronger and HCI are more likely to ionize residual gas in the vacuum system. These sacrifices are worthwhile when very high charge states are accessible. TITAN has already performed mass measurements on ions with charge states up to 22+ [36], increasing the theoretical precision on mass values for those isotopes by more than an order of magnitude.

The precision of a Penning trap mass measurement is highest when only one ion is present in the trap at any given time. The ToF measurement is obviously less certain if a cloud of multiple ions takes some time to completely exit the trap, but ion-ion interactions also shift both the resonant excitation frequency and the eigenfrequencies of motion in the trap [6]. The RFQ is therefore operated such that, on average, one ion reaches the measurement Penning trap per ToF-ICR measurement. The EBIT also substantially improves measurement precision, but there is still a major obstacle preventing TITAN from performing high precision mass measurements on a number of interesting nuclides: isobaric contamination. Isobaric contaminants can swamp signals from ions of interest even when only one ion is present per ToF-ICR cycle. This is because each ion produces its own ToF-ICR resonance and resonances from isobars typically overlap. If the contaminant isobar is much more common than the ion of interest (as is often the case), the contaminant can completely obscure the ToF-ICR resonance from the ion of interest. Even when an interesting resonance is visible above contaminant signals, fitting the resonance curve from multiple species creates statistical uncertainties which reduce measurement precision.

Isobaric contamination represents a significant challenge to Penning trap mass measurements primarily because it's nearly impossible for an ion source to produce only a single atomic species. Ion sources in common use at TRIUMF include a Rhenium surface ion source and a forced electron beam induced arc discharge (FEBIAD) ion source. In the surface ion source, neutral atoms diffusing from the target condense onto a metal surface hot enough to desorb and ionize them. In the FEBIAD, neutral isotopes are ionized in an electric arc, forming a plasma. These sources are not selective; a heated surface with a low work function will emit ions in a wide spectrum, particularly alkali metals which have low ionization energies; plasma sources like a FEBIAD ionize every particle passing through the plasma and they additionally generate ions with a variety of charge states, further complicating species selection. The only selective ion source available at ISAC is a resonant ionization laser ion source [40]. In resonant laser ionization, radioactive isotopes are exposed to several laser beams simultaneously and the laser frequencies are chosen to excite a specific element in steps until it's ionized. This technique is highly selective but it can only ionize isotopes which have an appropriate set of excited states.

After ionization, the ISAC mass separator is the only mass selection stage before the beam is delivered to TITAN. The mass separator typically isolates a single mass number, so any isobars ionized with the isotope of interest will end up in the TITAN system. This is such a common problem that it warrants an additional set of ion optics dedicated to isobar separation. As a typical example, the TITAN collaboration has already secured beam time to do a series of mass measurements on neutron rich Indium isotopes in the mass range 130–135 [37]. Nuclear mass measurements in this region are important for astrophysicists studying the r-process in supernovae. ^{133}In is produced at ISAC with a copious ^{133}Cs background. As shown in figure 1.6, more than 10^8 Cesium ions are produced for every Indium

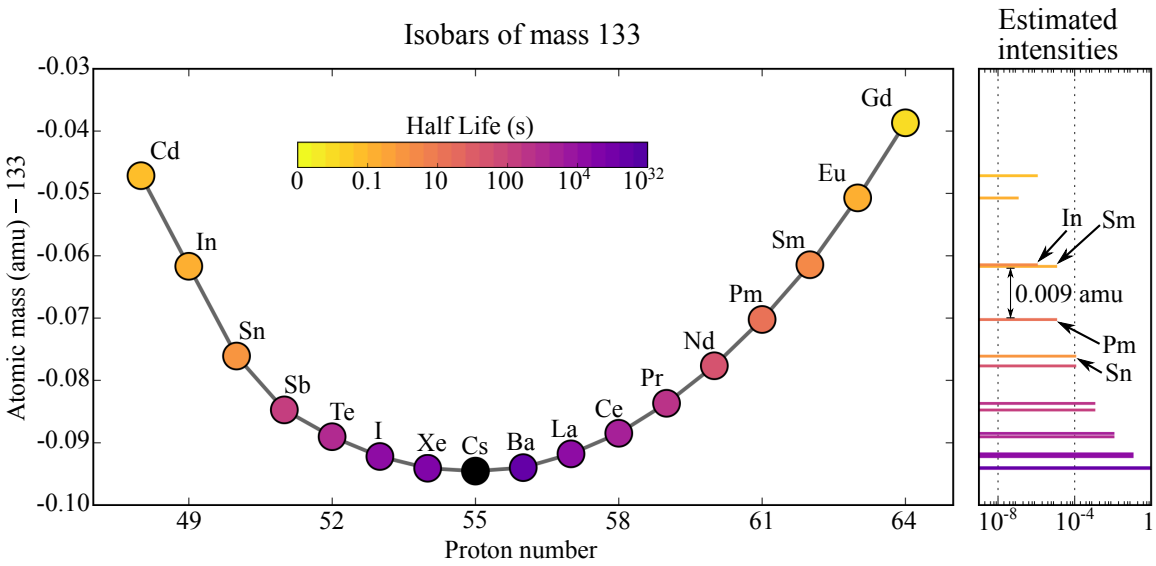

Figure 1.6: Isobars of mass 133 with half-lives indicated by the same color scale as in figure 1.2. The plot on the right shows estimates of the relative intensity of each isotope coming out of the target whose half-life is greater than 10 ms. Intensities are estimated as 10^{-p} where p is the number of protons from stability minus 1. This rule of thumb for relative intensities is supported by measured yields at ISAC [19]. Note that Cs is not included in the intensity estimate because no data is currently available for yields of stable isotopes.

ion of interest [19]. Since the mass difference between these isobars is only one part in 4,000 [57], a ^{133}In mass measurement at TITAN will require a new high resolution mass separator which is capable of handling ion currents high enough to separate hundreds of ions out of tens of millions in a reasonable amount of time. An MR-ToF system fits the bill, and the goal of this project is to commission an MR-ToF device for the TITAN collaboration.

The TITAN MR-ToF system has two operational modes; it can perform high resolution mass spectrometry, which involves a destructive measurement producing a time of flight spectrum of all ions in the system, or it can operate as a mass separator, recapturing a small section of the ToF spectrum and transporting those ions (preferably a single species) to either the EBIT or the measurement Penning trap. The destructive ToF spectra are essentially beam diagnostics; they provide a quick snapshot of the beam contents. These diagnostics will also provide the first direct measurements of total mass spectra for re-accelerated ion beams at ISAC. Currently ISAC yields are measured indirectly by depositing the beam on a target and collecting radiation. These techniques are highly developed but there is currently no way to measure yields of stable nuclei. The new MR-ToF spectrometer will hopefully provide independent confirmation of the relative intensities of radioactive ions as well as the first measurements of relative intensities for stable ions. There are a number of subsystems involved in complete operation of the system, and commissioning all of them is beyond the scope of a single master's project. My work has focused on initial construction

and commissioning of our spectrometer so this thesis is limited to mass spectrometry rather than mass separation.

Chapter 2

Time of flight mass spectrometry

In many respects, a multiple reflection time of flight spectrometer (referred to simply as "an MR-ToF" from here on) is no different than any other time of flight setup. In general, time of flight measurements on trapped ions can be broken down into four stages: preparation, acceleration, drift, and detection. During preparation, particles are ionized and accumulated in such a way that their initial energy and position are well defined. After preparation, ions are accelerated or *kicked* into a drift space. This process sets the kinetic energy of ions in flight and starts a clock for the time of flight measurement. Since they all have the same kinetic energy, ions with different mass to charge ratios will drift apart in flight. When ions hit a detector, they typically produce current pulses which can be read out into a time of flight spectrum.

In order to distinguish between two masses in a ToF spectrum, ion bunches should be separated by at least the time width of a pulse coming out of the detector. Since ion bunches with different mass to charge ratio get farther apart the longer they fly through a spectrometer, one of the primary design goals for a ToF system is to produce the narrowest possible peaks at the longest possible flight time. Ion bunches will be well defined in time when they're prepared in a small cloud (see section 2.1) and when the ion optics create an accurate image of the initial population (see sections 2.2 – 2.5), however there is a fundamental lower limit to the width of a bunch (see section 2.6). The figure of merit for this process is the *mass resolving power*, which is discussed in section 2.7.

2.1 Sample preparation

At an ISOL facility, ionization occurs near the production target, and at TRIUMF-ISAC ions are then delivered to a magnetic mass separator capable of selecting a single atomic number out of a diverse ion population. A description of the targets, ion sources, and mass separator used at ISAC is provided in [7]; this section focuses on what happens to the continuous ion beam after it's delivered to the TITAN platform.

Ion trapping requires an ion bunch with a limited spatial and time width. This can be achieved by chopping a continuous beam with a rotary aperture or a pulsed potential, however this is not an acceptable solution for exotic nuclei because many ions of interest would be lost. A rare ion beam must be accumulated in a buncher and passed downstream to a trap in such a way that the ion bunches are small and have a energy spread which downstream optics can accept. The goal is for an ion bunch to occupy the smallest possible volume in *phase space*, a six dimensional Hilbert space consisting of the coordinate dimensions (x, y, z) and the particle momenta (p_x, p_y, p_z). Under conservative forces with time independent potentials, the phase space volume of a set of particles is conserved; this is Liouville's theorem (see [63], section 1.3.3). In that case there's a trade off: either one can have an ion bunch with a small spatial volume or one can have an ion bunch with well defined momentum, but not both simultaneously.

One way to circumvent Liouville's theorem is to place ions of interest in a system whose phase space volume is extremely large but which allows the ions to migrate into a small section of the larger volume. This is the case when ions are trapped in a vessel filled with buffer gas, placing them in contact with a very large number of neutral particles whose thermal energy is lower than the average energy of the initial ion population. The average energy and the energy spread of the ions is reduced during repeated collisions with neutral particles; this is referred to as ion "cooling" and it reduces the volume of the ion bunch in momentum space. As ions cool they also occupy a smaller and smaller spatial volume near the potential minimum of the trap, but the overall phase space volume is conserved when one takes the neutral particles into account. The buffer gas must be chosen such that its mass is below the typical ion mass (otherwise ions tend not to lose momentum to the gas) and the gas should have a high ionization potential (otherwise ions are lost to charge exchange during collisions). Helium is a common choice of buffer gas, and it's used on the TITAN platform. After an ion bunch has reached the thermal energy of the buffer gas, the trapping potential is removed and ions are transported out of the gas filled region into experimental apparatus where the ambient pressure is typically very low. Liouville's theorem applies to the ion cloud as an isolated system once it leaves the buffer gas because there are few collision partners at low pressure, so the phase space volume of the ion bunch is conserved after cooling.

The traps used to cool ions in buffer gas are usually linear Paul traps or radio frequency quadrupoles (RFQs). In a linear Paul trap, a quadrupolar electric field is established between two endcaps perpendicular to the axis of the quadrupole. A true quadrupole field is only established by using electrodes whose surfaces are hyperbolic, however in practice a wide variety of electrode geometries produce fields which are sufficiently quadrupolar for transporting and trapping ions [12]. One simple configuration consists of four cylindrical electrodes perpendicular to flat apertures where ions enter or exit the trap (see figure 2.1). Ions are trapped longitudinally between the endcap electrodes and radial confinement is

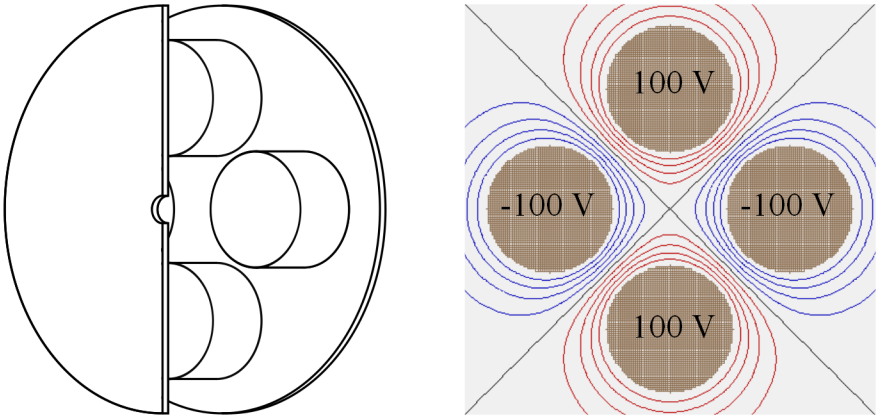

Figure 2.1: Left: a schematic of a Paul trap. Electrodes in this configuration are typically stainless steel. One aperture is cut away to show quadrupole geometry. Right: a quadrupole electric potential produced in this geometry with the endcaps at ground potential (no longitudinal trapping field is applied). Realistic electric potentials for a Paul trap in the TITAN MR-ToF are shown in figure 2.2.

achieved by rapidly rotating the quadrupole field about its axis. Rotation is established by applying two signals of opposite phase which switch the polarity of the rods at radio frequencies (hundreds of kHz to a few MHz). RF signals are typically sinusoidal or square waves depending on the method used to generate the signal (see section 3.6). Ion traps referred to as RFQs are similar to Paul traps but they consist of a long set of quadrupole electrodes which also apply a longitudinal gradient suitable for transporting ions to a particular location where a trap or series of traps is established. This provides a larger gas volume in which ions can cool before settling into a small trapping region (see figure 2.3).

Control and trapping of ions in gas filled RFQs is robust under a variety of operating conditions but the RF signals must be tuned to transport ions of a particular charge to mass ratio. The conditions for stable transport are calculated by examining ion motion in an evacuated RFQ. Ion trajectories in this case are analytic, consisting of a micro-scale oscillation in response to the RF field and larger scale or *secular* motion averaged over an RF period. A detailed description of the theory is provided by Dawson in [12, ch 2–3], a few results from that text are presented here.

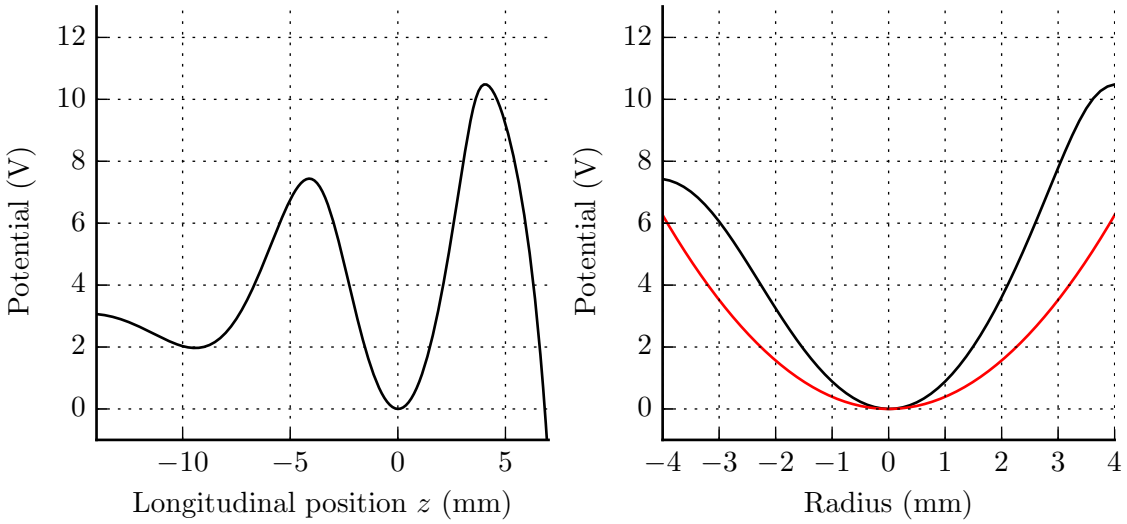

Figure 2.2: Electric potential around a Paul trap near the TITAN MR-ToF mass analyzer. Left: simulated longitudinal potential. The trap is asymmetrical because the apertures have different diameters (see sections 3.3 and 4.5 for details). Right: pseudopotential (red) calculated from equation 2.7 shown over the longitudinal potential (black). The pseudopotential is calculated for singly charged ^{133}Cs ions and a 120 V zero-to-peak RF signal at 1.15 MHz.

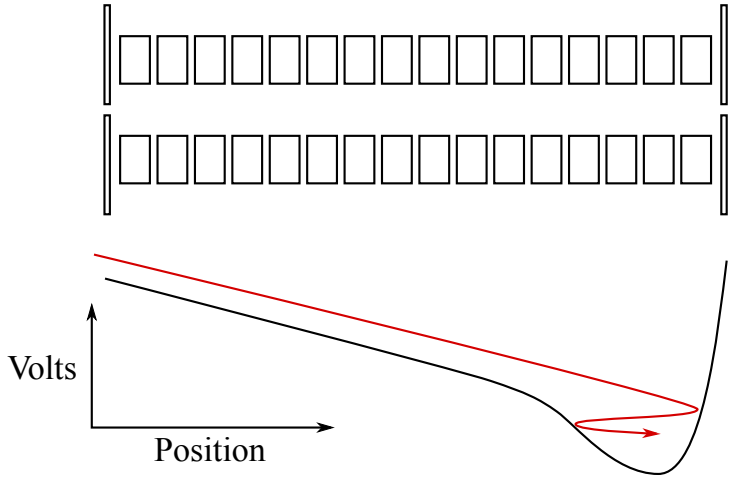

Figure 2.3: Top: a cross section of an RFQ ion cooler. This geometry relies on segmented stainless steel rods. In this case each segment has a different central potential about which the quadrupole field oscillates, producing a gradient along the quadrupole axis. There are a variety of methods to apply longitudinal gradients; see section 3.2 for another. Bottom: an ion trajectory (red) in a longitudinal trapping potential (black), assuming the RFQ is filled with buffer gas. To cool and bunch a continuous beam, the buffer gas pressure must be high enough that most ions cool to the thermal energy of the neutrals by the time they reach the trapping region.

For an ion traveling in an evacuated RFQ aligned with the z axis, the equations of motion are

$$\ddot{x} = -\frac{\omega a_x}{2} + x q_x \omega \cos(\omega t) \tag{2.1}$$

$$\ddot{y} = -\frac{\omega a_y}{2} + y q_y \omega \cos(\omega t) \tag{2.2}$$

$$\ddot{z} = -\frac{Q}{m}\frac{\mathrm{d}\phi(z)}{\mathrm{d}z} \tag{2.3}$$

where dots indicate time derivatives, ω is the angular frequency of the applied RF signals, Q is the ion charge, m is its mass, $\phi(z)$ is the static longitudinal electric potential, and a and q are the *Mathieu stability parameters*,

$$a_x = -a_y = \frac{4QU}{m\omega^2 r_0^2} \tag{2.4}$$

$$q_x = -q_y = \frac{2QV}{m\omega^2 r_0^2}, \tag{2.5}$$

where U is a possible constant offset voltage between the two RF phases (this should be zero for an RFQ ion cooler), V is the zero to peak RF amplitude, and r_0 is the minimum distance from a quadrupole electrode to the central axis.

Equations 2.1 and 2.2 are Mathieu equations with solutions of the form

$$j = A_1 e^{i\beta\omega t/2} \sum_{n=-\infty}^{\infty} C_{2n} e^{in\omega t} + A_2 e^{-i\beta\omega t/2} \sum_{n=-\infty}^{\infty} C_{2n} e^{-in\omega t},\ j \in \{x, y\}, \tag{2.6}$$

where A_1 and A_2 are integration constants determined by the initial conditions of the ion motion, and the constants β and C_{2n} depend only on the stability parameters a and q. If β is imaginary or a complex number then there are real exponential factors in equation 2.6 and ions are unbound in the transverse direction. If β is real and in the range $(2n, 2n+1)$ for integer $n \geq 0$, then ion motion is periodic and bound inside the quadrupole rods. If β is real and in the range $[2n-1, 2n]$ for integer $n > 0$, transverse ion motion is periodic but ions eventually escape the quadrupole. It's important to note that these outcomes are determined completely by the stability parameters, so one only needs to choose appropriate RF signals to produce stable ion motion regardless of the ion's initial state. Integer values of β form the boundaries of stable regions in a plot of a vs. q referred to as a stability diagram (see figure 2.4). The function $\beta(a, q)$ does not have a convenient closed form; there are approximation schemes [12, p 70], however the level curves in figure 2.4 were generated with the Scientific Python special functions package [35].

When an RFQ is operating within the first stability region with $a \approx 0$, the RF field may be approximated with a static *pseudopotential* which ignores small details of the ion motion but accurately describes the secular motion (assuming ions are singly charged) [13, 42]. The

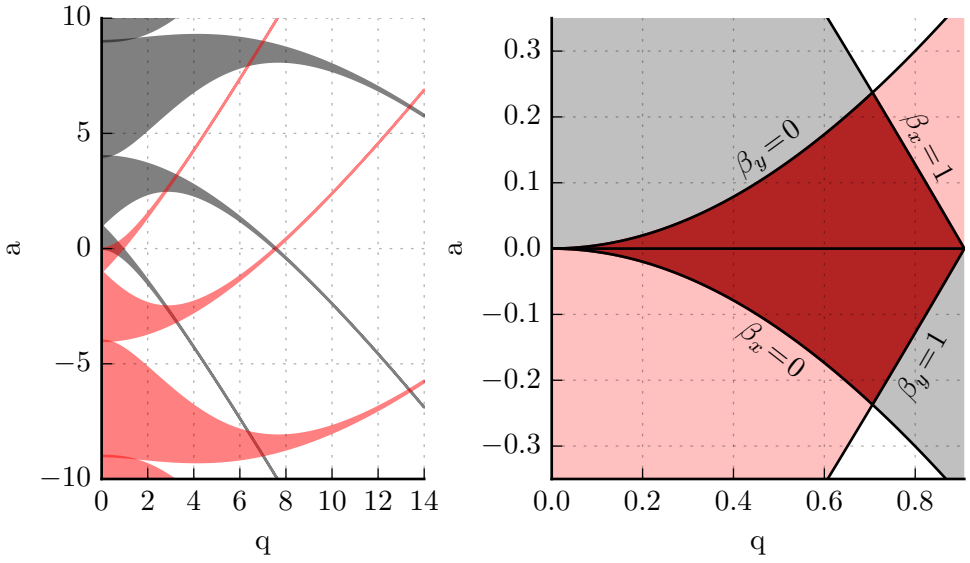

Figure 2.4: Left: diagram showing multiple regions in (a, q) space where radial ion motion is stable. Shaded regions show stability in the x coordinate (gray) and the y coordinate (red). Stability regions are bounded by level curves where β is an integer. Right: detail of the first stability region. An RFQ ion cooler operates near the $a = 0$ line where the RF signals on the quadrupole electrodes are exactly antisymmetric.

pseudopotential is a cylindrically symmetric harmonic oscillator potential,

$$\phi_p(r) = \frac{q_x V}{8}\left(\frac{r}{r_0}\right)^2 = \frac{QV^2}{4m\omega^2 r_0^2}\left(\frac{r}{r_0}\right)^2. \tag{2.7}$$

If the ion is also near the longitudinal minimum of a trap then the ion motion is an approximately harmonic 3D oscillation (see figure 2.2).

The previous paragraph describes ion motion in an *evacuated* RFQ. RFQs used to cool and bunch ions are filled with buffer gas to absorb kinetic energy from the ion beam. The microscopic details of ion motion in buffer gas are complex and require computational methods (see section 4.1). While it isn't a standard technique, one could treat ion motion in buffer gas as damped harmonic motion with a damping coefficient which decays over time,

$$\ddot{r} = -\frac{Q}{m}\frac{\mathrm{d}}{\mathrm{d}r}\phi_p(r) - \frac{e^{-t/c}}{m}\dot{r} \tag{2.8}$$

$$\ddot{z} = -\frac{Q}{m}\frac{\mathrm{d}}{\mathrm{d}z}\phi(z) - \frac{e^{-t/c}}{m}\dot{z}, \tag{2.9}$$

where the characteristic decay time c would depend primarily on the gas pressure and the mass of the neutral particles. This approximation might be helpful for initial parameter estimation when designing an RFQ or experiment, however in this work we rely on detailed

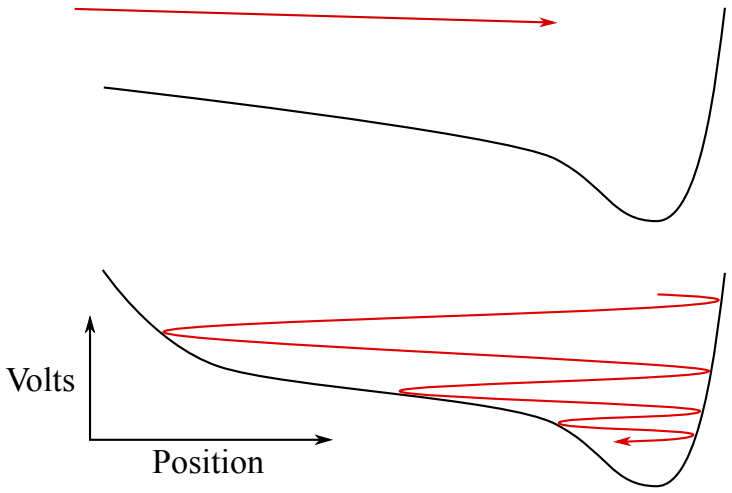

Figure 2.5: Top: ion trajectory (red) and the initial longitudinal potential (black) in the first RFQ in the TITAN MR-ToF. This is a schematic of the average trajectory for an ion bunch emitted from the cooler/buncher. Bottom: after an ion bunch enters the trapping region, the potential at the entrance aperture is raised. Switching is required because the buffer gas pressure is too low to completely cool the ions in one pass.

numerical simulations of ion motion including buffer gas collisions. The simulations are described in chapter 4.

At TITAN, the continuous beam from ISAC is cooled and bunched in an RFQ similar to the one shown in figure 2.3. The beam from the cooler/buncher can be transported to the Penning trap, the EBIT, or the MR-ToF (once it's installed on the platform). The MR-ToF contains several RFQs which transport ions to and from the mass analyzer, however they operate in a slightly different mode, shown in figure 2.5. The MR-ToF also contains a small gas filled Paul trap similar to the one shown in figure 2.1 which is positioned directly in front of the mass analyzer. The Paul trap is required to cool ions in a confined space where a strong and highly linear extraction potential may be applied to kick ions into the mass analyzer after they've been cooled.

2.2 Paraxial ion beams

One of the more elegant descriptions of a charged particle beam in optical systems like a mass spectrometer involves a set of matrix operations on phase space manifolds. In this case the canonical position-momentum phase space coordinates are replaced with functions of a new coordinate z along the *optic axis*, a hypothetical ion trajectory passing through the potential minima of all ion optics in the system which may have a convoluted path through a Cartesian coordinate system. A seventh coordinate may also be included to account for the mass of the particles. Assuming static electromagnetic potentials, the phase space position

vector of an ion is

$$\vec{r}(z) = \begin{pmatrix} x(z) & a(z) & y(z) & b(z) & t(z) & \delta_K(z) & \delta_m \end{pmatrix} \tag{2.10}$$

where x and y are coordinates orthogonal to the optic axis, $a = \mathrm{d}x/\mathrm{d}z$, $b = \mathrm{d}y/\mathrm{d}z$, and t is the time of flight. The final two coordinates are defined relative to a reference particle whose mass, kinetic energy, and charge are m_r, K_r, and Q_r. The last two phase space coordinates of an arbitrary ion are then

$$\delta_K(z) = \frac{K(z)/Q - K_r(z)/Q_r}{K_r(z)/Q_r} \qquad \xRightarrow{Q=Q_r} \qquad K(z) = (1 + \delta_K(z))K_r(z), \tag{2.11}$$

$$\delta_m = \frac{m/Q - m_r/Q_r}{m_r/Q_r} \qquad \xRightarrow{Q=Q_r} \qquad m = (1 + \delta_m)m_r, \tag{2.12}$$

where m, K, and Q are the mass, kinetic energy, and charge of the ion of interest. In this representation time is a scalar field; it's determined by the geometry of the electromagnetic potentials and it's only defined as a displacement between two points in space. Those displacements are typically between an object plane where an ion starts its transit through an optical system and a series of image planes perpendicular to the optic axis. Vectors in phase space are transformed from one plane to the next using transfer matrices. A development of mathematical methods in ion optics is available in textbooks like [61] and [63], however the topic is complex and only a few details are necessary here.

A transfer matrix $\mathcal{T}$ is a 7×7 matrix consisting of all partial derivatives of $\vec{r}(z)$ of a certain order. Ion transport through an arbitrary system may be constructed by multiplying transfer matrices between a series of intermediate image planes. If an ion beam is nearly axial (ions are close to the optic axis and their momenta make small angles with it), then we can ignore everything except the first order transfer matrices. This is called the *paraxial approximation*, and the transfer matrix $\mathcal{T}_{0i}$ representing paraxial transport between planes at z_0 and z_i is

$$\mathcal{T}_{0i} = \begin{pmatrix} \frac{\partial x(z)}{\partial x} & \frac{\partial x(z)}{\partial a} & \frac{\partial x(z)}{\partial y} & \frac{\partial x(z)}{\partial b} & \frac{\partial x(z)}{\partial t} & \frac{\partial x(z)}{\partial \delta_K} & \frac{\partial x(z)}{\partial \delta_m} \\ \frac{\partial a(z)}{\partial x} & \frac{\partial a(z)}{\partial a} & \frac{\partial a(z)}{\partial y} & \frac{\partial a(z)}{\partial b} & \frac{\partial a(z)}{\partial t} & \frac{\partial a(z)}{\partial \delta_K} & \frac{\partial a(z)}{\partial \delta_m} \\ \frac{\partial y(z)}{\partial x} & \frac{\partial y(z)}{\partial a} & \frac{\partial y(z)}{\partial y} & \frac{\partial y(z)}{\partial b} & \frac{\partial y(z)}{\partial t} & \frac{\partial y(z)}{\partial \delta_K} & \frac{\partial y(z)}{\partial \delta_m} \\ \frac{\partial b(z)}{\partial x} & \frac{\partial b(z)}{\partial a} & \frac{\partial b(z)}{\partial y} & \frac{\partial b(z)}{\partial b} & \frac{\partial b(z)}{\partial t} & \frac{\partial b(z)}{\partial \delta_K} & \frac{\partial b(z)}{\partial \delta_m} \\ \frac{\partial t(z)}{\partial x} & \frac{\partial t(z)}{\partial a} & \frac{\partial t(z)}{\partial y} & \frac{\partial t(z)}{\partial b} & \frac{\partial t(z)}{\partial t} & \frac{\partial t(z)}{\partial \delta_K} & \frac{\partial t(z)}{\partial \delta_m} \\ \frac{\partial \delta_K(z)}{\partial x} & \frac{\partial \delta_K(z)}{\partial a} & \frac{\partial \delta_K(z)}{\partial y} & \frac{\partial \delta_K(z)}{\partial b} & \frac{\partial \delta_K(z)}{\partial t} & \frac{\partial \delta_K(z)}{\partial \delta_K} & \frac{\partial \delta_K(z)}{\partial \delta_m} \\ 0 & 0 & 0 & 0 & 0 & 0 & 1 \end{pmatrix}_{z = z_1} \tag{2.13}$$

Many transfer matrix elements disappear under certain symmetry conditions [63, p 36]. The conditions which apply to the TITAN MR-ToF are that ions only see electrostatic fields and the system has two planes of symmetry (these are the symmetries of a static quadrupole

field). In this case the first order transfer matrix reduces to

$$\mathcal{T}_{0i} = \begin{pmatrix} \frac{\partial x(z)}{\partial x} & \frac{\partial x(z)}{\partial a} & 0 & 0 & 0 & 0 & 0 \\ \frac{\partial a(z)}{\partial x} & \frac{\partial a(z)}{\partial a} & 0 & 0 & 0 & 0 & 0 \\ 0 & 0 & \frac{\partial y(z)}{\partial y} & \frac{\partial y(z)}{\partial b} & 0 & 0 & 0 \\ 0 & 0 & \frac{\partial b(z)}{\partial y} & \frac{\partial b(z)}{\partial b} & 0 & 0 & 0 \\ 0 & 0 & 0 & 0 & 1 & \frac{\partial t(z)}{\partial \delta_K} & \frac{\partial t(z)}{\partial \delta_m} \\ 0 & 0 & 0 & 0 & 0 & \frac{\partial \delta_K(z)}{\partial \delta_K} & 0 \\ 0 & 0 & 0 & 0 & 0 & 0 & 1 \end{pmatrix}_{z = z_i} \tag{2.14}$$

The elements in $\mathcal{T}_{0i}$ which involve the spatial coordinates (x, a, y, b) are important for keeping ions near the optic axis. Ions are confined spatially using a set of focusing elements similar to common light optics like those found in a camera. These optics are described in detail elsewhere, see especially [63, section 3.2] for electrostatic lenses and [63, section 3.5] for focusing with electrostatic mirrors. Unlike light optics, ion optics may also produce *time foci*, planes at which ions of the same mass will arrive at the same time. If ions reach a time focus after passing through an ion optical system then that system is said to be *isochronous*. Isochronicity means that ions of the same mass reach the focal plane at the same time regardless of their initial conditions.

Isochronicity is the primary requirement for optics in a ToF spectrometer because ions separated in time are supposed to represent different masses. The temporal properties of an ion beam are represented in the first order transfer matrix by $\partial t/\partial \delta_K$ and $\partial t/\partial \delta_m$. A time of flight mass spectrometer requires that ions separate in time, so $\partial t/\partial \delta_m$ must be nonzero. A perfect time focus requires that ions of equal mass are isochronous regardless of their initial kinetic energy, however the $\partial t/\partial \delta_K$ element in $\mathcal{T}_{0i}$ means that an ion optical system can only be isochronous under certain conditions. Optical aberrations due to δ_K must be corrected for at all orders but only first and second order time focusing will be discussed in any detail here. Higher order and spatial properties of the TITAN MR-ToF are discussed in references [55, 64].

2.3 First order time focusing

The simplest time of flight measurement on trapped ions involves kicking ions out of the trap with a constant electric field $\mathcal{E}$ and letting them fly through a field free drift space (see figure 2.6). Let z_1 represent the distance from the initial position of a reference ion to the end of the extraction field. The flight path for an arbitrary ion is then split in two: $z_1 - z_0$ is the distance from the initial ion position to the end of the extraction field (time of flight t_{01}), and $z - z_1$ is the distance traveled with no field (time of flight t_d). Given that the force on a charged particle is $ma = m(z_1 - z_0)/t^2 = Q\mathcal{E}$, the time required for an ion starting

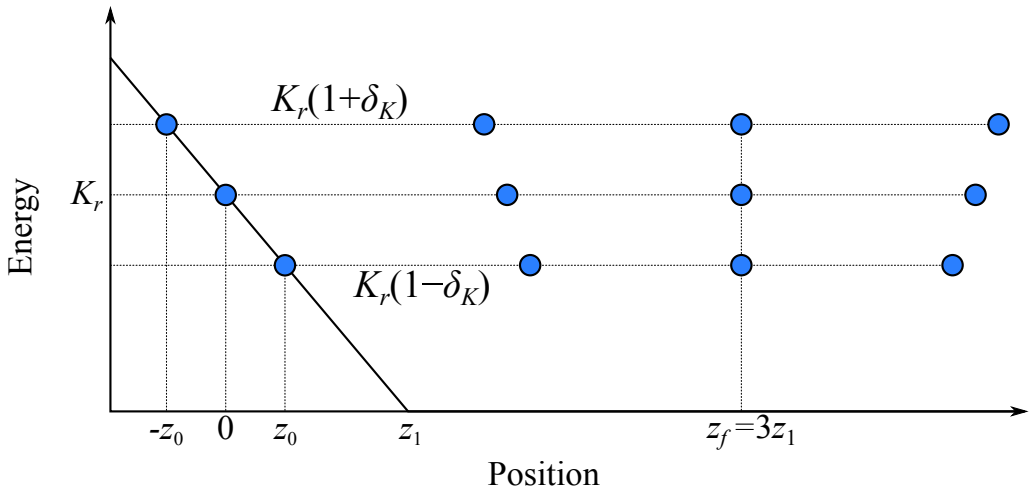

Figure 2.6: A simple time of flight system with a single accelerating potential (black line). Three ions with the same mass to charge ratio start from rest at the left and fly through a time focus when faster ions overtake slower ones. The time of flight for an ion in this system is given in equations 2.16 and 2.17

from rest to traverse the extraction field is

$$t_{01} = \sqrt{\frac{2m(z_1 - z_0)}{Q\mathcal{E}}} = \frac{\sqrt{2mK}}{Q\mathcal{E}} = \frac{\sqrt{2m(1+\delta_m)K_r}}{Q\mathcal{E}} = z_1\sqrt{\frac{2m(1+\delta_m)}{K_r}}, \tag{2.15}$$

where $K = Q\mathcal{E}(z_1 - z_0)$ is the kinetic energy of an arbitrary ion in the drift region, $K_r = Q\mathcal{E}z_1$ is the reference kinetic energy in the drift region, and I've assumed that all ions have the same charge state so that the second part of equation 2.11 applies. From the definition of non-relativistic kinetic energy, $K = mv^2/2$, we can write down the full time of flight for this simple setup:

$$\begin{aligned} t(z) = t_{01} + t_d &= z_1\sqrt{\frac{2m(1+\delta_m)}{K_r}} + (z - z_1)\sqrt{\frac{m}{2(1+\delta_m)K_r}} \\ &= \sqrt{\frac{2m}{K_r}}\left(z_1\sqrt{1+\delta_m} + \frac{z - z_1}{2}\frac{1}{\sqrt{1+\delta_m}}\right). \end{aligned} \tag{2.16}$$

The time focusing conditions are determined from the Taylor series expansions for $\sqrt{1+\delta_m}$ and $1/\sqrt{1+\delta_m}$,

$$\begin{aligned} t(z) &\to \sqrt{\frac{2m}{K_r}}\left(z_1\left(1 + \frac{\delta_K}{2} - \frac{\delta_K^2}{8}\right) + \frac{z - z_1}{2}\left(1 - \frac{\delta_K}{2} + \frac{\delta_K^2}{8}\right)\right) \\ &\to \sqrt{\frac{2m}{K_r}}\left(\frac{z + z_1}{2} + \frac{\delta_K(3z_1 - z)}{4} + \frac{\delta_K^2(3z - 5z_1)}{16}\right). \end{aligned} \tag{2.17}$$

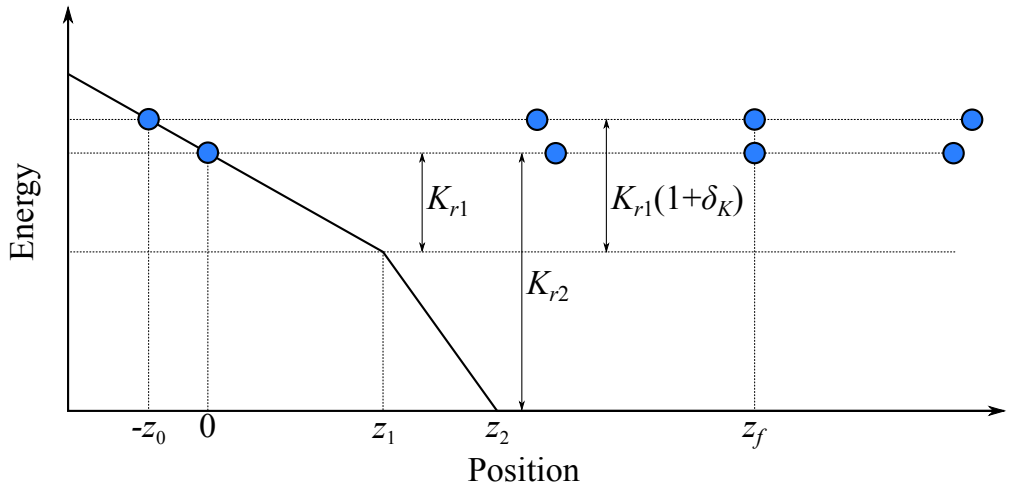

Figure 2.7: A time of flight system with two acceleration stages. As in figure 2.6, ions in this figure have the same mass to charge ratio and they start from rest.

The position of the first order time focus, z_f, is the location where the term to first order in δ_K goes to zero; $z_f = 3z_1$. Going back to equation 2.14, this eliminates the $\partial t(z)/\partial\delta_K$ term in the first order transfer matrix $\mathcal{T}_{0f}$ between the object and focal planes. For an ion starting from rest, the time of flight to the time-energy focal plane (ignoring the δ_K^2 term) is then

$$t(z_f) = 2z_1\sqrt{\frac{2m}{K_r}}. \tag{2.18}$$

From the δ_K^2 term in equation 2.17 we see that the condition for second order time focusing is $z = 5z_1/3$. The first and second order time-energy focusing conditions are incompatible; one can make a first order isochronous measurement by placing an ion detector at z_f, but there will be an irreducible second order aberration (identical ions will arrive at the focal plane with a minimum time spread proportional to δ_K^2). The only way to eliminate aberrations in the focal plane is to introduce additional ion optics into the system, creating additional degrees of freedom with which to control ion motion.

2.4 Second order time focusing

The simple time of flight system discussed in the last section had a single optical element which accelerated ions into a drift region, and we found an image plane in that system which was isochronous to first order. Eliminating the second order aberration at the focal plane requires a simultaneous solution to the first and second order focusing conditions, which is impossible in the simple system because the only available degree of freedom is z_1. One way to introduce another degree of freedom is to insert a second acceleration stage so that ions fly through two different electric fields before entering the drift space (see figure 2.7). The

technique is described by Wiley and Mclaren in a paper published in 1955 which includes the position of the first order time focus [59].

In the two stage system, the flight path is split into three sections: $z_1 - z_0$ is the length of the first acceleration stage (field $\mathcal{E}_1$, time of flight t_{01}), $z_2 - z_1$ is the length of the second acceleration stage (field $\mathcal{E}_2$, time of flight t_{12}), and $z - z_2$ is the distance traveled through the drift region (zero field, time of flight t_d). Ions in the accelerating fields feel a constant force, and a reference ion starting from rest at $z = 0$ will acquire kinetic energies

$$K_{r1} = Q\mathcal{E}_1 z_1, \tag{2.19}$$

$$K_{r2} = K_{r1} + Q\mathcal{E}_2(z_2 - z_1), \tag{2.20}$$

where K_{r1} is the reference kinetic energy at the end of the first accelerating field and K_{r2} is the reference kinetic energy in the drift region. An arbitrary ion starting from rest at a distance z_0 away from the reference ion will acquire a slightly different kinetic energy in the first acceleration stage because it starts at a different potential energy, but all ions traverse the whole second stage and acquire additional kinetic energy equal to $K_{r2} - K_{r1}$. The kinetic energies of any ion passing the points z_1 and z_2 are therefore

$$K_1 = K_{r1}(1 + \delta_K), \tag{2.21}$$

$$K_2 = K_1 + (K_{r2} - K_{r1}) = K_{r2} + K_{r1}\delta_K, \tag{2.22}$$

where δ_K is the relative deviation in kinetic energy acquired in the first accelerating field. The times of flight through the accelerating fields are found from the ratio of the change in ion momentum to the force on the particle in each region

$$t_{01} = \frac{\sqrt{2mK_1}}{Q\mathcal{E}_1} = z_1\sqrt{\frac{2m(1+\delta_K)}{K_{r1}}}, \tag{2.23}$$

$$t_{12} = \frac{\sqrt{2m}(\sqrt{K_2} - \sqrt{K_1})}{Q\mathcal{E}_2} = \sqrt{2m}(z_2 - z_1)\frac{\sqrt{K_{r2} + \delta_K K_{r1}} - \sqrt{K_{r1}(1+\delta_K)}}{K_{r2} - K_{r1}}. \tag{2.24}$$

The time of flight in the drift region is found directly from the total ion kinetic energy,

$$t_d = (z - z_2)\sqrt{\frac{m}{2K_2}} = \frac{z - z_2}{2}\sqrt{\frac{2m}{K_{r2} + \delta_K K_{r1}}}. \tag{2.25}$$

The total time of flight is then the sum of the partial times,

$$t(z) = \sqrt{2m}\Bigg(\frac{(z - z_2)}{2\sqrt{K_{r2} + \delta_K K_{r1}}} + (z_2 - z_1)\frac{\sqrt{K_{r2} + \delta_K K_{r1}}}{K_{r2} - K_{r1}} + \sqrt{1 + \delta_K}\left(\frac{z_1}{\sqrt{K_{r1}}} - \frac{\sqrt{K_{r1}}(z_2 - z_1)}{K_{r2} - K_{r1}}\right)\Bigg). \tag{2.26}$$

As in equation 2.17, the time-energy focusing conditions are determined from Taylor series expansions in δ_K about $\delta_K = 0$. The series required to expand equation 2.26 are

$$\sqrt{1+\delta_K} \to 1 + \frac{\delta_K}{2} - \frac{\delta_K^2}{8}, \tag{2.27}$$

$$\sqrt{K_{r2}+\delta_K K_{r1}} \to \sqrt{K_{r2}}\left(1 + \frac{\delta_K K_{r1}}{2K_{r2}} - \frac{(\delta_K K_{r1})^2}{8K_{r2}^2}\right) = \frac{1}{\sqrt{K_{r2}}}\left(1 + \frac{\delta_K}{2\lambda} - \frac{\delta_K^2}{8\lambda^2}\right), \tag{2.28}$$

$$\frac{1}{\sqrt{K_{r2}+\delta_K K_{r1}}} \to \frac{1}{\sqrt{K_{r2}}}\left(1 - \frac{\delta_K K_{r1}}{2K_{r2}} + \frac{3(\delta_K K_{r1})^2}{8K_{r2}^2}\right) = \frac{1}{\sqrt{K_{r2}}}\left(1 - \frac{\delta_K}{2\lambda} + \frac{3\delta_K^2}{8\lambda^2}\right), \tag{2.29}$$

where I've made the substitution

$$\lambda = K_{r2}/K_{r1}. \tag{2.30}$$

Inserting the series into equation 2.26 gives

$$t(z) = \sqrt{2m}\Bigg(\frac{(z-z_2)}{2\sqrt{K_{r2}}}\left(1 - \frac{\delta_K}{2\lambda} + \frac{3\delta_K^2}{8\lambda^2}\right) + \frac{(z_2-z_1)\sqrt{K_{r2}}}{K_{r1}(\lambda-1)}\left(1 + \frac{\delta_K}{2\lambda} - \frac{\delta_K^2}{8\lambda^2}\right) + \frac{1}{\sqrt{K_{r1}}}\left(1 + \frac{\delta_K}{2} - \frac{\delta_K^2}{8}\right)\left(z_1 - \frac{z_2-z_1}{\lambda-1}\right)\Bigg) \tag{2.31}$$

The $\partial t(z)/\partial\delta_K$ element in the first order transfer matrix (equation 2.14) comes from the first order terms in δ_K,

$$\frac{\partial t(z)}{\partial \delta_K} \approx \frac{\delta_K}{2\lambda}\sqrt{\frac{m}{2K_{r2}}}\left(2\lambda^{3/2} z_1\left(1 - \frac{z_2-z_1}{z_1(\lambda+\sqrt{\lambda})}\right) - (z-z_2)\right). \tag{2.32}$$

The primary time focus (the position of the time-energy focal plane) occurs when $\partial t(z)/\partial\delta_K$ goes to zero. From equation 2.32, the distance from the end of the accelerating fields to the time-energy focal plane is

$$z - z_2 = 2\lambda^{3/2} z_1\left(1 - \left(\frac{z_2-z_1}{z_1}\right)\frac{1}{\lambda+\sqrt{\lambda}}\right). \tag{2.33}$$

The δ_K^2 terms in equation 2.31 produce a second order transfer matrix element,

$$\frac{\partial^2 t(z)}{\partial \delta_K^2} \approx \frac{3\delta_K^2}{16\lambda^2}\sqrt{\frac{2m}{K_{r2}}}\left((z-z_2) - \frac{2\lambda^{5/2} z_1}{3}\left(1 - \frac{(z_2-z_1)(\lambda^{3/2}-1)}{z_1\lambda^{3/2}(\lambda-1)}\right)\right). \tag{2.34}$$

From equation 2.34, we can read off the second order time-energy focusing condition,

$$z - z_2 = \frac{2\lambda^{5/2} z_1}{3}\left(1 - \left(\frac{z_2-z_1}{z_1}\right)\frac{\lambda^{3/2}-1}{\lambda^{3/2}(\lambda-1)}\right). \tag{2.35}$$

The second order aberration due to δ_K is eliminated in the time focal plane by choosing parameters such that equations 2.33 and 2.35 are solved simultaneously. The relevant pa-

rameters are λ and the lengths of the fields. λ is the ratio of the total voltage drop seen by the reference ion to the potential difference it sees in the first acceleration region. For a given set of ion optics, the position of the primary time focus may be shifted by changing the applied voltages but the second order aberration will only disappear when voltages are chosen such that they fulfill both focusing conditions at the same time. The distance between a first order time-energy focal plane and a second order focal plane depends on the geometry of the system but in general one shouldn't expect the correction to be small.

The method above demonstrates a general approach to the design of ion optics; one chooses the geometric symmetries of the system and then introduces as many degrees of freedom as are required to eliminate optical aberrations up to a certain order. This is a fundamentally algebraic problem [29, 30, 47, 65] but it eventually becomes analytically unmanageable when real fields are taken into account. The sharp dilineations between accelerating regions described here may be approximated with wire grids across the flight path of the ions, but in that case some ions will always hit the grids. It's possible to construct a 99% grid, one in which only 1% of ions hit the wires, however in a multiple reflection system ions might see a grid tens or hundreds of times and the compounded losses would be unacceptable in a spectrometer meant to handle exotic nuclei. Gridless systems are required for rare isotope beams, and with gridless electrodes there is always a nonlinear fringing field that extends beyond the region where a potential gradient is applied. Analytic descriptions are very useful in designing gridless systems, however for higher order corrections it can be more practical to fly virtual ions through numerical simulations which vary dimensions and voltages of the optics algorithmically.

2.5 Isochronous reflections and MR-ToF spectrometers

Wiley and Mclaren described the two-stage optical system discussed in the previous section as a method to produce a high quality ion source for time of flight spectrometry [59]; a sample would be ionized in the first accelerating region and the voltages could be tuned to place the time-energy focal plane at the position of an ion detector. The same technique may be used to transport ions between multiple time-energy foci. Instead of sending ions directly to a detector, one could use a second multi-stage potential to reflect ions back into the drift region. A time focus is achieved after each reflection because high-energy ions penetrate farther into the reflecting potential and take longer to turn around compared to low-energy ions. As shown in the previous two sections, isochronous focusing conditions exist for any linear electrostatic field which obeys certain symmetries, so the reflector will have its own time-energy focal plane independent of the initial accelerator. In principle one could therefore produce an isochronous ion optical system with an arbitrarily long flight path – an ideal time of flight spectrometer.

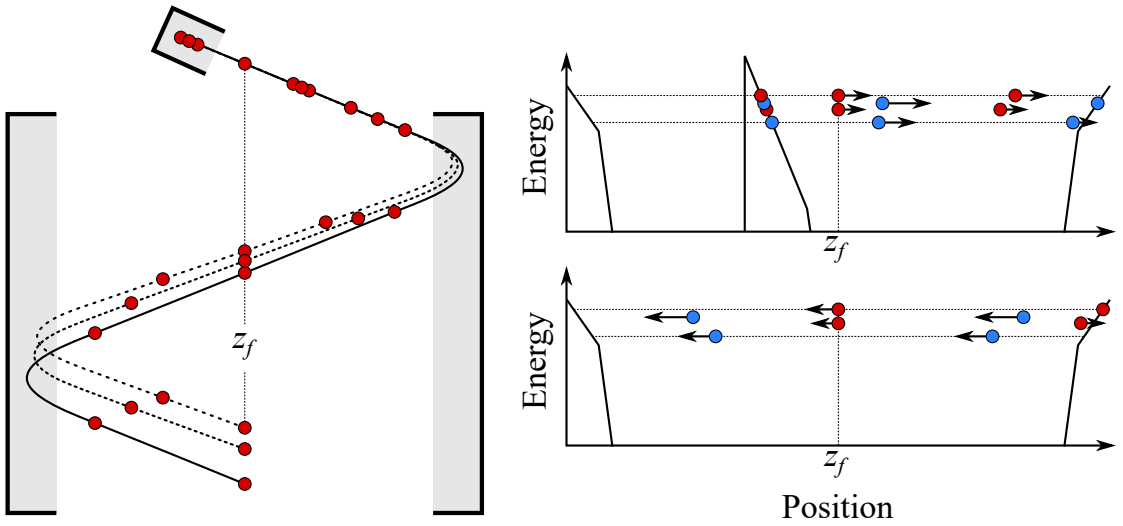

Figure 2.8: A multiple reflection time of flight system with an open ion flight path. Red dots indicate ions with a larger mass to charge ratio compared to blue ions. Left: ions begin at rest in an initial accelerating field at the top of the figure and are confined between identical reflecting fields (shaded regions). Faster ions (solid line) spend more time in the mirror fields because they penetrate farther than slower ions (dashed lines), so all ions pass through the focal plane at the same time. Right: the initial accelerating potentials are chosen to produce a time-energy focus in the focal plane of the reflectors. The time and distance separating ions of different mass to charge ratio increases every time they traverse the drift region. Horizontal dashed lines indicate the energy spread of ions and vertical lines mark the time-energy focal plane.

Figure 2.8 shows a possible configuration for a multiple reflection time of flight mass spectrometer. Ions in the figure never return to the same point, so the system is called an open path spectrometer [44]. The ion path length and therefore the time of flight is determined by the distance between the reflectors and the angle of the ion source with respect to the focal plane. The mirrors and the ion source are positioned so that their time-energy foci are all in the same plane; the time-energy focus is maintained across many reflections in the figure because the geometry is set up to fulfill all focusing conditions for each optical element independently, but this need not be the case. In fact, requiring all time-energy foci to occur in the same plane is a strong geometric constraint, one that's often impossible to achieve in real applications. If this constraint is relaxed so that the focal planes of discrete optical elements don't overlap then one must work out isochronous focusing conditions for the overall system. One could use the same method shown in the previous two sections, but the time of flight (equation 2.26) would include terms for each electric potential and drift space between the ion source and the focal plane. The detailed focusing conditions would need to be calculated on a case by case basis, but it is a general rule that in order to create a time-energy focal plane at a new position along a given axis one must apply a new isochronous mirror potential along that axis[1] (see figure 2.9). This operation may be referred to as a *time focus shift* (TFS) [16].

In contrast to open path systems, closed path spectrometers may allow for an adjustable time of flight. If ions travel a closed loop inside the spectrometer then one can apply switched electric fields to admit ions into the loop and then let them out after any number of circuits through the system. The TITAN MR-ToF is a closed path spectrometer consisting of an ion trap, a pair of cylindrical reflectors, and a detector arranged along a single axis (see figure 2.10). To begin mass analysis in the TITAN MR-ToF, ions are kicked out of the trap with a two stage ejection potential and pass through a time-energy focus very close to the trap. The upstream mirror is initially near the drift potential, and the downstream mirror is set to reflect ions such that they pass through a time-energy focus in the center of the drift region. The upstream mirror is then switched into a TFS mode which moves the time focus into the downstream mirror, completing a round trip or a *turn* containing two TFS operations. After the TFS turn the mirrors are in a *multi-turn* mode which maintains symmetrical time-energy foci inside the mirrors for a predetermined number of turns. After multiple reflection analysis, ions are extracted by lowering a mirror potential and allowing them to pass out of the analyzer. In the TITAN system one can fly ions onto a detector to produce a destructive mass spectrum or fly them back into the trap where a portion of the mass spectrum may be collected in a non-destructive retrapping operation. Note that an additional time focus shift is not required for extraction because the multi-turn mirrors

[1] Assuming that time foci always occur in drift spaces. The situation may change for time foci inside optical fields; see figure 2.11.

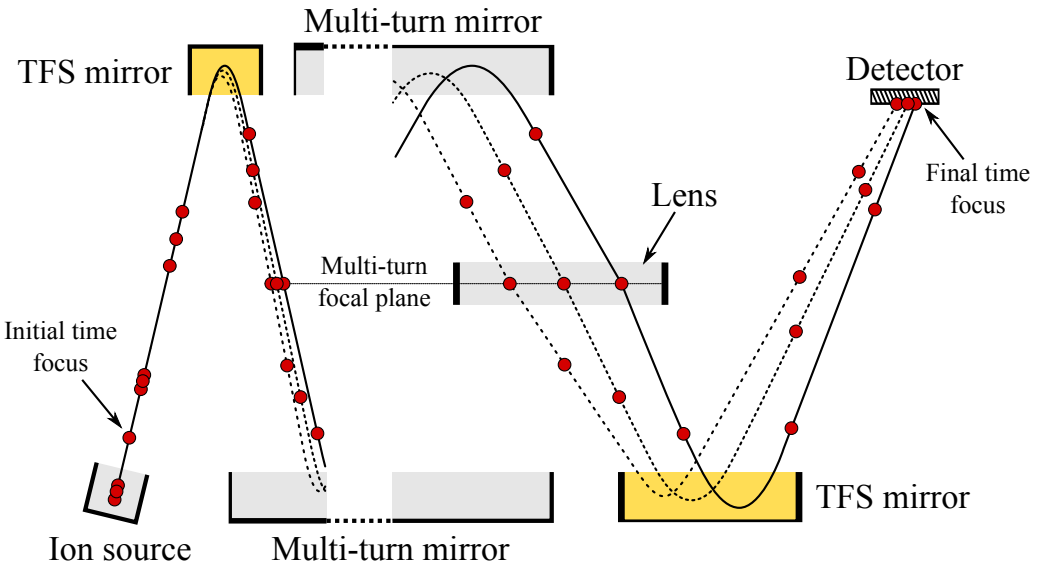

Figure 2.9: An open path MR-ToF spectrometer with additional ion optics to adjust time-energy foci after the ion source and before detection. All ions in the figure (red dots) have the same mass to charge ratio and start from rest in the ion source. Yellow mirror fields introduce a time focus shift (TFS) in the vertical direction while gray mirror fields maintain a time-energy focus on the central axis between the mirrors as in figure 2.8. A lens near the end of the flight path provides spatial focusing so that all ions hit the detector.

have virtual foci at the detector and the trap during the multiple reflection period (see figure 2.11). The mirror fields could be tuned such that the first reflection moves the time focus to the center of the drift region and the last reflection shifts the time focus either to the detector or to the trap, but that tuning has not yet been explored on the TITAN MR-ToF.

Closed path spectrometers introduce the additional complication that ions may not arrive at the detector in the correct order. If there is a large mass difference between ions in the system or if the ions have separated over a long time of flight, then light ions might overtake heavy ones before a mirror is opened. If that happens then ion bunches will arrive at the detector out of order. It is possible to identify masses in the sample by taking several ToF spectra at many different turn numbers; fast ions will eventually disappear from the beginning of a spectrum and reappear at the other end of a spectrum at some larger number of turns[2], however the analysis in this case is more complicated and requires a larger sample of ions. Therefore it's useful to estimate the *mass range* of a closed path mass analyzer as a function of the turn number. The mass range represents the relative mass difference between the lightest and heaviest ions which will be properly ordered after some number of turns.

[2]Fast ions should appear at the start of a ToF spectrum but they'll look like slow ions (at the end of a ToF spectrum) if they're starting their nth $+ 1$ turn as slow ions finish their nth turn

Three times are required for the calculation: t_i is the flight time from the ion source to the first mirror field an ion sees, t_m is the time spent in a mirror before returning to the drift space, and t_T is the time of flight for a single turn. These times are illustrated in figure 2.12. Noting that flight times are proportional to the square root of the ion mass and defining them in terms of t_T:

$$t_T = T\sqrt{m}, \tag{2.36}$$

$$t_i = c_i T\sqrt{m}, \tag{2.37}$$

$$t_m = c_m T\sqrt{m}, \tag{2.38}$$

where m is the ion mass, T is a scaling constant for a single turn, c_i is the fraction of the single turn time required for injection, and c_m is the fraction of a single turn spent in one mirror. Ions must be outside the mirror fields while the fields are switching in order to maintain good focusing, so the time of flight of the slowest ion in a turn (the third line in figure 2.12) is then

$$t_i + (n-1)t_T + t_m = (c_i + c_m + n - 1)T\sqrt{M}, \tag{2.39}$$

where $M > m$. The time of flight for the fastest ion in a turn (the fourth line in figure 2.12) is

$$t_i + nt_T = (c_i + n)T\sqrt{m}. \tag{2.40}$$

Setting equations 2.39 and 2.40 equal and rearranging, we see that the maximum ratio in mass between unambiguously detected ions at turn n is

$$\frac{M}{m} = \left(1 + \frac{1 - c_m}{c_i + c_m + n - 1}\right)^2. \tag{2.41}$$

We can estimate the mass range in the TITAN MR-ToF using simulated position data for ^{133}Cs shown in figure 2.13. From the figure it appears that the time of flight for a single turn, t_T, is about 22 µs (neglecting the ToF difference between the TFS turn and multi-turns). The injection time, t_i, is roughly 10.5 µs, and the time of flight in a mirror, t_m is around 7 µs. The constants in equations 2.37 and 2.38 are then $c_i = 0.48$ and $c_m = 0.32$. At 2 turns (1 TFS turn plus 1 multi-turn), the mass range is about 1.8. At 100 turns the mass range is 1.005, which corresponds to roughly 1 amu near mass 133 because $134/133 = 1.008$.

2.6 Turnaround time

The entire discussion up to this point has assumed that ions begin from rest in a source or trap. If ions begin from rest then an aberration-free optical system would produce ideal time-energy foci – all ions of the same mass to charge ratio would arrive in a focal plane at exactly

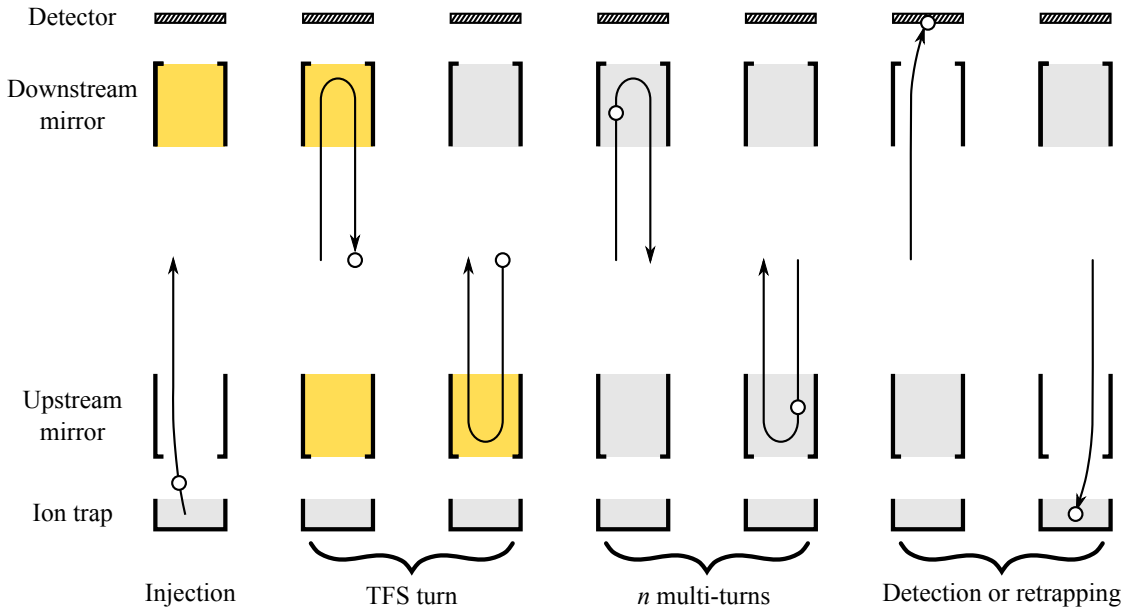

Figure 2.10: Diagram of the TITAN MR-ToF spectrometer showing the different time foci (open circles) during operation. Ions begin in a gas filled quadrupole trap, they're injected into the analyzer, and the mirrors are closed around them. Yellow mirror fields represent TFS reflections. Gray fields represent multi-turn reflections which maintain time foci inside the mirrors over any number of turns. Ions are extracted from the mass analyzer by lowering one of the mirror fields.

the same time. But the assumption of ions at rest is not valid; in reality any collection of atoms has some energy distribution. Since a "perfect" time-energy focus exactly reproduces the original kinetic energy distribution of a sample, ions in a real spectrometer never arrive at a focal plane at exactly the same time[3]. The closest one can get to initializing ions with a single value in kinetic energy is to prepare a thermal ion population, in which case the ions will have a Maxwell-Boltzmann velocity distribution. In most MR-ToF spectrometers this is achieved via buffer gas cooling as described in section 2.1; the minimum velocity spread is then roughly determined by the temperature of the gas in the trap, however a few other factors such as RF power from trapping fields may be important.

With an initially thermal velocity distribution, half the ions will start out travelling towards the drift space and half the ions will start out traveling toward the ion source at the time the sample is kicked into the mass analyzer. Ions traveling away from the drift space must stop in an accelerating field and turn around before entering the spectrometer; they'll initially be delayed by the *turnaround time* relative to a theoretical reference ion starting at rest (see figure 2.14). The turnaround time is the time required for an ion initially flying

[3]More specifically, ions arrive at a time-energy focus with the same kinetic energy distribution they started with, but the central value of that distribution will be shifted by the difference in potential energy between the initial position and the position of the focal plane.

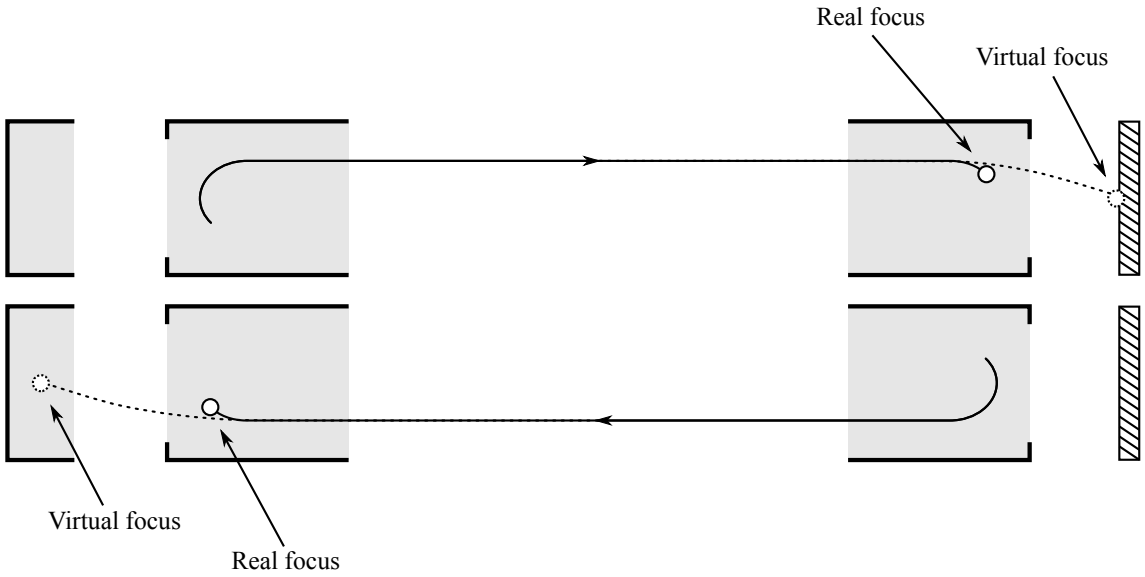

Figure 2.11: Time-energy foci of multi-turn mirror potentials in the TITAN MR-ToF mass analyzer. During multi-turn analysis, each mirror has a real time-energy focus inside the opposite mirror and also a virtual focus farther away, either in the trap or on the detector. Ions pass through the real foci while the mirrors are closed and they only reach one of the virtual foci after a mirror is opened. The time of flight to a focus marked "real" in this figure is the same as the time of flight to its corresponding virtual focus; the real foci only exist because ions slow down in the mirror potentials. Opening a mirror isn't referred to as a time focus shift because a TFS operation changes the position of a focal plane at drift potential.

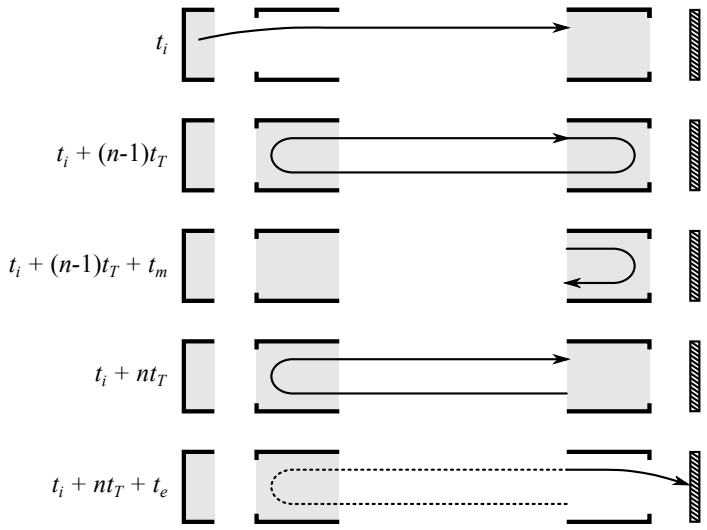

Figure 2.12: Times of flight at various points in the path of an ion flying through a closed path MR-ToF. The values on the left indicate the total time of flight for an ion reaching the end of the trajectory shown in the diagram to the right. Ions will only reach the detector in the correct order if they lie on the dashed line while the downstream mirror is switching off. The mirror colors are dropped because the difference in flight time through the different mirror potentials is small.

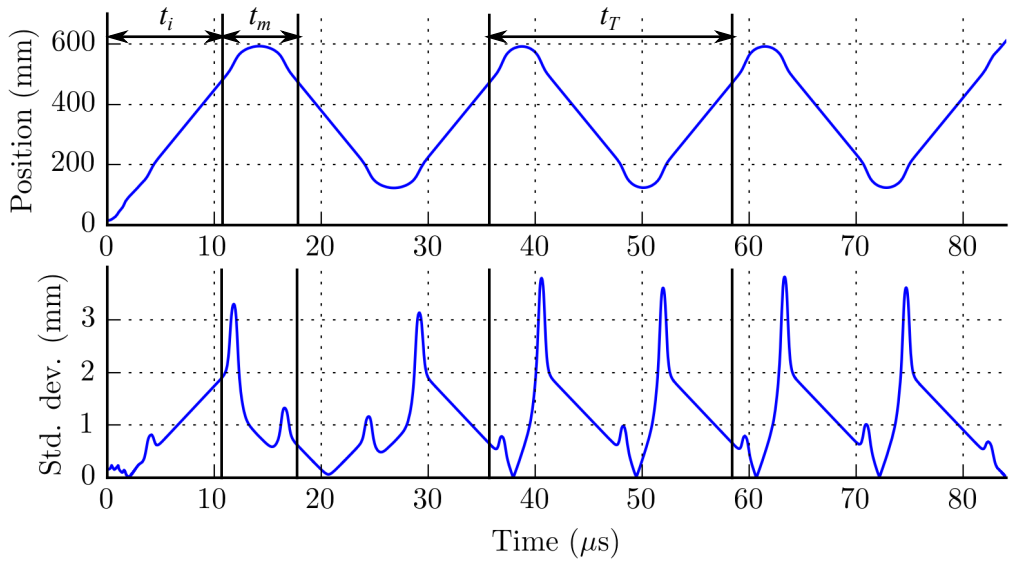

Figure 2.13: Simulated position data for 3 singly charged ^{133}Cs ions making 1 TFS turn and 2 multi-turns in the TITAN MR-ToF mass analyzer. The upper plot is the position along the axis of the analyzer, and the lower plot is the standard deviation in position on the same axis. Since ions begin at rest, time foci correspond to points where the standard deviation goes to zero, and additional structure in the standard deviation plot comes from spatial focusing optics near each mirror.

into the kicking field to stop, turn around, and return to its initial position. The overall time of flight for the higher energy ions is also a little shorter then the ToF for the reference ion; in a multiple reflection system this means that the ion cloud will get wider in time with every pass through the drift space because low-energy ions will lag behind high-energy ions.

An initial kinetic energy distribution of ions in a ToF spectrometer also complicates the choice of accelerating fields. With a shallow initial accelerating potential, the potential energy spread due to the position of the ions will be small but the turnaround time for ions with initial kinetic energy will be long (see figure 2.15). A steep initial potential will result in a short turnaround time but a large energy spread due to the size of the ion cloud. The energy spread due to the finite size of the ion cloud may be compensated for using the ion optical techniques described above, so it's best to choose an initial potential that's as steep as possible. A large inital accelerating field will also create a short time-energy focal length (equation 2.33), which is why there's a time-energy focus very close to the ion trap in the TITAN MR-ToF (see figures 2.10 and 2.13). The major drawback to a large initial energy spread is that all other ion optics in the system must accept ions throughout that energy range. In practice the initial accelerating field is limited by the parameters of other optics in the system such as lenses, which have a limited energy range over which they can focus an ion cloud.

The turnaround time represents a lower limit on the time width of an ion cloud passing through a time-energy focus. As shown in sections 2.3 and 2.4, the correlation between arrival time and initial potential energy can be completely eliminated at a focal plane using appropriate ion optics, but any initial kinetic energy will result in an irriducible time distribution at a focal plane and the width of the distribution increases with total time of flight. For a point of reference, we can estimate the turnaround time in the TITAN MR-ToF for ^{133}Cs. The most probable kinetic energy for a particle moving in one dimension at room temperature is 0.025 eV[4]. The field which kicks ions out of the trap is roughly 100 V/mm, so at 300 K, Cs^+ ion initially flying into the field will move $2.5{\cdot}10^{-4}$ mm before losing all its kinetic energy. Using this value for z_1 in equation 2.15 (with $\delta_m = 0$) and multiplying by 2 to get the time required to return to the initial position, we find that the turnaround time is approximately 5 nanoseconds. That means the minimum width of a ^{133}Cs peak in a ToF spectrum in the TITAN system is probably a little more than 5 ns, and in fact the typical ^{133}Cs peak width after 1 TFS turn and 1 multi-turn in the real spectrometer is around 8 ns.

[4]This is the kinetic energy which corresponds to the most probable velocity from a Maxwell-Boltzmann distribution.

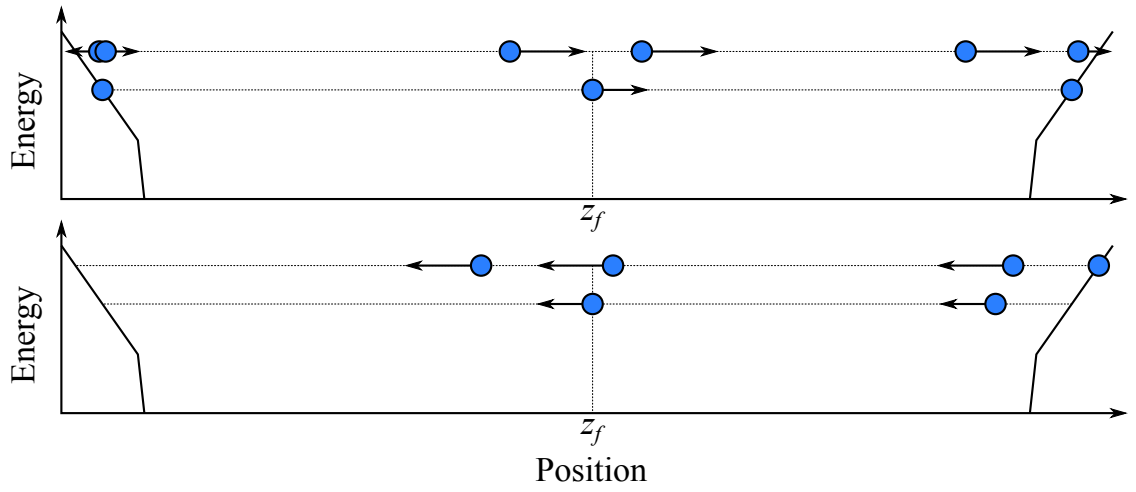

Figure 2.14: Ions starting out with a velocity spread and accelerating into a drift space with symmetrical mirror fields on either side. All ions in the figure have the same mass to charge ratio. Top: three ions start at the same position. A reference ion starts at rest and two others start with the same kinetic energy but opposite velocities. If the ions started at rest they would all reach the time-energy focal plane at the same time, but in this case the ion initially traveling towards the drift space is leading the reference ion while the ion starting in the opposite direction is delayed by the turnaround time. Bottom: after reflecting on the right, ions pass through the time-energy focus again. Because of the initial velocity distribution, the time spread at the focal plane will grow with each additional pass.

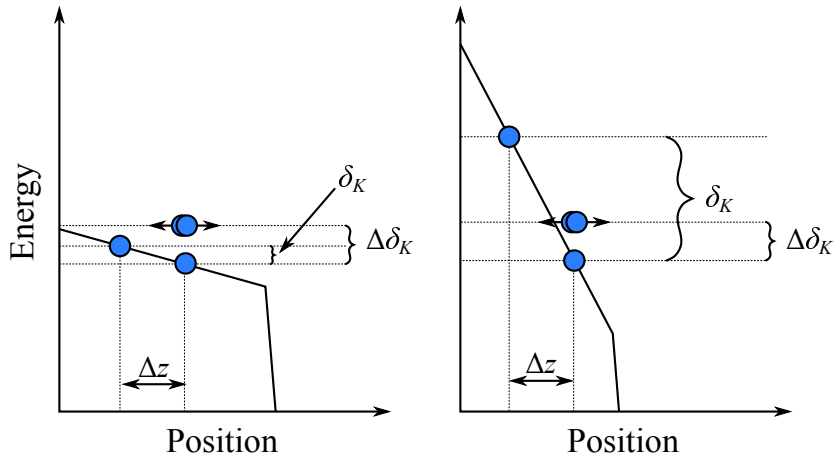

Figure 2.15: Comparison of accelerating potentials which kick an ion cloud into a ToF spectrometer. A shallow initial potential results in a small potential energy difference due to Δz but the turnaround time may be very long. A steep initial potential will result in a smaller turnaround time but a larger energy spread due to Δz. The kinetic energy distribution creates an uncertainty $\Delta\delta_K$ in the energy difference between an arbitrary ion and the reference ion.

2.7 Mass resolving power

The mass resolving power is defined as $R = m/\Delta m$, where m is the mass of an ion of interest and Δm is the uncertainty in the mass. The resolving power is the minimum relative difference between two masses that may be distinguished in a mass spectrum; if $R = 100$ then two ion bunches flying into a detector will only appear as separate peaks if their masses differ by at least one part in 100.

To find the mass resolving power in terms of the time of flight, first we write down the time of flight for an arbitrary particle in terms of the mass and kinetic energy of the reference ion,

$$t(z) = z\sqrt{\frac{m}{2K}} = z\sqrt{\frac{m_r(1+\delta_m)}{2K_r(1+\delta_K)}} = t_r\left(1 + \frac{\delta_m}{2} - \frac{\delta_K}{2} + \cdots\right), \tag{2.42}$$

where t_r is the time of flight of the reference ion, m and K are related to the reference values through equations 2.12 and 2.11, and in the last step Taylor series are substituted for $\sqrt{1+\delta_m}$ and $1/\sqrt{1+\delta_K}$. The separation in time, $t - t_r$, between two ions is proportional to the relative mass difference between the ions; the scaling constant,

$$\frac{\partial(t - t_r)}{\partial \delta_m} = \frac{t_r}{2}, \tag{2.43}$$

is called the time of flight mass dispersion coefficient [63, ch 2.2.2]. The mass resolving power is the ratio of the ToF mass dispersion to the time width of an ion bunch arriving at a detector,

$$R = \frac{t_r}{2\Delta t}. \tag{2.44}$$

Δt corresponds to the full width at half maximum (FWHM) of a peak in the ToF spectrum. The time width of a single ion bunch can be determined to first order using the transfer matrix in equation 2.14,

$$\Delta\vec{r}(z_d) = \mathcal{T}_{0d}\Delta\vec{r}(0), \tag{2.45}$$

where $\Delta\vec{r}(0)$ is the initial spread in phase space coordinates and $\Delta\vec{r}(z_d)$ is the phase space width at the detector. Taking only the time coordinates,

$$\Delta t(z_d) = \Delta t(0) + \Delta\delta_K(0)\left|\frac{\partial t(z)}{\partial \delta_K}\right|_{z=z_d}, \tag{2.46}$$

where $\Delta t(0)$ is the turnaround time and $\Delta\delta_K(0)$ is the uncertainty in the initial energy spread. The $\partial t(z)/\partial\delta_m$ term is not present in equation 2.46 because ideally a single ion bunch arriving at the detector contains a single ion species, meaning that $\Delta\delta_m = 0$. The

mass resolving power for a ToF spectrometer is then

$$R = \frac{t_r/2}{\Delta t(0) + \Delta\delta_K \partial t(z_d)/\partial\delta_k}. \tag{2.47}$$

The form of $\partial t(z)/\partial\delta_K$ depends on the ion optics of the system; as shown in sections 2.3 and 2.4, it's possible to eliminate some of the δ_K terms from equation 2.42 by producing a high order time-energy focus at a detector. For example, assume that a ToF spectrometer has a third order time-energy focus, meaning that third order terms are eliminated and only the δ_K^4 term enters into equation 2.47. In that case, $\partial t(z)/\partial\delta_K \approx t_r\delta_K^3$. A well-cooled ion bunch in the TITAN MR-ToF might have an initial z width of about 0.3 mm[5]; if the kicking field is 100 V/mm and the drift kinetic energy is 1300 V, then $\delta_K \approx 0.023$. $\Delta\delta_K(0)$ is entirely due to the kinetic energy distribution of ions at the time they're kicked into the spectrometer. With an initially thermal ion population, $\Delta\delta_K(0)$ is the FWHM of a Maxwell-Boltzmann distribution, or about 0.4 eV at 300 K. $\Delta t(0)$ is the turnaround time, which was estimated at 5 ns in the last section. Plugging these values into equation 2.47 gives an estimate of the theoretical resolving power in the TITAN MR-ToF,

$$R = \frac{t_r/2}{5{\cdot}10^{-9} + t_r 5{\cdot}10^{-6}}. \tag{2.48}$$

For a ^{133}Cs reference ion, t_r is approximately $23n$ µs, where n is the number of turns in the analyzer (this time is estimated from figure 2.13); a plot of the Cs resolving power vs. turn number and time of flight is show in figure 2.16.

[5]A thermal ion bunch has the minimum size for a given applied potential. This width estimate comes from simulations of ion motion in the analyzer trap (see chapter 4). Experience shows that attempting to compress the ion cloud much further by changing potentials in the trap does not improve the mass resolving power.

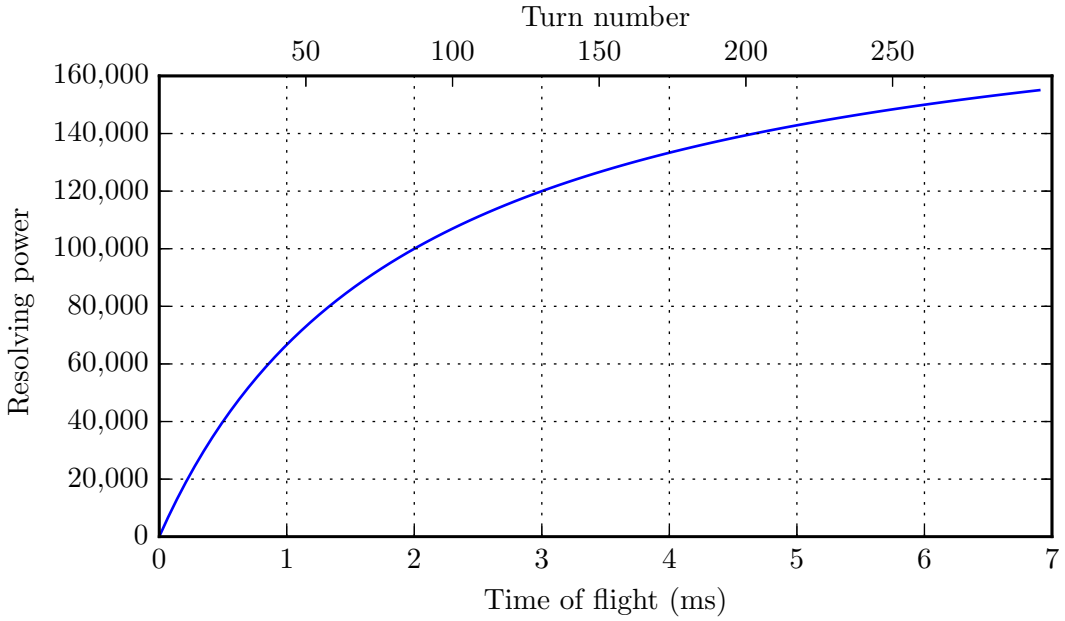

Figure 2.16: Theoretical resolving power of ^{133}Cs ions in the TITAN MR-ToF spectrometer (equation 2.48). The plot assumes 3rd order time-energy focusing and that the ToF for a single turn is 23 µs (estimated from figure 2.13)

Chapter 3

The TITAN MR-ToF spectrometer

The previous chapter discussed MR-ToF systems in general; this chapter gives details of the MR-ToF implemented at TITAN. The primary purpose of the TITAN MR-ToF is to filter single isobars out of a diverse ion population as quickly as possible. When operating as an isobar separator, ions enter from the TITAN cooler/buncher, fly through buffer gas to the Paul trap at the mass analyzer where they are re-bunched and cooled, then isobars of interest are re-trapped out of the full beam and transported to the horizontal section of the TITAN beamline. The MR-ToF will also provide destructive mass spectra at variable mass resolution. When operating as a mass spectrometer, ions are flown from the mass analyzer into a multi-channel plate (MCP) detector. Depending on the voltages applied to this detector, single ion signals may be as short as 1 ns. The detection efficiency of the MCP has not been measured.

The TITAN MR-ToF was designed and constructed by the IONAS group at Universiy of Giessen [34, 33]. As there wasn't room for an MR-ToF on the TITAN beamline when the TITAN-IONAS collaboration began, the MR-ToF had to be installed in an extension to the TITAN beamline rather than inline with existing ion optics. Space for such an extension is limited on the platform; there is only a narrow path for experimenters to walk around and access components, and vertical space over the platform is limited to a few meters because there must be room for a gantry crane to fly through. The IONAS group solved this problem with a buffer gas filled RFQ transport system which accepts ions from below, transfers them vertically to the MR-ToF, brings isobars of interest back down to a 90° switch (re-using a section of the beam path), and delivers ions to the TITAN platform perpendicular to their input direction (see figure 3.1). The cubic switch at the heart of the transport section was designed by the IONAS group in order to make the transport optics compact enough to fit into the TITAN beamline, and as far as we know it's the first device device of its kind. This is a compact solution for coupling the MR-ToF to the beamline, but the 90° switch (referred to here simply as *the cube*) also provides space to install a channeltron ion detector and a ^{133}Cs thermal ion source for calibration and diagnostics.

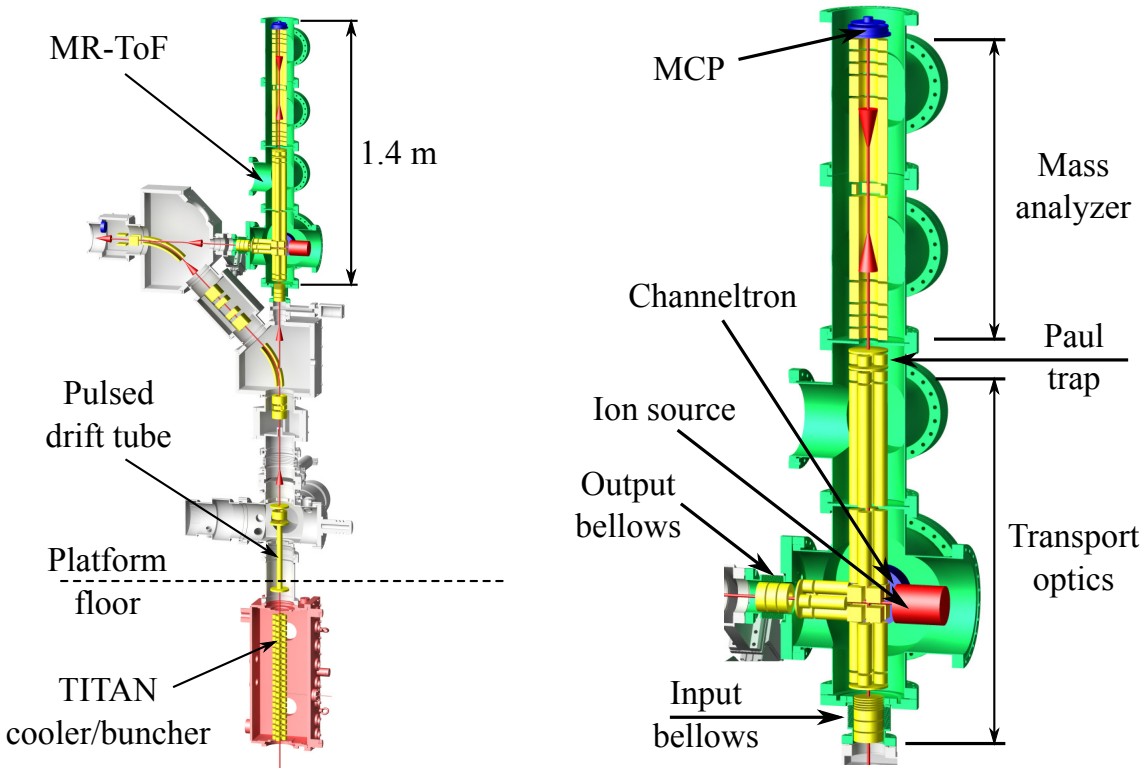

Figure 3.1: Left: schematic of the MR-ToF and its position on the TITAN beamline. Radioactive beam from ISAC enters the cooler/buncher and is then either transported directly to the Penning traps on the platform (through the two 45° benders) or vertically to the MR-ToF. The MR-ToF (green vacuum chamber) is not yet installed on the TITAN platform; it is currently mounted on the floor of the ISAC hall for commissioning. Right: overview of MR-ToF system components. Optics in the transport section deliver ions to the Paul trap and bring isobars of interest back to the TITAN beamline after retrapping. The mass analyzer performs multi-turn analysis, delivering ions either to an MCP detector which produces a mass spectrum or back to the analyzer trap for isobar separation. A ^{133}Cs ion source and a channeltron detector mounted to the transport optics provide internal calibration and diagnostics. Figures adapted with permission from [34].

The MR-ToF vacuum chamber is installed via two gatevalves, so the new spectrometer and its transport system may be completely isolated from the rest of the TITAN vacuum system. Complete vacuum separation means that the MR-ToF may be installed and operated using the internal ion source without interrupting normal operations on the TITAN platform.

During online operation, the transport optics will accept ions from the TITAN cooler/buncher. The buncher is elevated to 20 kV in order to slow the exotic beam from ISAC to tens of eV. A pulsed drift tube just downstream of the buncher sets the kinetic energy of the beam extracted from the buncher and shifts the reference electric potential of the ions to ground. When the MR-ToF is in operation, the kinetic energy of ions after the drift tube will be 1.3 keV. The drift tube in the MR-ToF spectrometer is fixed at ground, so the kinetic energy of ions entering the transport section sets the energy of ions during mass analysis. As discussed in the previous chapter, higher kinetic energy in the MR-ToF analyzer allows shorter initial ion bunches and therefore higher mass resolution at shorter times of flight; 1.3 keV is the highest practical kinetic energy for MR-ToF mass analysis at TITAN because the control electronics for the mass analyzer may break down at the potentials required for higher energies.

For commissioning, the MR-ToF is mounted on the floor of the ISAC I experimental hall. Photos of the current setup are shown in figure 3.2. Extensions to the vacuum chamber were installed at the input and output bellows (see figure 3.3); the input extension contains a thermal ^{133}Cs ion source which simulates beam from the TITAN buncher, and the output extension contains an ion detector which was meant to characterize the output optics in the transport system. Unfortunately, the output detector required maintenance and was not operational during the time we could have used it for this work.

3.1 Vacuum system

Figure 3.3 shows several photos of the MR-ToF vacuum chambers. The vacuum system is roughly divided into three sections: the transport section, the trap section, and the analyzer section (see figure 3.4). The transport and trap sections each contain encapsulated buffer gas.

the buffer gas encapsulation around the transport optics, a high vacuum region in the transport section, and a high vacuum region around the mass analyzer (see figure 3.4). There are three 1.5 mm differential pumping apertures from the buffer gas volume into the high vacuum area around the transport system, and a single aperture connecting the two high vacuum regions. Turbomolecular pumps backed by a scroll pump maintain pressure in the vacuum vessel (see table 3.1).

The base pressure for the entire system with no gas load is in the low 10^{-7} to high 10^{-8} mbar range. With buffer gas, the transport section is in the low 10^{-2} mbar range and the high vacuum regions are in the mid to high 10^{-7} mbar range. In addition to the hot

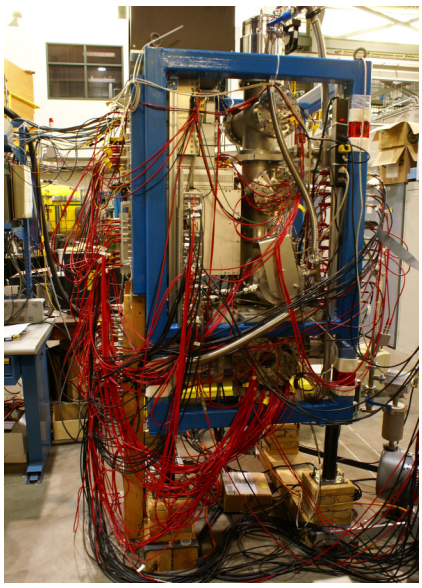

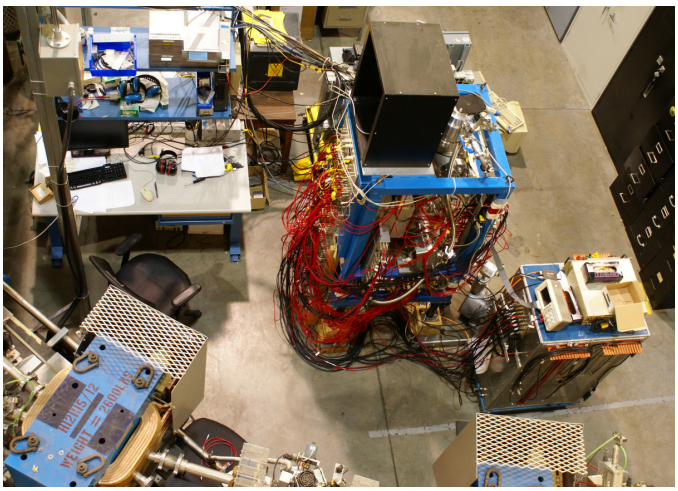

Figure 3.2: Left: the TITAN MR-ToF during commissioning. The blue frame will be separated from the black legs when the system is installed on the TITAN platform; the legs below the frame provide clearance for the input extension to the vacuum chamber. A stack of HV switches is mounted inside the frame on the left-hand side (see section 3.8). Right: commissioning work area. The unit to the right of the MR-ToF is a Faraday cage enclosing power supplies for the transport optics which are floating at 1.3 kV (see section 3.7).

Section	Base [mbar]	Operating [mbar]	Pump speed [l/s]
Analyzer	$1.0 \cdot 10^{-8}$	$1.4 \cdot 10^{-7}$	550
Trap (vac)	$6.2 \cdot 10^{-7}$	$4.2 \cdot 10^{-5}$	550
Transport (vac)	$6.5 \cdot 10^{-7}$	$1.0 \cdot 10^{-4}$	1000
Trap (gas)	$7.1 \cdot 10^{-6}$	$7.6 \cdot 10^{-3}$	
Transport (gas)	$1.2 \cdot 10^{-6}$	$3.0 \cdot 10^{-2}$	

Table 3.1: Pressures in the vacuum sections illustrated in figure 3.4. Lines marked (vac) are from gauges outside the buffer gas encapsulation, lines marked (gas) are from gauages inside the gas encapsulation. Base pressures are without buffer gas, operating pressures are for typical gas loads in the transport and trap sections. Pumps are Varian Navigator TV551 and TV1001.

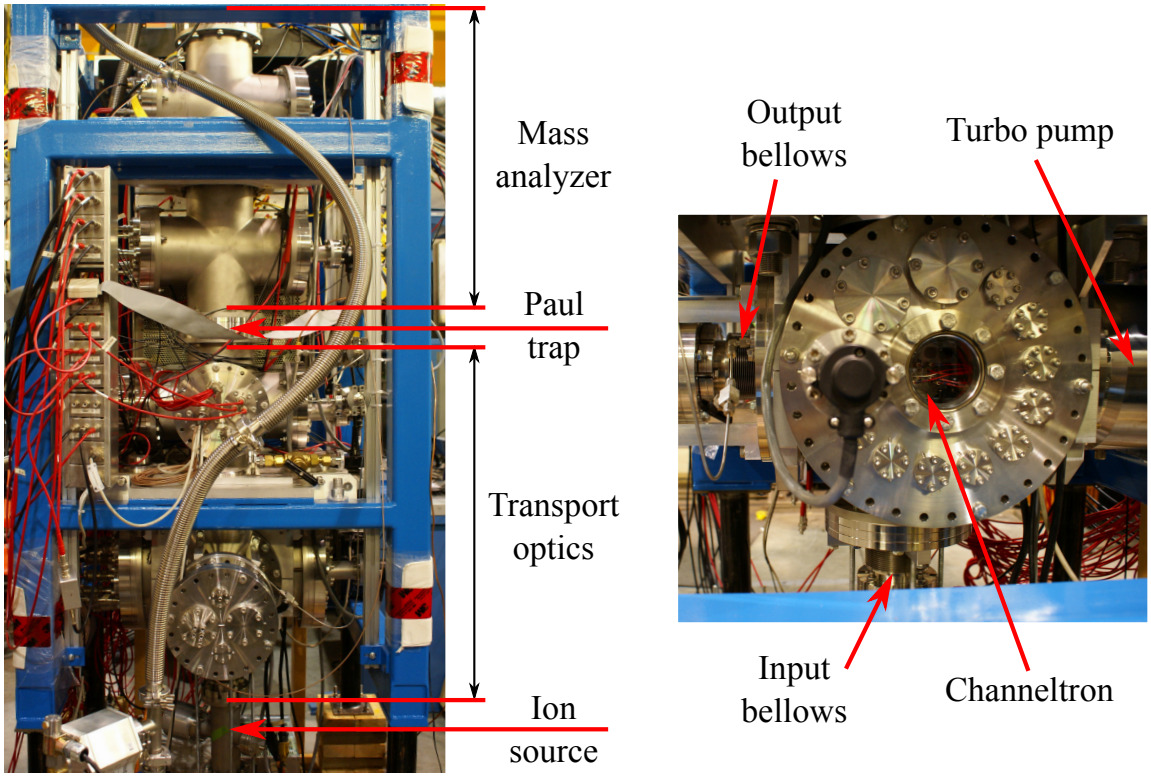

Figure 3.3: Left: photo of the MR-ToF vacuum chamber for comparison to figure 3.1. The input extension housing the commissioning ion source is shown at the bottom and the output extension faces the viewer. Right: detail of the lowest vacuum cross. The cube sits at the center of this chamber, and wires coming out of the channeltron detector is visible through the window.

cathode ion gauges shown in figure 3.4, two MKS MicroPirani gauges provide buffer gas pressure readout while the MR-ToF is in operation. The ion gauges attached to the buffer gas section are wide range gauges capable of monitoring the gas pressure, however they generate a copious ion background which is captured in the transport ion optics.

3.2 Transport ion optics

The following three sections provide detailed diagrams of ion optics for transport and mass analysis. These diagrams are based on mechanical drawings; details such as feedthroughs and fasteners have been removed.

The transport system consists of three RFQs which meet at the cube (see figure 3.5). There are additional optics for deceleration, steering, and spatial focusing outside the buffer gas encapsulation near the input and output RFQs (see figure 3.6). The RFQ electrodes are cylindrical rods 13 mm in diameter with a clear space of 5 mm between the axis of the RFQ and the surface of a rod. The electrodes are continuous carbon-filled polyether ether ketone (PEEK) rods with stainless steel electrical contacts screwed into the ends. PEEK

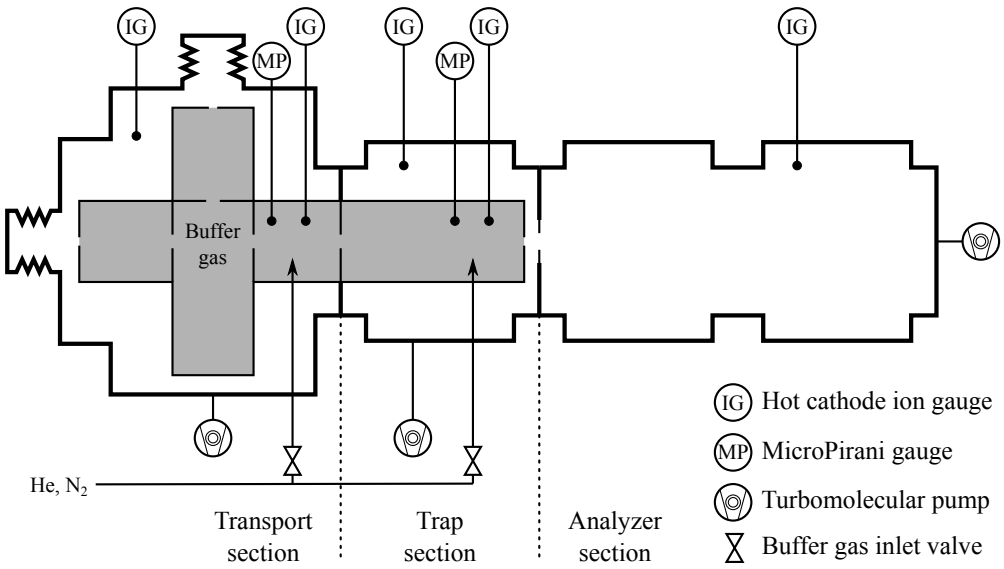

Figure 3.4: Schematic of the MR-ToF vacuum system. Apertures inside the gas encapsulation are 1 cm in diameter, differential pumping apertures at the edge of the gas encapsulation are 1.5 mm, and the aperture between the trap section and the analyzer is 2 mm.

is a structural plastic used in vacuum applications and it's typically an electrical insulator, but the carbon fill gives it some conductivity. One can therefore complete a circuit using the stainless contacts and run a current through the rods. Since electrical resistance is distributed throughout the electrode volume (about 10 Ω/cm for these rods), there will be an approximately linear voltage drop between the stainless contacts. This is a convenient method to produce transport potentials in RFQ ion guides because it requires only two DC voltages and it eliminates the resistor chain required for segmented RFQs. The PEEK used in the rods is not manufactured for electrical components, so the carbon fill may be inhomogeneous and leave spots on the surface with nearly zero conductivity. If this were the case, static charge could build up on the spots and distort applied ion optical potentials. To eliminate this possibility, the rods are coated with a spray-on carbon lacquer which creates a conductive surface layer.

The cube is an RFQ switch capable of accepting or transmitting ions from any side, and it may accept or transmit ions from multiple sides at once to split or combine beams. It consists of 8 carbon-filled PEEK electrodes which have a tripod structure with three orthogonal legs. Each leg is capped with a stainless steel contact and the contacts are captured in a non-conductive PEEK shell. Just like a normal RFQ ion guide, the cube takes two RF signals 180° out of phase with each other and distributed as shown in figure 3.7. Each cube face has four stainless steel contacts which all receive the same static potential in addition to their RF signals. There are three static potentials applied to the cube faces; one high, one mid, and one low. To transport ions straight through the cube, the input face is set high, the output face is set low, and the other faces get the mid potential. To transport

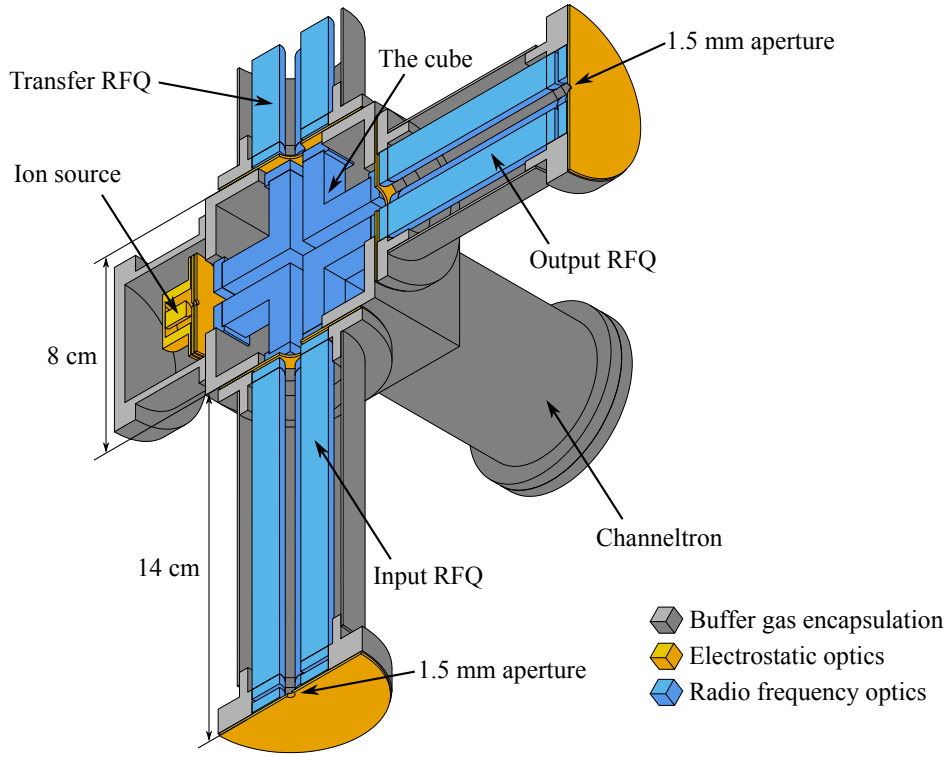

Figure 3.5: Radio frequency ion optics in the transport section. The transfer RFQ is 47 cm long and extends to the Paul trap at the mass analyzer. 1.5 mm apertures at the outside end of each RFQ define electric potentials and serve as differential pumping apertures for the buffer gas.

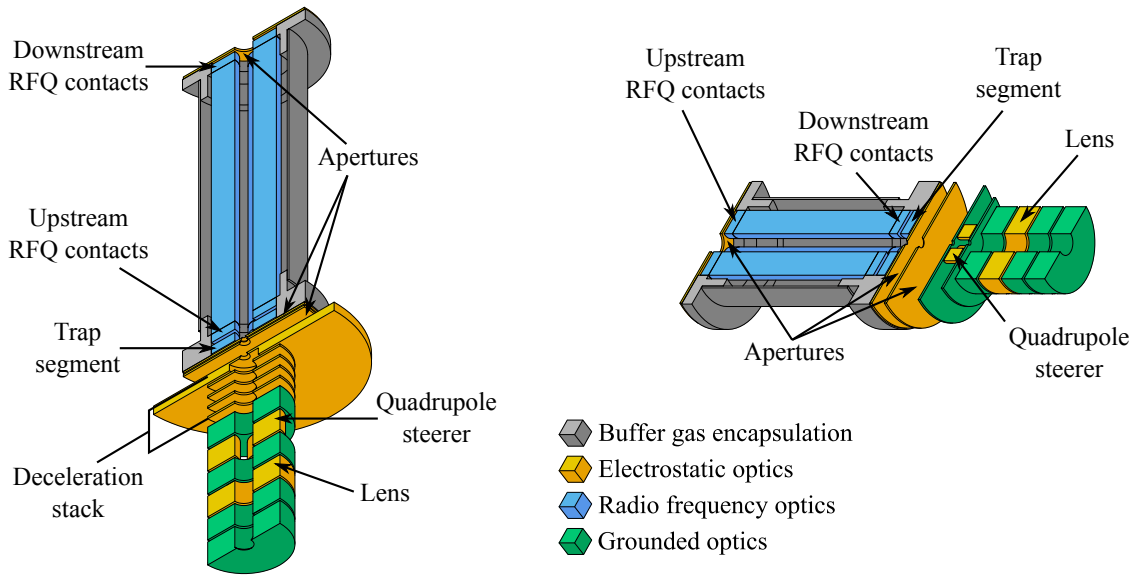

Figure 3.6: Left: input ion optics. The deceleration stack applies a linear retarding field which slows ions to a few eV. Right: output ion optics.

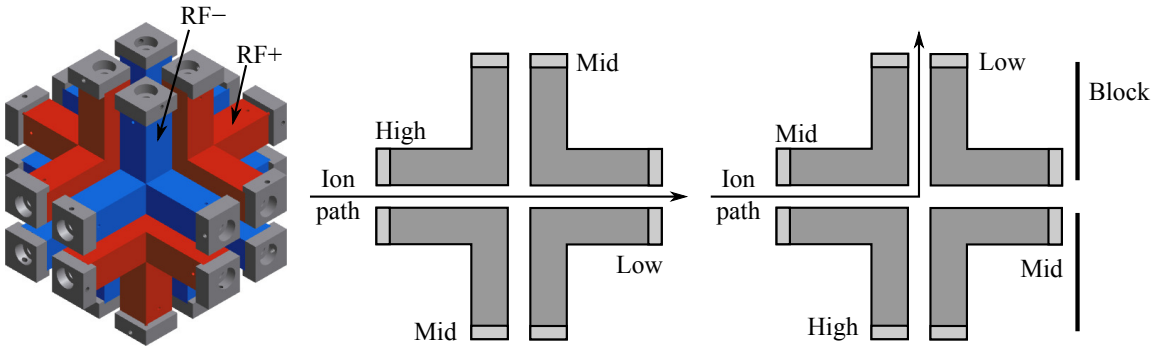

Figure 3.7: Electric potentials in the cube. Left: distribution of the two RF phases over the cube electrodes. Center: DC potentials used to transport ions straight through the cube from left to right. Right: DC potentials used to transport ions around a corner from left to the top of the figure (see text for details).

ions 90° around a corner, one configures the cube electrodes as if ions were transported straight to the desired output face and sets an additional blocking potential outside the cube opposite the input. That is, ions enter the cube at the mid potential and an extra element outside the cube prevents them from flying straight across the cube and out the other side. In this configuration, ions reflect between two cube faces at mid potential a few times before settling into the output channel. Assuming the low cube face is at zero volts, typical mid, high, and blocking potentials are 5, 10, and 60 V. The two cube configurations are illustrated in figure 3.7.

During isobar separation, ions traverse the cube and the transfer RFQ twice; the initial ion bunch has to go up to the analyzer and then isobars of interest travel back down and turn a corner into the output RFQ. This process decouples the MR-ToF duty cycle from the TITAN buncher. An ion bunch is admitted into the cube from the input RFQ by switching the aperture between them low for a few microseconds; otherwise the aperture is held high so that ions accumulate in the input RFQ without entering the cube. The repetition rate of the MR-ToF (the number of times per second the cube is opened for another shot into the mass analyzer) is then completely independent of the rate the TITAN buncher sends ions into the MR-ToF transport system. The duty cycle of the MR-ToF is also independent of duty cycle for the Penning traps; a segment at the end of the output RFQ creates a trap small enough to send sub-microsecond ion bunches on to the next element on the TITAN beamline, and this output trap can accumulate ions for an arbitrary period before kicking a bunch on to the rest of the platform. These features mean that the repetition rates into and out of the MR-ToF can be tuned for optimum efficiency.

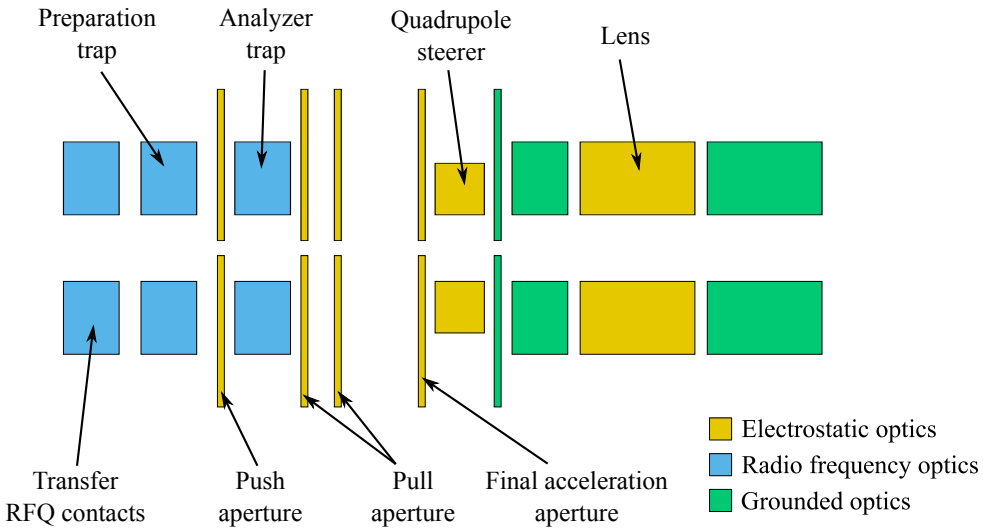

Figure 3.8: Schematic of trapping optics for MR-ToF mass analysis. The push, pull, and steering apertures form a two stage acceleration potential which kicks ions out of the analyzer trap. The buffer gas encapsulation ends at the upstream pull aperture, and the trap and vacuum sections of the vacuum system meet at the downstream pull aperture (see figure 3.4).

3.3 The trap system

The trap system which prepares ions for mass analysis is at the end of the transfer RFQ (see figure 3.8). An ion bunch elongates during transit through buffer gas, so a stainless steel segment just downstream of the transfer RFQ rods forms a preparation trap in which ions are re-bunched after passing through the RFQ. Accumulation from the transfer RFQ and cooling in the analyzer trap both occur in the trapping potential shown in figure 3.9. Once ions have formed a single cloud in the preparation trap, the aperture between the traps is switched to create the loading potential shown in figure 3.9; the loading potential is applied for microseconds and then the trapping potential is re-applied to capture and cool ions in the analyzer trap. The transfer operation between the traps is mass dependent and the timing of the loading operation must be adjusted for the mass range of interest, however the mass range captured by a single timing value is tens of amu. The loading time for ^{133}Cs (optimized using the relative intensity of ions passing through the analyzer after cooling) is approximately 5.7 µs. Since heavier ions travel between traps more slowly than light ions, the loading time for an ion of mass A is scaled by $\sqrt{A/133}$.

After cooling, the push aperture between the preparation and analyzer traps is switched to a high voltage, the pull aperture just downstream of the analyzer trap is switched low, and ions are kicked out of the trap using a two stage accelerating potential like the one described in section 2.4. The kicking potential is shown in figure 3.10. The figure shows two approximately linear fields corresponding to the two acceleration stages. The pull aperture is

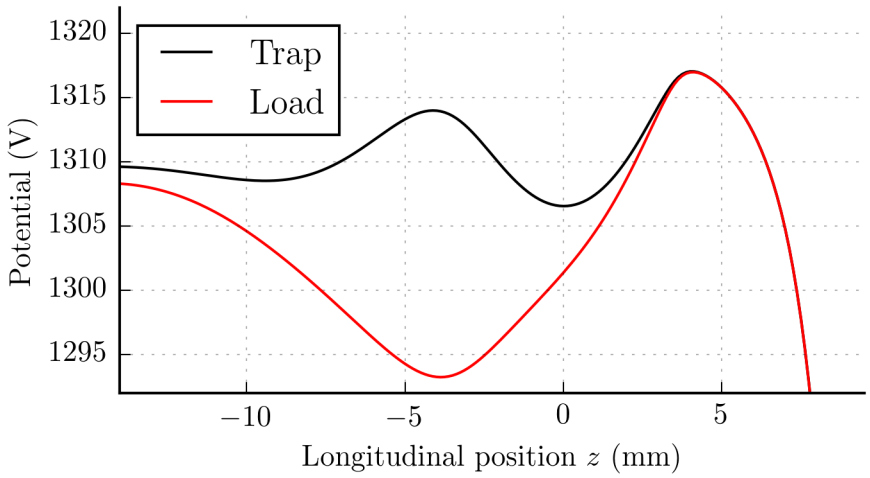

Figure 3.9: Simulated longitudinal electrostatic potentials used to load ions into the main trap from the preparation trap and then cool them. Half of a cross section of the ion optics in this region is shown for reference; colors are the same as in figure 3.8.

actually two aperture plates at the same potential which are separated by a few millimeters. This produces a region with nearly zero field between the two acceleration stages which acts as a spatial lens. In contrast to the simple two-stage acceleration described previously, the second acceleration stage out of the analyzer trap drops below the drift potential (0 V). The deceleration back to ground potential creates an additional spatial lens at the quadrupole steerer.

3.4 The mass analyzer

The mass analyzer is a cylindrically symmetric stack of nine stainless steel electrodes; the four electrodes at each end of the stack make up the mirrors and the central electrode is the drift tube (see figure 3.11). Circular baffles inside the drift tube reject ions which are so far away from the optic axis that they cannot be properly focused; these ions would have a longer time of flight than ions close to the optic axis, which would reduce the mass resolution or possibly lead to misidentification. The quadrupole steerer at the center of the drift tube is called the mass range selector (MRS) and it serves two purposes. First, in combination with the steerer and lens upstream of the mass analyzer, this steerer can produce ion trajectories which are both centered on the optic axis and parallel to it. Second, one can use the MRS to select an ion of interest by steering unwanted ions into the baffles. This is convenient because it only requires calculating when the ion of interest will pass by the MRS. One then applies a steering field for several turns and only switches it off for short windows to allow ions of interest through. The MRS is not precise enough to separate isobars because the time required to switch the steering field on or off is a few

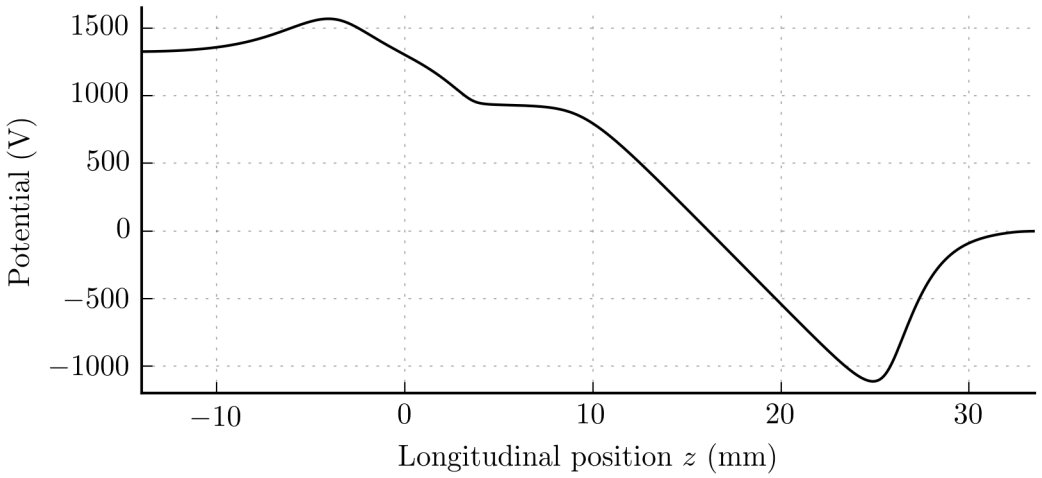

Figure 3.10: Simulated on-axis electric potential used to kick ions out of the analyzer trap.

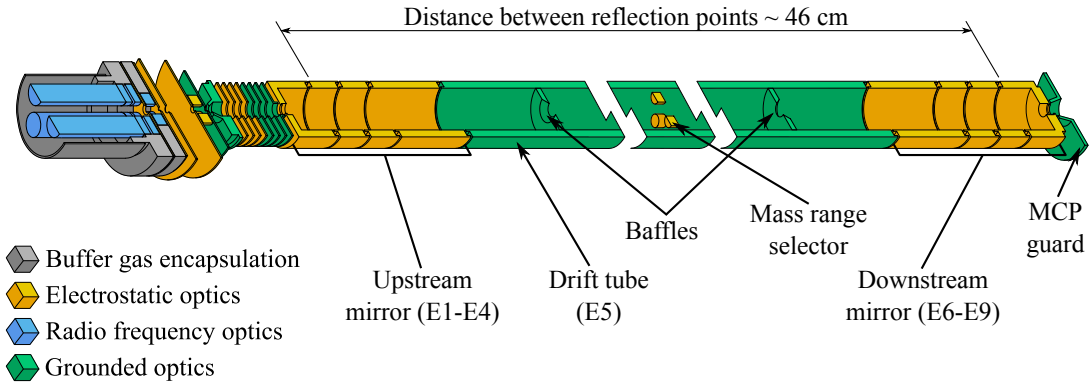

Figure 3.11: The full MR-ToF, including the trap system and the mass analyzer (image not to scale). Mass analyzer electrode designations are E1–E9, where E1 is the upstream endcap, E5 is the drift tube, and E9 is the downstream endcap.

hundred nanoseconds, but even after hundreds of turns in the analyzer the time between neighboring isobars is only tens of nanoseconds; one can't accept an isobar of interest using the MRS without also accepting contaminant isobars. While the MRS can't select isobars, it is helpful to remove potentially large contamination from ions at least 1 amu away from the ion of interest because in extreme cases space charge from ions in the analyzer may affect ion optical fields.

To operate the TITAN MR-ToF, the drift tube is held fixed at ground potential and the mirror potentials are switched between three states: open, time focus shift (TFS), and multi-turn (MT). The principles of MR-ToF mass analysis are described in sections 2.5 and 2.7; mass analysis in the TITAN system is performed using the potentials shown in figure 3.12. For an ion kinetic energy of 1.3 keV, the distance between turnaround points in the mirror potentials is about 47 cm so the ion flight path for a full turn is approximately

one meter. That means that in a typical high resolution mass spectrum produced with the TITAN MR-ToF, every detected ion travels more than 200 meters through the analyzer.

3.5 Timing

Switching times in the TITAN MR-ToF are set with custom control software produced by our collaborators in Germany which runs a field-programmable gate array (FPGA) with 32 outputs for logic-level trigger signals. The FPGA has a clock frequency of 200 MHz (5 ns resolution) and the on-board program can set a constant delay between two triggers, it can set periodic triggers, or it can send a trigger signal determined by boolean operations on other trigger states. The trigger system and software have been discussed in previous publications [31, 32]; this section only provides an outline of the timing scheme used in the TITAN MR-ToF.

During this work, the thermal ion source upstream of the input optics was run with a roughly constant ion current. The ion optics for the input source are identical to those for the diagnostic source shown in figure 3.5, and the ion current entering the input RFQ was regulated by switching an aperture on the source to allow ion bunches through at a few hundred Hertz. This produced an approximately constant ion current at the input optics which could be regulated using the switching frequency at the input source. Ions were stored in the input RFQ using the cube aperture on the input side (see figure 3.5). During online operation the input RFQ will operate slightly differently; instead of remaining open at the input end to accumulate ions, an aperture at the input side of the RFQ will be switched to a high potential to dynamically capture an input bunch from the TITAN buncher.

The duty cycle for a shot through the mass analyzer begins by switching the aperture between the cube and the input RFQ low to allow ions into the cube. Simulations show that ions take a few hundred microseconds to pass through the cube and accumulate in the preparation trap, then they're loaded into the analyzer trap and cooled. The typical times used in this work were about one millisecond for accumulation and three milliseconds for cooling. After cooling, ions are kicked into the mass analyzer and fly for tens of microseconds to about three milliseconds. After mass analysis, either the upstream mirror is opened for retrapping or the downstream mirror is opened for mass spectrometry. If the upstream mirror is opened, ions are captured in the analyzer trap and re-cooled. They're then loaded back into the preparation trap and the gradient on the transfer RFQ is reversed for transport back upstream to the cube and on to the output RFQ. Alternatively, re-cooled ions may be kicked into the mass analyzer a second time. This may be useful in cases where the ratio between contaminant ions and ions of interest is so high that either the detector would be swamped with contaminants or it would be impossible to retrap the species of interest without also capturing a significant amount of contaminant ions.

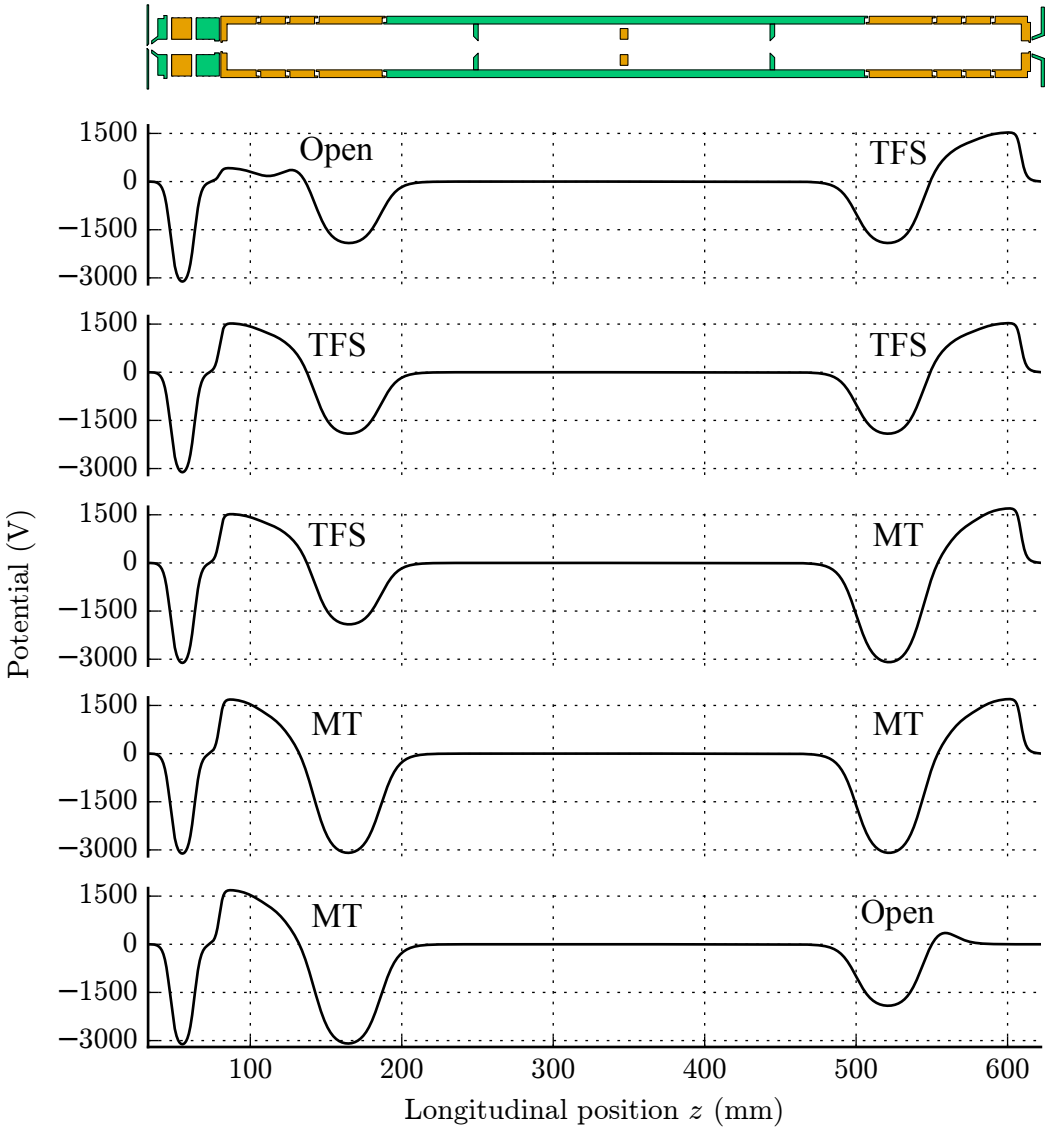

Figure 3.12: Simulated on-axis electric potentials in the mass analyzer at each stage of analysis. The state of the mirrors is indicated in each plot (see text for details). A cross section of the analyzer is shown for reference; colors are the same as in figure 3.11, but the upstream lens has been simplified. These potentials implement the schematic shown in figure 2.10. The mirror potentials include accelerating lens potentials which maintain spatial focusing after each reflection.

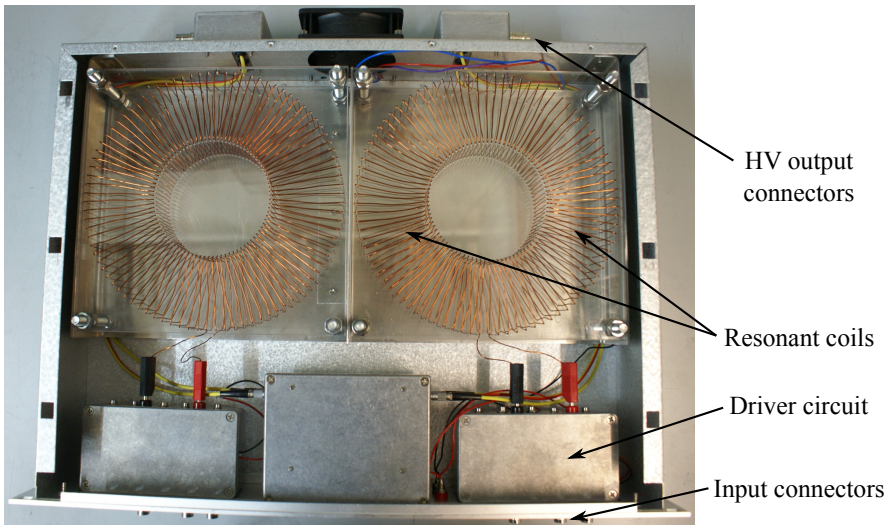

Figure 3.13: Photo of one of the RF generator units. Each 19" rack mount chassis contains two generators; components of one of the generators are labeled on the right. Coaxial cables which complete the resonant circuit are not shown.

3.6 RF voltage supplies and RF/DC mixing

The radio frequency signals for the RFQs, the cube, and the Paul trap come from three independent resonant LC circuits (sometimes called "tuned" or "tank" circuits). A photo of one of the RF generator units is shown in figure 3.13. Each generator consists of a pair of air-core coils in a toroidal configuration attached to coaxial cables which carry the signals to the vacuum chamber. The coils are inductors which resonate with the coaxial cables' intrinsic capacitance to ground. The toroidal shape confines magnetic flux inside the coils and reduces effects from nearby objects which could shape the magnetic field and create interference. Custom driver boards produced by our collaborators in Germany take a TTL square wave and a constant voltage input of 0–15 V or so. The drivers amplify the square wave in proportion to the DC input, smooth it, and then split it. Nearly sinusoidal waves 180° out of phase are fed from the driver board into the two coils, which are wound such that the magnetic flux in the two coils forms a continuous circle around the torus. When the center frequency of the input square wave is on resonance with the LC circuit, the RF generator can deliver two highly sinusoidal signals which are phase locked 180° apart with peak-to-peak amplitudes of hundreds of volts.

The resonant frequency of an RF generator is fixed by the coils, the cables, and the capacitance of the ion optics inside the vacuum chamber. To operate an RF generator, the frequency of the square wave input is tuned to resonance and then the DC input value is tuned to adjust the output amplitude and tune the Mthieu satbility parameter of one of

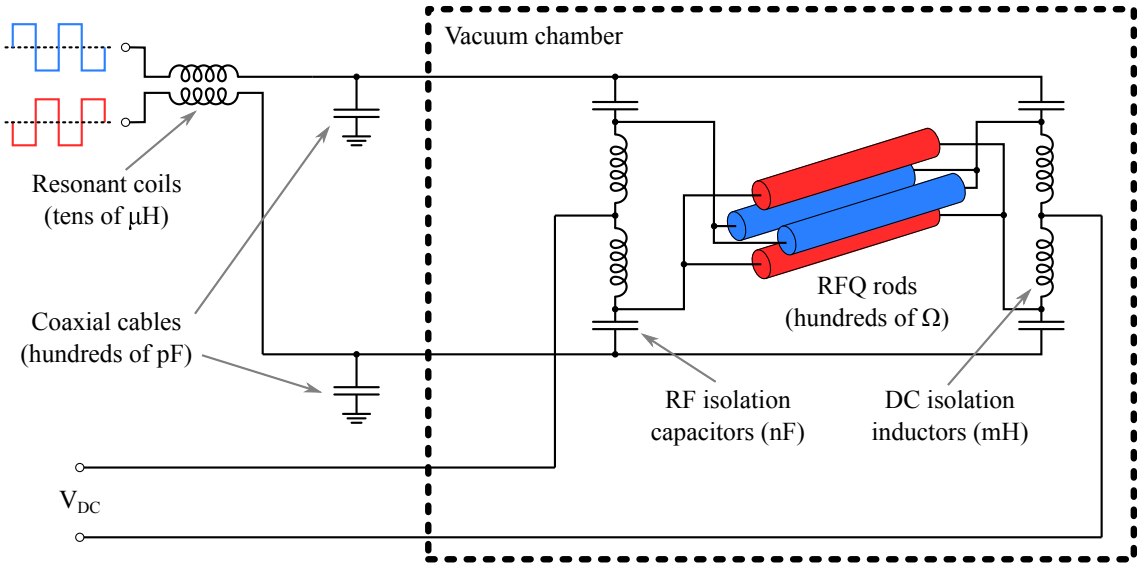

Figure 3.14: Wiring diagram of an RFQ with continuous rods. The coaxial cables and the air-side coils form a resonant circuit which converts TTL square waves into high voltage sinusoids. Inductors in vacuum prevent RF signals from propagating back to the DC power supply, while in-vacuum capacitors keep direct current from flowing to the RF generator.

the RF optics (see section 2.1). Resonant frequencies in the TITAN MR-ToF transport and trapping optics are 1–1.5 MHz and peak-to-peak amplitudes range from about 50 to 400 V.

The RF generators produce sinusoidal signals about ground voltage, however the static voltages for ion transport in the TITAN MR-ToF must be around 1.3 kV in order to trap ions at high voltage and perform mass analysis at ground potential. To reduce the number of external feedthroughs on the vacuum chamber, the RF signals are combined with static voltages from high voltage supplies on RF/DC mixing boards inside the vacuum chamber. A diagram of the full wiring for one of the RFQs is shown in figure 3.14.

3.7 Static voltage supplies and distribution

There are approximately 40 static voltages applied to ion optics in the TITAN MR-ToF at any given time. Except for RF signals, all voltages come from static supplies; switching is achieved by wiring multiple static supplies to a high voltage switch whose output is connected to an ion optical element (see next section). All voltage supplies for ion optics in this system are modular units installed in MPOD crates from Wiener. We purchased high voltage supplies manufactured by iseg and the low voltage floating supplies are from Wiener.

Each potential in the mass analyzer is set with an independently tunable power supply. The most sensitive values are the mirror potentials which must preserve time foci throughout multiple reflection analysis; changing the mirror voltages by a few parts in 10^5 will have an

impact on the mass resolving power (that's tens of millivolts on a 1 kV nominal voltage). Electrodes in the mass analyzer therefore have additional passive filtering to reduce electrical noise during mass analysis. The mirror voltages are stabilized with fifth order low-pass filters which are installed in 19" rack mount units outside the vacuum chamber; the filters are in series with the analyzer optics between the electrodes and the HV switches.

Static voltages in the transport system are set up using floating supplies which apply a constant offset voltage between two points. This is convenient because it allows the operator to set things like the transport gradient on an RFQ and the voltage offset between an RFQ and the next downstream element without keeping track of absolute voltages. Since cube and the RFQs have current-carrying elements and the resistance of one RFQ rod is hundreds of Ohms, the steady-state current drawn by the RFQs and the cube from static voltage supplies is hundreds of milliamps. Floating power supplies within the initial budget of this project could only deliver such high currents at up to about 400 V relative to the ground potential of the power supply crate. The initial plan for the TITAN MR-ToF was therefore to float the transport system to about 350 V and put the drift tube at -300 V so that the kinetic energy of ions in the drift tube was 650 eV, or half the design value. All voltages in the mass analyzer were then scaled by a factor of one half.

In order to bring the system up to its full kinetic energy, we had a Faraday cage produced which could fully encapsulate one of the Wiener crates and float the ground on its AC power input to 1.3 kV using an isolation transformer. This system uses an additional high voltage channel for the floating "ground" potential but it can deliver a combined current of more than ten amps which is then distributed between the transport optics and the thermal ion sources, all at an operating voltage of around 1.3 kV. The Faraday cage is shown in figure 3.2.

In addition to the Faraday cage, a patch panel was produced and installed during this project to simplify high voltage distribution. There are many points in the wiring of the TITAN MR-ToF where a single supply voltage must be distributed to multiple locations. For instance, any time an optical element receives a voltage from a chain of floating power supplies, at least a "T" junction is required; one cable comes from the positive terminal of a floating supply, one cable goes to a vacuum feedthrough, and one cable goes to the negative terminal of the next floating supply in the series. Some floating voltages in the transport system are distributed to up to five different vacuum feedthroughs, requiring a total of seven SHV cables which all carry the same voltage. Accounting for power supply connectors, junctions, and feedthroughs, there are over 100 connections in the system. Additionally, some junctions require simple circuits to drain current to ground or reduce noise. In order to make the wiring more manageable, we produced an electrical panel which provides "patches" of 3–8 SHV connectors wired together internally; the operator connects a power supply to one connector and then the rest of the connectors on the same patch are available to distribute the supply voltage to multiple locations. The unit is fully enclosed and the

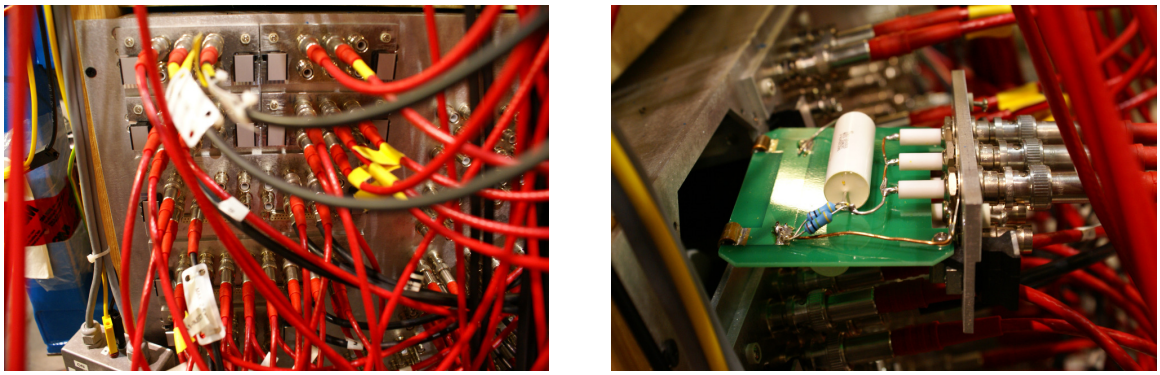

Figure 3.15: Left: partial view of the patch panel. Modular patches are shown in the center of the image and some simple patches are visible on the right side of the panel. Each row of connectors on the modular patches (each column for the simple patches) are wired together to deliver the same voltage. Right: a modular patch with three connectors. A second three-connector patch on the same module is wired to the bottom of the circuit board. Copper barrels on the rear edge of the circuit board connect to a ground plane when the module is inserted into the panel. The circuit shown provides additional filtering for electrodes in the analyzer.

patches can safely hold ±10 kV. The patch panel also has modular patches wired to circuit boards which may be removed from the panel for easy installation and modification of circuit elements. A photo of the patch panel and one of the modular patches is shown in figure 3.15.

3.8 High voltage switching

Switching in the TITAN MR-ToF is performed with custom push-pull amplifiers designed and built by our collaborators. Each switch has three inputs and one output; the inputs are two static voltages and a TTL signal. When the TTL input is high, the ouput voltage is the higher of the two static inputs and when the TTL is low the output is connected to the lower input voltage. If more than two voltages are required, switches may be stacked together by wiring the output of one switch to the input of another, however some on-board capacitors must be removed from one of the switches.

To switch the voltage on an electrode, charge must be supplied to or removed from the electrode and the cables between the electrode and the switch. The time required to change from one static voltage to another is then partially determined by the amount of current flowing through the switch; the higher the current the shorter the switching time. In reality the current in the switches must be limited because the transistors in a push-pull amplifier (or circuit elements in any switch) can only handle a certain amount of current before burning out. A load resistor at the output stage of the switch acts as a current limiter to protect the switch but it also increases the switching time. The length of coaxial cable

between the switch and the electrode in vacuum also affects the switching time and the required current; longer cables have more capacitance and therefore require more charge to bring the electrode up to full voltage. Switches are mounted to the frame of the MR-ToF vacuum chamber in order to keep the output cables as short as possible (see figure 3.2).

Typical switching times in the TITAN MR-ToF are hundreds of nanoseconds. This is an acceptable time scale in the mass analyzer because only the mirror fields are switched, and once an ion bunch leaves a mirror there are at least a few microseconds to switch and stabilize a mirror field before the bunch returns. This is not the case in the trap system; when ions are kicked out of the trap or retrapped after returning from the mass analyzer, they see a changing field throughout the switching operation. If ions move much more than the width of the ion cloud during switching, the initial phase space of the ions is distorted and the mass resolving power is reduced[1]. The switching time on the apertures around the analyzer trap therefore needs to be shorter than the average time required for an ion in the trap to travel a few hundred µm. Since this isn't a directly measurable quantity, we optimized the analyzer trap switching time by checking the resolving power for different load resistances (see section 5.7)

[1]The effect is similar to increasing the length of the ion cloud at the beginning of mass analysis (increasing z_0 in figures 2.6 and 2.7

Chapter 4

Simulations

A detailed description of ion motion in electromagnetic fields is required for the design and implementation of ion optical systems. There are only a few cases in which ion trajectories can be described analytically; for instance a parabolic electric potential along one axis leads to harmonic oscillation of charged particles, and radio-frequency quadrupole fields confine ions within approximately harmonic potentials in multiple dimensions [12]. Even in cases where nearly analytic fields can be generated with experimental apparatus, real geometries of machined electrodes or magnetic pole faces lead to deviations from ideal fields. Since these deviations are important for experimental design and because many ion optical systems generate fields which are not even approximately analytic, numerical simulations of particle trajectories are a common component of nuclear physics experiments at accelerator facilities.

Any simulation of ion motion consists of two parts: a calculation of electromagnetic fields and an iterative calculation of velocity vectors for ions in those fields. The idea is to calculate a velocity from the potentials an ion sees at a given time and position, move the ion along its velocity vector during some time step, recalculate the velocity at the new position, and iterate. In this chapter I report on simulated data produced with SIMION 8.1 [10]. SIMION provides tools to produce both electromagnetic fields and particle trajectories.

Electric potentials are calculated in SIMION using finite difference methods. A user first defines a coordinate grid for the simulation space and then defines which points on the grid are inside electrodes. Once SIMION knows where the electrode points are, it steps through sets of points the user has defined as independent electrodes, defines those points as boundary values of 1 V, and then takes successive averages of potentials at neighboring points outside the electrodes. This is a well known method for approximating the Laplace equation which defines electric potentials in free space [24, section 3.1]. The result is an electric potential from each independent electrode defined over the whole simulation space. Since the Laplace equation has unique linear solutions [24], all these 1 V potentials can be scaled by desired electrode voltages and summed up to define a potential for the whole system. This method allows for "fast adjustment" of electrode potentials at each simulation time step because the potentials can be scaled independently without solving the Laplace

equation all over again. After refining electrode potentials, SIMION can perform discrete time integration of forces on charged particles to determine their trajectories through the simulation space.

Radio frequency fields in the MR-ToF transport section are produced by applying a constant voltage to RF electrodes and adding a sinusoidal signal which is updated at each time step. In the real setup, longitudinal transport fields are produced in the RFQs and the cube by running a current through carbon filled PPS electrodes (see section 3.2). It's possible to simulate the voltage drop along the plastics in the RFQs by slicing a perfectly conductive rod into many segments and applying different voltages to each segment. This method is not a good approximation for complex geometries like the cube electrodes. As shown in figure 3.5, there is a sharp point where the three legs of a cube electrode come together. The current density in a dielectric is a solution to the Poisson equation, so the electric current goes to zero at the point of the cube electrodes because the curvature of the surface diverges. The voltage drop along the surface of the cube electrodes is clearly not a simple function, so the fields in the cube should be found from a numerical approximation of the current density produced in the real electrodes.

SIMION 8.1 provides a Poisson solver which can take two 3D arrays as input; one defines points associated with perfectly conductive geometry where voltages are constant when applied to an electrode surface and the other defines the permittivity of material outside the electrodes. SIMION then produces a solution for the electric field everywhere outside the conductive electrodes. This is the method used in the current work to define fields in both the cube and the RFQs; a steady-state solution for the current density is found using SIMION's Poisson solver and the resulting electric potential is scaled by the (RF + DC) voltage applied at the stainless contacts. The nearly insulating plastics which form the shell of the cube and the support structure for the gas encapsulation are also included in the simulation geometries. These components were included because they are dielectrics which could have some effect on field penetration through apertures.

The MR-ToF mass analyzer is a set of cylindrically symmetric stainless steel electrodes which see very low ambient gas pressure, and it's designed such that ions should never see time-varying fields. This environment is about as close as one can get to an ideal analogue for simulated ion motion. However, any MR-ToF mass analysis depends critically upon well defined ion bunches, which means trapping ions in some lossy medium for cooling. In practice ions are cooled through collisions with buffer gas, which is a stochastic process. The phase space volume occupied by cooled ions can be approximated with damped oscillations during trapping, however this method ignores real ion trajectories due to random collisions which could potentially lead to loss of ions. Since complete operation of the TITAN MR-ToF also relies on buffer gas cooling throughout the transport system, especially in the cube, a more accurate simulation of collisional cooling will lead to a deeper understanding of the system. To that end, I implemented a detailed simulation of ion collisions with buffer gas.

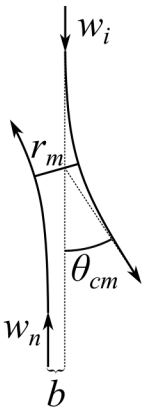

Figure 4.1: A two body, center of momentum collision under a central potential. w_i and w_n are incoming ion and neutral speeds in this reference frame, b is the impact parameter, θ_{cm} is the scattering angle in this reference frame, and r_m is the distance of closest approach.

4.1 Buffer gas collisions

Before discussing how buffer gas collisions are integrated into the overall simulation, let's look at the kinematics of a single collision. Given an ion and a neutral collision partner, the goal is to find the state of the ion after the collision. Assuming that collisions are elastic and that the partners are initially far apart, the total energy of the system is

$$\frac{1}{2}(m_i v_i^2 + m_n v_n^2) = \frac{1}{2}\left((m_i + m_n)v_{cm}^2 + \mu v_r^2\right) = E_{cm} + E, \tag{4.1}$$

where $\vec{v}$ is a velocity in the reference frame of the simulation; subscripts i, n, r, and cm correspond to ion, neutral, relative, and center of mass values; and $\mu = m_i m_n/(m_i + m_n)$ is the reduced mass. We can break the total energy into two parts; E_{cm} is the energy associated with the motion of the center of mass of the system and E is the kinetic energy available for a collision in a center of momentum reference frame. We can write down these energy relations immediately but there is a choice to make about how the kinetic energy should evolve during a collision. For instance, one could implement a hard-sphere model or acknowledge that ions actually polarize neighboring atoms and "collide" when the particles approach closely enough to generate mutual repulsion. This is a choice between definitions of the interaction potential particles feel during collision; either the potential energy between particles is zero everywhere until they hit an infinite wall when they touch, or there's some central, long range electric potential between collision partners. The scattering angle (derivation in [11]) is,

$$\theta_{cm}(b, E) = \pi - 2b\int_{r_m}^{\infty} \frac{dr}{r^2\sqrt{1 - \frac{V(r)}{E} - \frac{b^2}{r^2}}}, \tag{4.2}$$

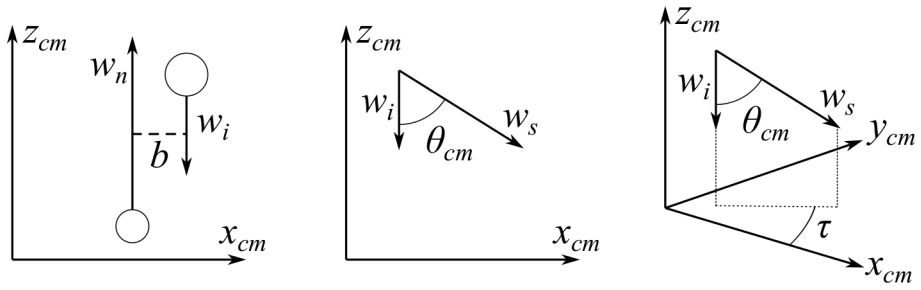

Figure 4.2: Left: the center of momentum coordinate system is chosen so that the x-z plane contains the particle velocities. Center: the initial ion velocity is the z projection of the scattered ion velocity. Right: the scattered ion velocity is defined by the scattering angle (equation 4.2) and a random transverse angle τ.

where $V(r)$ is the ion-neutral interaction potential (see equations 4.12 and 4.13 below), r is the distance between collision partners, r_m is their distance of closest approach, and b is the impact parameter. The impact parameter is the perpendicular distance between the initial velocity vectors of the collision partners (see figure 4.1) – it's a measure of the total angular momentum in the collision. For a given interaction potential and collision energy, r_m is the largest real root of the equation

$$1 - \frac{b^2}{r_m^2} - \frac{V(r_m)}{E} = 0. \tag{4.3}$$

In the current work r_m is found numerically for each collision using root finding algorithms defined in [45].

It's easiest to define the center of momentum scattering angle after choosing a coordinate system. Let's define a center of momentum frame such that the velocities are in the x_{cm}-z_{cm} plane (which is acceptable regardless of the velocities' orientations in the simulation frame). Call this center of momentum reference frame w. The scattering angle in this frame defines the z_{cm} projection between the initial and scattered ion velocities (see figure 4.2). The kinematics are cylindrically symmetric, so once the magnitude of the scattered velocity has been set by the scattering angle in the x_{cm}-z_{cm} plane we then set a random transverse angle $\tau = \mathcal{U}(0, 2\pi)$, where $\mathcal{U}(0, 2\pi)$ indicates a uniformly distributed random number on the interval $(0, 2\pi)$. τ defines the angle of the scattered velocity with respect to the x_{cm} axis. Given these angles, the scattered velocity vector in this center of momentum frame is

$$\vec{w}_s = w_i \begin{pmatrix} \sin(\theta_{cm})\cos(\tau) \\ \sin(\theta_{cm})\sin(\tau) \\ \cos(\theta_{cm}) \end{pmatrix} \tag{4.4}$$

After calculating $\vec{w}_s$ we have to transform back into the reference frame of the simulation. The first step is to rotate to a center of momentum coordinate system which is parallel to

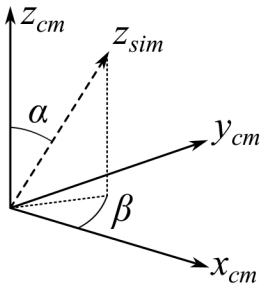

Figure 4.3: Rotation angles between the reference frame of figure 4.1 and the simulation axes.

the simulation coordinates. Call this parallel center of momentum frame u. The initial ion velocity in that frame, $\vec{u}_i$, is just defined by a boost from the simulation reference frame into the center of momentum: $\vec{u}_i = \vec{v}_i - \vec{v}_{cm}$. The rotation angles between the center of momentum frames w and u are then

$$\alpha = \cos^{-1}\left(\frac{u_x}{u}\right), \quad \beta = \tan^{-1}\left(\frac{u_y}{u_x}\right), \tag{4.5}$$

and the rotation matrix from reference frame w into frame u is

$$\mathcal{R} = \begin{bmatrix} \cos(\alpha)\cos(\beta) & -\sin(\beta) & \sin(\alpha)\cos(\beta) \\ \cos(\alpha)\sin(\beta) & \cos(\alpha) & \sin(\alpha)\sin(\beta) \\ -\sin(\alpha) & 0 & \cos(\alpha) \end{bmatrix}. \tag{4.6}$$

Bringing this together we can define the scattered ion velocity in the reference frame of the simulation:

$$\vec{v}_s = \mathcal{R}\vec{w}_s + \vec{v}_{cm} \tag{4.7}$$

This takes care of the collision kinematics given the particle velocities. The ion velocity can be read out at any time (the purpose of the simulation is, more or less, to generate ion velocity vectors), however there's no way to keep track of all neutral collision partners during the simulation. We need a procedure to generate neutral velocities on the fly.

If the neutral atoms form an ideal gas, then the speed of all collision partners should be Maxwell-Boltzmann distributed. This constrains the magnitude of the total neutral velocity vector, but that isn't good enough for the collision kinematics; what's required is three orthogonal velocity components whose *sum* is Maxwell-Boltzmann distributed. Thankfully we can get exactly that by generating three Gaussian distributed random numbers and defining each neutral velocity component $\vec{v}_{nj}$ like this:

$$\vec{v}_{nj} = \mathcal{N}(0,1)\sqrt{\frac{k_b T}{m_n}}\,\vec{j}, \;\; j \in \{x, y, z\}, \tag{4.8}$$

where $\mathcal{N}(0,1)$ indicates a normally distributed random number with mean 0 and variance 1, k_b is the Boltzmann constant, T is the buffer gas temperature, and m_n is the mass of the neutral particle. Equation 4.8 might appear to be an arbitrary choice for the velocity components. One can prove that this choice actually leads to a Maxwell-Boltzmann speed distribution as follows.

Given equation 4.8, the normalized probability distribution for a single neutral velocity component (the probability for the component to take magnitudes between v_j and $v_j + \mathrm{d}v_j$) is

$$p(v_j)\,\mathrm{d}v_j = \sqrt{\frac{m_n}{2\pi k_b T}} e^{-v_j^2 m_n/2k_bT}\,\mathrm{d}v_j = \frac{1}{\eta} e^{-(v_j/v_{th})^2}\,\mathrm{d}v_j, \tag{4.9}$$

where the last step introduces the thermal speed $v_{th} = \sqrt{2k_bT/m_n}$ and a normalization constant $\eta = v_{th}\sqrt{\pi}$. Since selecting the velocity components constitutes three mutually exclusive random events, the probability for choosing a vector in the range $(\vec{v}, \vec{v} + \mathrm{d}\vec{v})$ is just the product of the probabilities for choosing each component:

$$\begin{aligned} p(\vec{v})\,\mathrm{d}\vec{v} &= p(v_x)p(v_y)p(v_z)\,\mathrm{d}v_x\,\mathrm{d}v_y\,\mathrm{d}v_z \\ &= \eta^{-3}\, e^{-(v_x^2+v_y^2+v_z^2)/v_{th}^2}\,\mathrm{d}v_x\,\mathrm{d}v_y\,\mathrm{d}v_z \\ &= \eta^{-3}\, e^{-(v/v_{th})^2}\,\mathrm{d}v_x\,\mathrm{d}v_y\,\mathrm{d}v_z. \end{aligned} \tag{4.10}$$

This is the distribution of the neutral velocity *vector*. To get the distribution of the speed, it's easiest to convert to spherical coordinates and integrate the angular components:

$$\begin{aligned} p(\vec{v})\,\mathrm{d}\vec{v} &= \eta^{-3}\, e^{-(v/v_{th})^2} v^2 \sin(\phi)\;\mathrm{d}v\,\mathrm{d}\theta\,\mathrm{d}\phi \\ p(v)\,\mathrm{d}v &= \eta^{-3}\, e^{-(v/v_{th})^2} v^2 dv \int_0^{2\pi} \mathrm{d}\theta \int_0^{\pi} \sin(\phi)\,\mathrm{d}\phi \\ p(v)\,\mathrm{d}v &= 4\pi \left(\frac{m_n}{2\pi k_b T}\right)^{-3/2} v^2 e^{-(v/v_{th})^2} \mathrm{d}v. \end{aligned} \tag{4.11}$$

Equation 4.11 is the Maxwell-Boltzmann speed distribution in three dimensions, so this proves that equation 4.8 is a valid choice for the velocity components of an atom in an ideal gas[1]. We now have *almost* all the pieces required to do the kinematics for an ion-neutral collision; we can read out the ion velocity in simulation and then use equation 4.8 to generate a neutral velocity, but one has to know the impact parameter before calculating a scattering angle.

In principle the impact parameter for an ion-neutral collision is infinite. This is because the interaction potential is electromagnetic, and the electromagnetic force has infinite range. Accounting for ion-neutral interactions throughout a simulation volume at every time

[1]Of course we proved something else along the way – to get an isotropic normally distributed vector, you generate normally distributed component vectors with the same variance as the total vector.

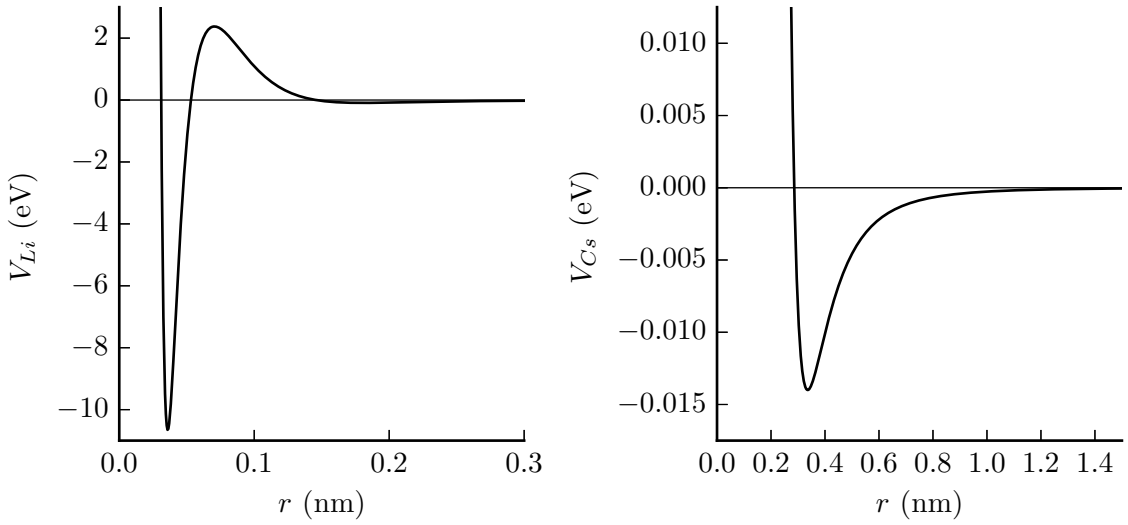

Figure 4.4: Left: Interaction potential between Li^+ and He (Equation 4.13), reported in [50]. Right: Cs^+-He interaction potential (Equation 4.12), reported in [41].

step would take significant computational resources and, since the scattering angle falls off quickly with distance between collision partners, most of those resources would go to calculations that don't affect the ion trajectory very much. It's better to define some maximum interaction range beyond which ions can't see neutrals any more, which is equivalent to choosing a minimum scattering angle; finding the maximum impact parameter B means finding the largest root of the equation $|\theta_{cm}(b, E)| - |\theta_{min}| = 0$ for a given collision energy E. We could solve this equation for each collision, however root finding and integration are computationally intensive; in this case we have to find another root to get r_m and then integrate $\theta_{cm}(b, E)$ at every step in the search for θ_{min}, which would significantly increase the overall simulation time. It's better to define some function $B(E)$ which will allow us to approximate B at all collision energies.

Since the scattering angle depends on the interaction potential, we'll need to select a potential in order to make a choice about the minimum scattering angle. Simulations presented here deal with interactions of singly charged Cesium and Lithium ions with Helium buffer gas. The Cs-He potential is relevant because Cesium is a standard calibrant ion in mass spectrometry, and Li-He is used as a check against previous work in [50]. Experimental ion mobilities are also available for both interactions (see section 4.3), so output from the buffer gas code may be compared to two different data sets. The interaction potentials are[2]

[2]The Cs and Li potentials are reported in [41] and [50] respectively.

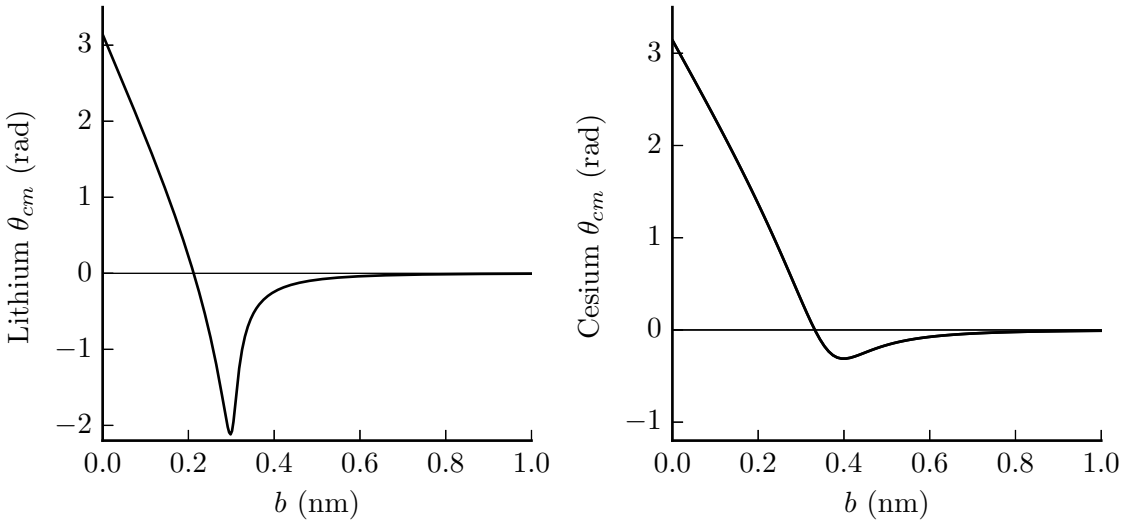

Figure 4.5: Center of momentum scattering angles for Lithium and Cesium ions scattering on Helium atoms. θ_{cm} is always negative for large b, and the maximum scattering angle at high b decreases with collision energy E.

$$V_{Cs}(r) = 0.0109\left(\frac{0.000346}{r^8} - \frac{0.00242}{r^6} - \frac{0.0222}{r^4}\right), \tag{4.12}$$

$$V_{Li}(r) = 27.2\Bigg(23.2\,e^{-43.8r} - 29.3\,e^{-59.5r} + \frac{8.74{\cdot}10^{-9}e^{-32.9r}}{r^6} - \frac{5.98{\cdot}10^{-6}e^{-0.116r}}{r^4} + \frac{0.0529\big(23.0\,e^{-62.5r} - 6.44\,e^{-32.0r}\big)}{r}\Bigg), \tag{4.13}$$

where the potential comes out in eV for r in nm (see figure 4.4). From figure 4.5 it's clear that both interaction potentials lead to an extreme value in θ_{cm} which approaches zero as the collision energy increases. This places a constraint on the energy region in which the function $B(E)$ will be continuous. In practice one should determine $B(E)$ over a region in which it's continuous and take the result as an approximation for all energies. An additional constraint on the choice of θ_{min} comes from calculating the ratio of the scattered ion kinetic energy to the ion kinetic energy before collision. From equation 4.4 we have

$$\frac{E_s}{E_i} = \frac{w_s^2}{w_i^2} = \sin^2(\theta_{cm}) + 1. \tag{4.14}$$

We'd like the energy ratio to be close to 1 at θ_{min} to ensure that we aren't ignoring collisions which are relevant to ion motion in the simulation. For $\theta_{min} = 10^{-3}$ rad, equation 4.14 differs from unity by about one part per million. Therefore, the criteria for choosing the minimum scattering angle in this work were that θ_{min} should be no larger than 1 mrad and

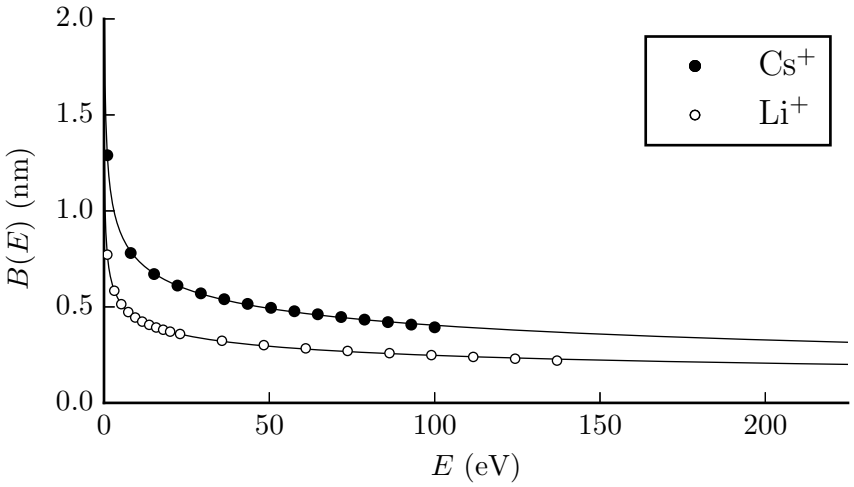

Figure 4.6: Maximum impact parameter vs. collision energy for Cesium and Lithium ions scattering on Helium atoms.

that $|\theta_{min}|$ must intersect $\theta_{cm}(b, E)$ up to collision energies of at least 100 eV[3]. The angles meeting these criteria are 1 mrad for Lithium and 0.22 mrad for Cesium; the maximum collision energies producing an intersection are then 137 eV and 100 eV respectively. To generate $B(E)$, one can follow the prescription in [50]: define some set of collision energies $\{E_j\}$, solve $\theta_{cm}(b, E) - \theta_{min} = 0$ in b for each E_j, and then do a least-squares fit to determine constants in the equation

$$B(E) = \frac{c_1}{E^{c_2}} - c_3. \tag{4.15}$$

$B(E)$ for Lithium and Cesium is plotted in figure 4.6, and the functions are

$$B_{Cs}(E) = \frac{1.48456}{E^{0.196523}} - 0.196341 \tag{4.16}$$

$$B_{Li}(E) = \frac{0.793133}{E^{0.233996}} - 0.0228196, \tag{4.17}$$

where B comes out in nm for E in eV. Python code to generate these functions is provided in section A.1.

$B(E)$ defines the maximum value of the impact parameter at a given energy, so at each collision we need to generate a random b between 0 and $B(E)$. The impact parameter is not a simple uniform random variable; the correct definition is $b = B\sqrt{\mathcal{U}(0,1)}$ (see next section for details). The impact parameter was the last parameter required to run the kinematics for a collision; given an ion velocity and a random neutral velocity we can now get the

[3]The energy constraint means that the collision cross section is artificially low for collision energies above 100 eV.

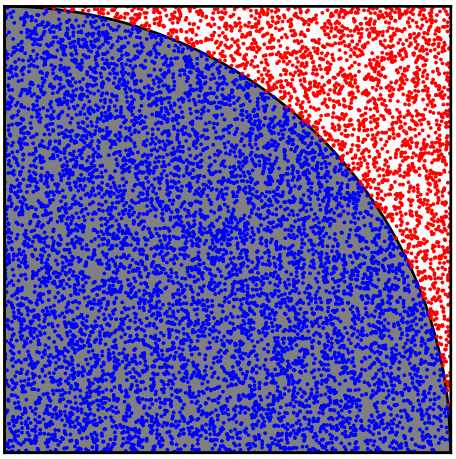

Figure 4.7: Visualization of a Monte Carlo approximation of π. Pairs of uniform random numbers (a, b) define points on the plane; points for which $a^2 + b^2 < 1$ are shown in blue.

collision energy, generate an impact parameter, then calculate the scattering angle and the scattered ion velocity. This completely defines a single ion-neutral collision, but before we can simulate ion motion in buffer gas we have to decide when a collision should actually occur. Since the collisions are random events with a predictable average rate, a Monte Carlo method is an appropriate decision model.

4.2 The Monte Carlo algorithm

The Monte Carlo technique is a method for integrating functions using random numbers. A common example of the use of Monte Carlo algorithms is to approximate π by finding the area under the curve $a^2 + b^2$ [39, ch 6]. The procedure is as follows: generate a large set of pairs of random numbers $a_j = \mathcal{U}(0, 1)$, $b_j = \mathcal{U}(0, 1)$ and calculate the sum of squares for each pair, $s_j = a_j^2 + b_j^2$. The fraction of values $s_j < 1$ then approaches $\pi/4$ as the number of pairs increases. Figure 4.7 shows a plot of 10^4 random pairs, 7864 of which fall under the curve. The approximation to π is therefore $4 \cdot 7854/10^4 = 3.1376$. Monte Carlo integration methods have several advantages [39], but two are relevant here. First, for n random numbers used to sample a function, the error on the integral is always $1/\sqrt{n}$ regardless of the number of dimensions the function is to be integrated over. Second, as long as the function can be evaluated for a given set of random parameters, we don't have to define the region over which the integral should be evaluated. These features are relevant for simulations of buffer gas collisions because the probability of an ion-neutral collision is a multidimensional function that has to be integrated in order to decide if an ion should collide with a neutral atom.

To estimate the probability of an ion-neutral collision, one can start from dimensional analysis. The probability has to increase with the neutral gas density N; it also has to

increase over time, and the only relevant parameter which depends on the simulation time is the ion velocity. The probability, being dimensionless, then has the form $N\sigma v_i \mathrm{d}t$, where $\mathrm{d}t$ is some small time step and σ is the collision cross section. Since B is defined as the maximum distance between collision partners, the total cross section should be πB^2. The probability is time independent because the infinitesimal time step $\mathrm{d}t$ is a constant value; this implies that the times between collisions follow a Poisson distribution [39, section 3.2], and so the cumulative probability for a collision should be

$$F(t) = 1 - e^{-N\pi B^2 v_i t} \approx N\pi B^2 v_i \, t, \tag{4.18}$$

where the approximation is valid for small t. If the simulation time step is kept well below the average time between collisions, then the collision rate R is roughly

$$R = N\pi B^2 v_i. \tag{4.19}$$

At every time step we say an ion saw a collision if $R\mathrm{d}t$ is greater than a random number $\mathcal{U}(0,1)$. That is, we approximate the integral of F by evaluating the function based on the simulation state at successive times and comparing the result to a random number in the range of F; this is a Monte Carlo approximation.

There are a couple of things to note at this point. First, t in equation 4.18 doesn't have a fixed starting point. If all parameters in the equation were fixed and we only counted time then t would refer to the time since the last collision, but in this case $B(E)$ and v_i both depend on the simulation state so there are multiple time-varying parameters. Since those parameters are different at every time step, we can effectively treat each time step as an independent Poisson counting experiment. This means that in the Monte Carlo integration we can always multiply the current collision rate by the length of the previous time step without keeping track of the time since any particular event.

The second important result of this Monte Carlo decision is that after the Monte Carlo algorithm says there's been a collision, any random variables sampled from parameters in equation 4.18 have to be chosen by analytic inversion [45, section 7.3.2]. This is because we're using uniform random numbers to integrate F, so if we want to randomly sample b with maximum value B then we can't just use any random number; the random variate must be chosen such that if we substituted b for B in equation 4.18 then F would be uniformly distributed[4]. This is important because if $R\mathrm{d}t > \mathcal{U}(0,1)$ in the Monte Carlo test then we have to do kinematics for a collision and choose a random impact parameter b on the interval $(0, B)$. $b = B\mathcal{U}(0,1)$ would oversample small values because $F(t) \propto B^2$.

[4]Put another way, there's a probability distribution $p(t)$ for which $F(t)$ is the cumulative probability, and any random variables in the system should be sampled from $p(t)$.

The correct distribution for b is found by inverting $F(B)$ and taking $F^{-1}(\mathcal{U}(0,1))$, so for a particular collision we have

$$b = B(E)\sqrt{\mathcal{U}(0,1)}. \tag{4.20}$$

A flowchart of the buffer gas simulation is shown in figure 4.8. The collision kinematics and Monte Carlo decision described in the last two sections are implemented in SIMION using code I've written for the current work and based on previous SIMION extensions for simulations presented in [50]. Details of the code and its interface with SIMION can be found in appendix A.

4.3 Evaluation of buffer gas code

The buffer gas simulation code was tested by comparison to ion mobility data for Cesium and Lithium ions in Helium gas, published in [21] and [56] respectively. The ion mobility is the ratio between an ion's drift velocity through a gas and an applied electric field $\mathcal{E}$. Mobilities are typically reported in terms of the *reduced* mobility K_0. The reduced mobility is scaled such that it eliminates dependence on the thermodynamic conditions of the gas:

$$K_0 = \frac{v_d}{\mathcal{E}}\left(\frac{273.15\,[\mathrm{K}]}{T}\right)\left(\frac{P}{101325\,[\mathrm{Pa}]}\right) = \frac{v_d}{\mathcal{E}}\frac{N}{N_0}, \tag{4.21}$$

where T is the buffer gas temperature in degrees K and P is the pressure in Pa. The standard gas density N_0 is $2.6868{\cdot}10^{25}$ m^3. It is also conventional to report ion mobilities as a function of $\mathcal{E}/N$ in Townsend, which is a unit defined such that

$$1\,[\mathrm{Td}] = 10^{-21}\,[\mathrm{Vm}^2]. \tag{4.22}$$

Simulations of Cs^+ and Li^+ ion mobilities in Helium were carried out in SIMION using a cylindrical volume 100 grid units long by 100 grid units in diameter. The drift length L between electrodes was 96 grid units, and the grid was set to 1 mm per grid unit. In order to simulate mobilities in Townsend, the gas pressure was always 1 mbar (100 Pa), the temperature was 300 K, and the potential difference across the electrodes was calculated from

$$V = -10^{-21}\left(\frac{\mathcal{E}}{N}\right)\frac{PL}{k_bT} = -10^{-21}\left(\frac{\mathcal{E}}{N}\right)\frac{0.032}{k_b}, \tag{4.23}$$

where $\mathcal{E}/N$ was input in Townsend. The experimental mobilities for Lithium were actually determined at 296 K, but it's clear from figure 4.9 that the model isn't sensitive enough for the difference to matter.

Experimental data used to validate the collision model cover 5–120 Td for Cesium and 3–180 Td for Lithium. Trapped ions in the MR-ToF can see fields well below 1 Td because

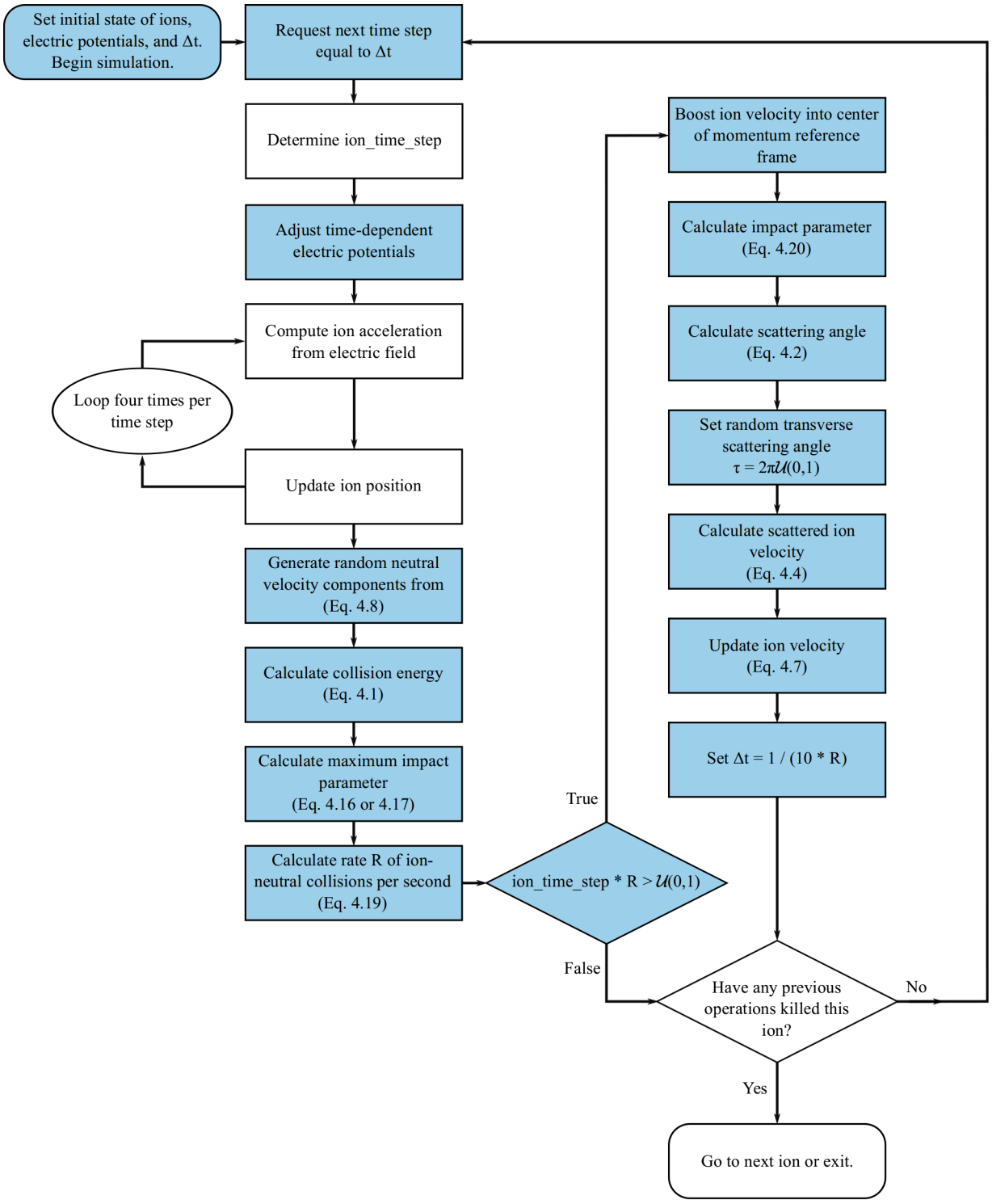

Figure 4.8: Flowchart of buffer gas simulations. White nodes are native SIMION operations, blue nodes indicate operations which include code written for this project. See appendix A for details.

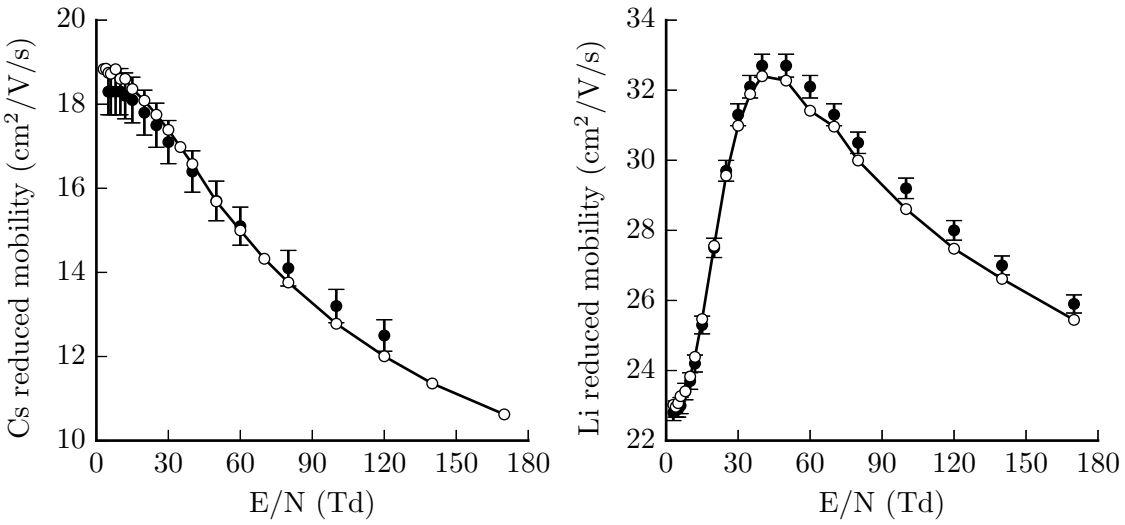

Figure 4.9: Comparison between experimental and simulated ion mobilities for Cesium and Lithium ions in Helium buffer gas. Filled circles are experimental values with published errors (3% for Cs and 1% for Li). Open circles are simulated mobilities averaged over 1000 ions per point.

they're near the minimum of an approximately harmonic potential, and the extraction field applied to kick ions into the mass analyzer is in excess of 10^6 Td (700 V applied over 7 mm in a buffer gas pressure of 10^{-3} mbar). A single collision model can't accurately cover such a wide energy range, however ions only see very high fields for tens of nanoseconds during extraction from the analyzer trap. As a benchmark value, an ion moving around the MR-ToF transport section typically sees fields of approximately 1 V/cm, and with a buffer gas pressure of 0.01 mbar at 300 K that field is roughly 400 Townsend. While the experimental data doesn't reach 400 Td, mobilities simulated using this model agree with measured values throughout most of the data range and this is sufficient for the current work. Note that up to a point there is a trade off between accuracy and simulation time – the time step in these simulations was set to about one tenth of the time between collisions ($1/R$), and simulated mobilities for Cesium are in slightly better agreement with data when the time step is ten times smaller. The shorter time step also increases the simulation time for low-field points in figure 4.9 from hours to days on a workstation with a 3 GHz Intel Core i7 CPU.

Following [46], it is also worthwhile to confirm that a simulated thermal ion population actually has a thermal velocity distribution. Figure 4.10 shows normalized histograms of thermal ion speeds plotted against a Maxwell-Boltzmann distribution (equation 4.11). The collision model presented here does produce Maxwell-Boltzmann distributed ion velocities for an initially thermal ion population. The speeds in figure 4.10 were produced by simulating ion drift through buffer gas at 1 mbar and 300 K in a 22 mm cubic volume (1 grid

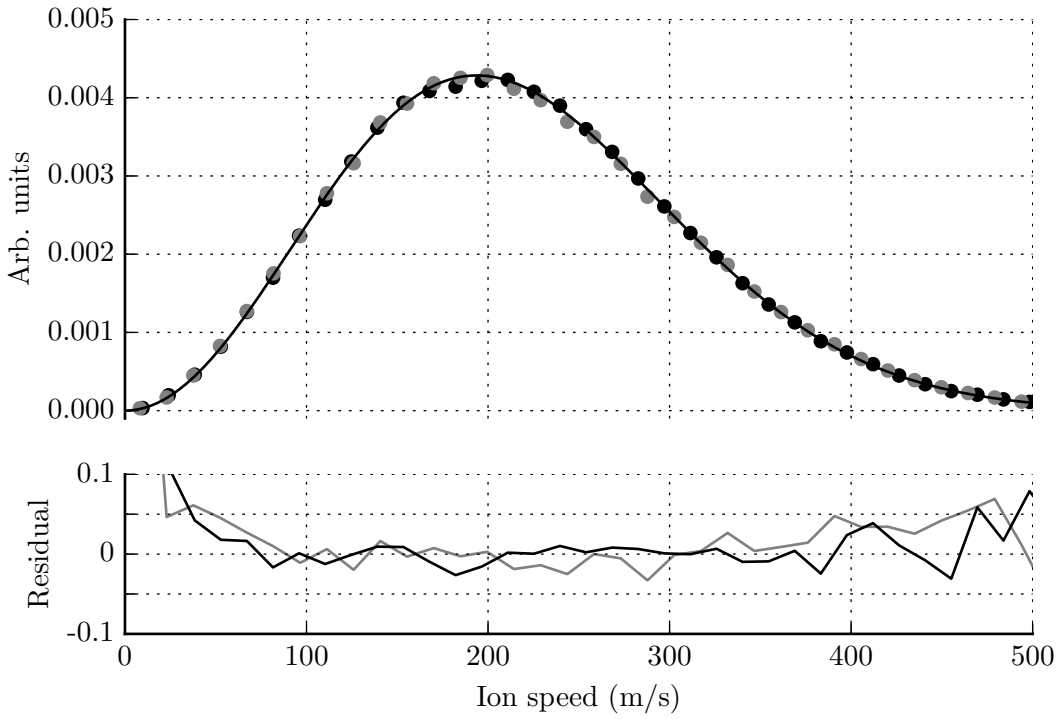

Figure 4.10: Histograms of simulated Cs^+ ion speeds in a grounded box filled with He buffer gas. Black circles are ions initialized with Maxwell-Boltzmann distributed velocities, grey circles are ions initialized with a constant 0.07 eV kinetic energy. The black line in the upper plot is a Maxwell-Boltzmann speed distribution for Cesium atoms at 300 K. Lines in the lower plot show the relative deviation of simulated data from the ideal distribution.

unit per mm) surrounded by a grounded surface. Ion speeds were recorded every 1000 time steps until there were $2.5 \cdot 10^5$ speeds to histogram.

4.4 Input optics and the cube

Simulations of the input optics upstream of the MR-ToF gas encapsulation are available, however during commissioning the ion population coming into the MR-ToF was essentially unknown. The minimum incoming kinetic energy is set by the electric potential difference between the external ion source and the input RFQ but there are no detectors outside the gas encapsulation which could inform efficiency estimates or determine the initial phase space of ions in the transport system. For this reason, and because thermal sources were intense enough to get ions into the system without much tuning, optics at high vacuum in front of the input RFQ were ignored in the current work. Buffer gas temperature throughout these simulations is 300 K.

General features of the input RFQ were estimated using 10 Cesium ions starting from the upstream RFQ contacts (10 mm into the buffer gas region) with an initial kinetic energy

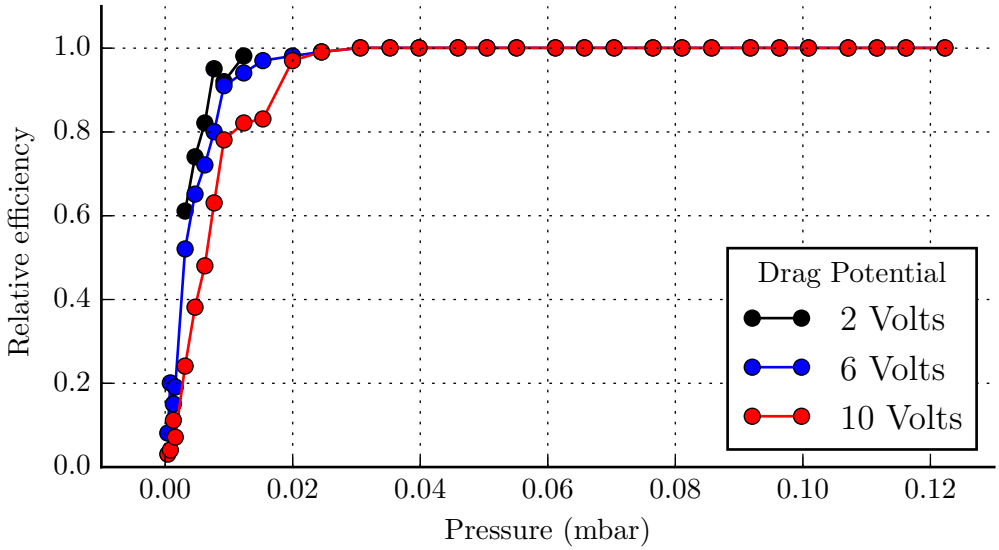

Figure 4.11: Simulated relative efficiencies for ion transport around a corner in the cube.

of 10 eV. Ions were initialized randomly within a circle 2 mm in diameter centered on the z axis with no divergence. Ion-ion interactions were approximated using SIMION's charge repulsion feature with the ions' charge weighting factor set to 1. With the gas pressure at $3.5 \cdot 10^{-2}$ mbar, ions took 600 µs to settle into an ion cloud with a standard deviation in z smaller than 2 mm and centered 127 mm from the second input aperture (this is 15.5 mm from the cube aperture; see section 3.2). Since ions in the real setup will cool in the input RFQ for several milliseconds while the previous ion bunch runs through the system, simulations of ion transport downstream from the input were initialized with ions at 127 mm from the first input aperture. Initial ion velocities were then determined a 3D Maxwell-Boltzmann speed distribution for Cesium atoms at 300 K.

In pass-through mode the cube acts approximately like a linear RFQ, and the simulated transport efficiency in the MR-ToF RFQs is 100% for q values close to stability (see section 2.1). Ions are never stored in the cube, and cooled ions typically pass through into the transfer RFQ within tens of µs. Transporting ions around a corner through the cube is a more complicated operation, and I've produced detailed simulations to estimate its efficiency. Unfortunately there wasn't time to produce a data set for comparison to these simulations, but the results of the simulations are presented here for future reference.

Figures 4.11 – 4.13 show data representing simulated ion transport around a corner in the cube. Simulations indicate that 100% transport efficiency is possible with a He pressure in the 10^{-2} mbar range. The efficiency is not sensitive to the applied field gradient; cube gradients of 2–10 V all produce 100% efficiency above about 10^{-2} mbar. Transport times increase significantly with cube gradients below 5 V and times are 20–30% shorter at 10 V

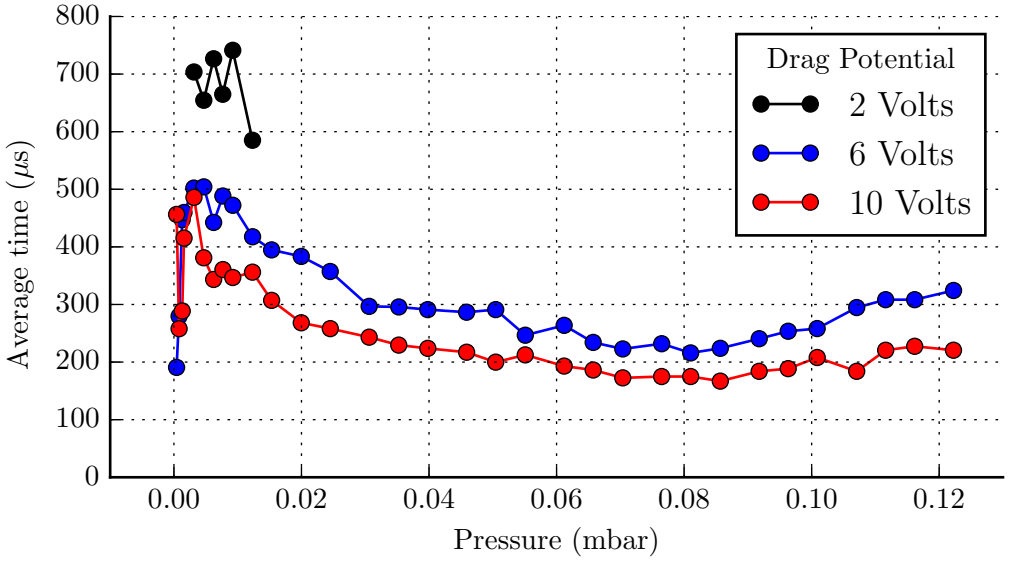

Figure 4.12: Simulated average time required for ions to enter the cube and reach the channeltron detector around a corner from the input.

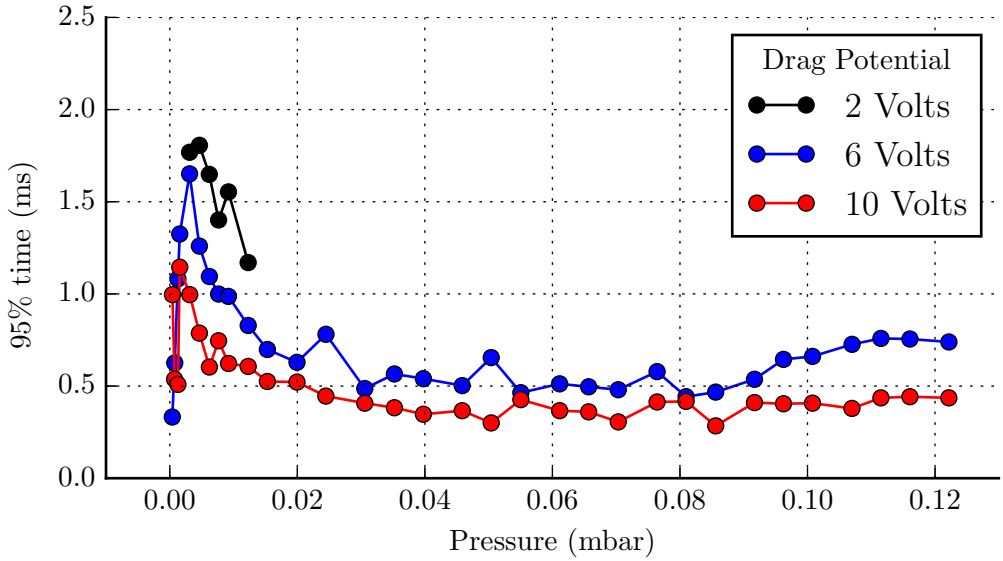

Figure 4.13: Simulated time required for 95% of ions to enter the cube and reach the channeltron detector around a corner from the input.

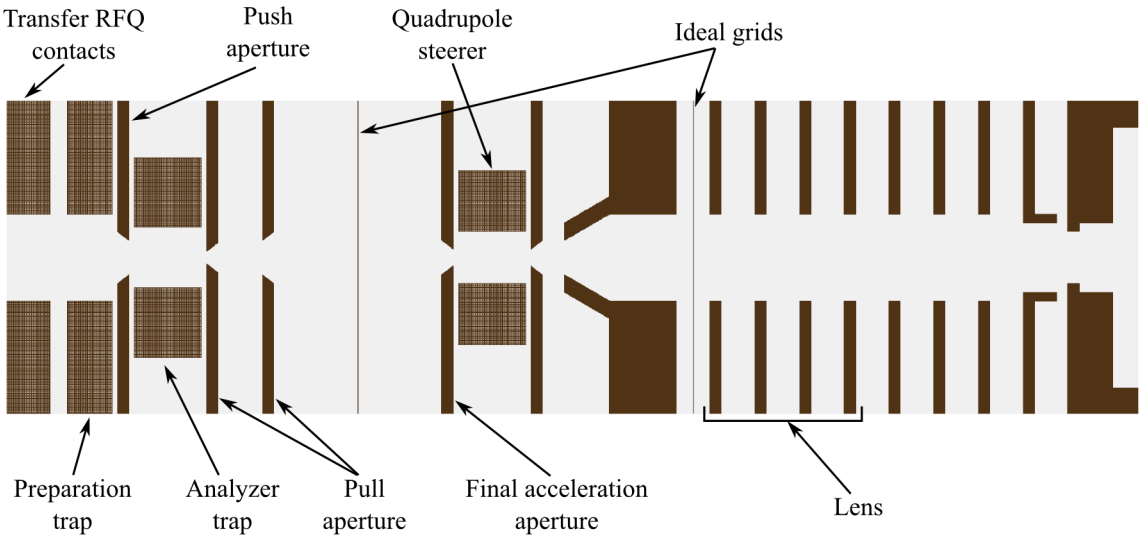

Figure 4.14: Cross section of simulated trap geometry (image not to scale). Unmarked elements are grounded. All three potential arrays extend to the left hand side of the imege and they're layered with the trap on top, the steerer in the middle, and the analyzer at the bottom. Ions flying through a particular region only see the potential from the uppermost array in that region. The trap array ends at the first ideal grid and the steerer array ends at the second. Ideal grids are planes perpendicular to the diagram which set a constant electric potential but do not stop ions. They're used to set the electric potential at the edge of a potential array so that it approximately matches the potential on the other side of the boundary.

compared to 6V. Unfortunately there was not time for a detailed comparison between these simulations and actual performance during this work.

4.5 The mass analyzer

Simulations of the mass analyzer use a cylindrically symmetric geometry everywhere outside the traps, the steerer, and the mass range selecter (MRS). SIMION can fly ions through symmetrical geometries without storing additional field values for symmetrical points, so this method has the significant advantage that the resolution in the ion mirrors can be as high as 40 grid units per millimeter while the total simulation occupies less than 2 gigabytes of memory. The trap, steerer, and MRS are defined with no symmetry operations. The resolution from the trap up to the beginning of the lens in front of the analyzer is 8 grid units per millimeter, and the resolution in the center of the drift region around and including the MRS is 4 grid units per millimeter.

The trap geometry includes the downstream transfer RFQ contacts as well as the preparation trap segment, so the full 4 ms of cooling in the traps may be included in a simulation run through the mass analyzer. Switched voltages in the traps are implemented with an

Electrode	Closed	Load	Kick
RFQ contacts	1311	1311	1311
Preparation trap	1301	1301	1301
Push aperture	1318	1290	1667
Analyzer trap	1300	1300	1300
Pull aperture	1318	1318	933
Steering aperture	-1200	-1200	-1200
Lens	-3263	-3262	-3263

Table 4.1: Typical simulation voltages for optical elements upstream of the mass analyzer. Peak-to-Peak RF voltages are 260 V for the preparation trap and 240 V for the analyzer trap.

error function to account for finite switching times. Instantaneous switching of simulated mirror voltages is acceptable because ions take microseconds to return to a mirror field and real switching times are hundreds of nanoseconds, so real ions should only see static fields at the mirrors. For simulations in this work, electrodes in the trap region have three possible states; "closed" refers to cooling in either trap, "load" refers to values when ions are loaded into the analyzer trap from the preparation trap, and "kick" refers to voltages used to kick ions into the analyzer. The apertures around the analyzer trap are the only switched voltages in these three configurations (see table 4.1). Electrodes in the analyzer also have three states; "open" voltages allow ions to pass through a mirror, "TFS" (time focus shift, see section 2.5) voltages are used to move the time focus of an ion bunch from the analyzer trap to the detector, and "closed" or "multi-turn" values trap ions in the analyzer for any number of turns after the TFS reflections. Typical simulated analyzer voltages are listed in table 4.2.

For ions randomly initialized in a small spherical volume (less than 1 mm in diameter) at the potential minimum of the analyzer trap with Maxwell-Boltzmann distributed velocities, roughly 100% transport efficiency to the detector is achieved with no cooling under a variety of trap parameters. These ideal simulations usually include 10 ions and use SIMION's charge weighted repulsion setting to account for ion-ion interactions. The standard deviation of arrival times at the detector after 2 turns (1 TFS, 1 multi-turn) is typically $3-4$ ns, corresponding to a full width half max of $7-9.5$ ns for a Gaussian peak. Peak widths in the real system compare well with these results (see section 5.3). The buffer gas pressure in the traps is set to $2 \cdot 10^{-3}$ mbar and the analyzer pressure is 10^{-7} mbar in these simulations. For a 10 ion bunch there are typically less than 5 buffer gas collisions in the trapping region during ejection and zero collisions outside the trap even for hundreds of turns in the analyzer. Perfect efficiency for such long flight times is unrealistic, and the relative transport efficiency in the real system clearly decreases with number of turns (see section 5.5).

There are two sources for this error. First, the simulation uses the same collision model for all ion-neutral interactions, which assumes that all residual gas in the analyzer is Helium.

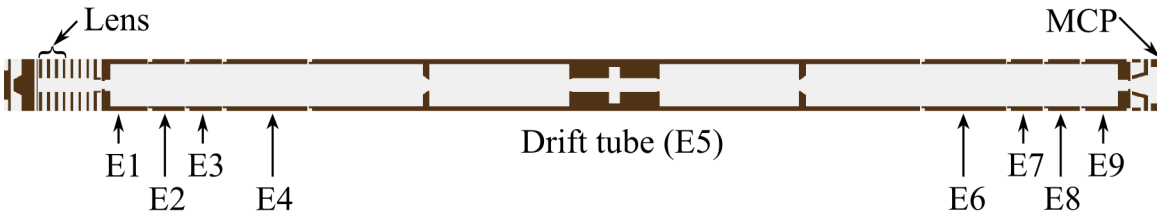

Figure 4.15: Cross section of simulated analyzer geometry (image not to scale). Unmarked elements are groundend.

Electrode	Open	TFS	MT
E1	433	1542	1715
E2	0	1215	1215
E3	826	826	431
E4	-2027	-2027	-3255
E5	0	0	0
E6	-2027	-2027	-3255
E7	826	826	431
E8	0	1215	1215
E9	0	1542	1715

Table 4.2: Typical simulation voltages in the the mass analyzer. E5 is the grounded drift tube; E1 – E4 are electrodes at the upstream end of the analyzer, E6 – E9 make up the downstream end. Only E1 and E9 have three different voltages for the three states.

The base pressure in the analyzer (before introducing buffer gas into the RFQs) is in the mid 10^{-9} to low 10^{-8} mbar range, so in reality there is some significant fraction of other neutral particles which could have much stronger interaction potentials than Helium. Second, ions in the analyzer have kinetic energies above 1 keV and the collision model hasn't been evaluated at such high energies (see section 4.1). Despite the uncertainties, we can infer from these simulations that for short flight times, any loss of ions in the analyzer or the traps is due almost entirely to misalignment of ion optics or imperfect cooling.

Linear misalignment between the traps and the analyzer has been simulated using a transverse offset between the simulated trap geometry and all elements downstream (the steerer, the lens, and the analyzer). The efficiency was roughly proportional to the overlap between the pull aperture at the analyzer trap and the aperture immediately upstream of the steerer, with efficiency dropping to a few percent at a 2 mm displacement between the optic axes. The reduction in efficiency was due entirely to the misalignment between the two apertures; any ions passing through into the analyzer hit the detector after 1 TFS turn and 10 multi-turns. Angular misalignment between the traps and the analyzer was not investigated in this work, but the geometries described here may be quickly adapted for those simulations should they become necessary.

To simulate cooling prior to mass analysis, an estimate of the initial conditions for ions in the preparation trap was made by simulating ion transport through the transfer RFQ. Ions were initialized just after the aperture between the cube and the RFQ in a 2 mm circle with 2 eV kinetic energy and velocities parallel to the optic axis. Buffer gas pressure in the RFQ was set to $2 \cdot 10^{-3}$ mbar. After 900 µs flight time, the average ion energy and the standard deviation of the energy were both around 0.3 eV and the ion cloud was centered on the potential minimum of the preparation trap with a width of a few millimeters. The average energy, the energy spread, and the width of the ion cloud all decreased by about 30% between 900 µs and 1 ms flight time. Given these results, when ions are cooled before mass analysis in the analyzer simulation, they're initialized with thermal velocities and randomly distributed in a cylinder 3 mm long by 1 mm in diameter centered on the preparation trap minimum. Ions are held in the preparation trap for 100 µs and then transferred to the analyzer trap where they're cooled for an additional 3 ms before ejection into the mass analyzer.

While the transfer RFQ simulation gives a best guess for ion conditions in the preparation trap, there is significant uncertainty because in reality the buffer gas conditions are not well constrained in the region around the traps. The nearest pressure sensor is more than 10 centimeters away, and the pull aperture for the analyzer trap, diameter 1.5 mm, is also the smallest differential pumping aperture for the transfer RFQ. Buffer gas is therefore flowing out of the analyzer trap at some high rate, so ions in the traps are more likely to see neutral collision partners moving towards the analyzer. This effect isn't included in the simulation. The push aperture (the one between the preparation trap and the analyzer trap) has a 4 mm diameter, so the pressures in the traps are probably similar but not the same. The buffer gas pressure also drops by more than an order of magnitude between the cube and the traps. The pressure in simulation is $2 \cdot 10^{-3}$ mbar for both the transfer RFQ and the traps, however the 2 eV initial ion energy in the transfer RFQ is chosen to be somewhat lower than the expected energy coming out of the cube in order to compensate for the artificially low simulated pressure near the cube.

Given the voltages in tables 4.1 and 4.2, there is still an available degree of freedom to tune the peak width, which is the amount of time the aperture between the traps is opened so that ions can be loaded into the analyzer trap. The simulated peak width is minimized when the loading time is around 4.9 µs. Optimum loading times in the real system are typically 4–7 µs. For the initial conditions described above, the simulated transport efficiency from the preparation trap to the MCP detector is above 90% even when the time width of a gaussian peak (FWHM) at the detector after 2 turns is more than 50 ns, or about five times the ideal value. In other words, the simulated efficiency is high even when the trap and analyzer potentials are badly tuned. Perfect efficiency is unlikely even in a well-tuned system because ions may collide with neutral atoms in the trap as they are kicked into the analyzer.

Chapter 5

Commissioning the TITAN MR-ToF

After constructing the MR-ToF we commissioned the system off-line. This chapter reports on results obtained with the device operated as an off-line mass spectrometer; the system was not on the TITAN platform during these measurements, and ions were produced with either the diagnostic ion source on the cube or the temporary ion source mounted to the input optics (see figures 3.1– 3.3). Commissioning measurements include ions from thermal ion sources of Cesium and Potassium with natural abundances. All time of flight spectra shown here are averaged oscilloscope traces read out directly from the MCP detector. The oscilloscope used to collect these data was a Lecroy HDO6034 with a bandwidth of 350 MHz and an analog sample rate of 2.5 GS/s. Figure 5.1 shows a series of single ion signals collected on the oscilloscope compared to a 1000 shot average. The MR-ToF was not well-tuned when those signals were recorded so the averaged peak is much broader than typical; the figure is only meant to illustrate "raw" data collected during this work.

5.1 Mass resolving power

The analyzer is designed for ions with a drift kinetic energy of around 1.3 keV but the infrastructure to apply these voltages wasn't initially available (see chapter 3), so development of the TITAN MR-ToF in Vancouver began with a drift energy of 650 eV. That configuration also reduced the kicking field in the trap by a factor of two relative to the design value, which meant the ultimate mass resolving power of the system was limited (see sections 2.6 and 2.7). Diagnostics of the transport system and wiring could still be performed at 650 eV kinetic energy, and the highest mass resolving power we demonstrated at low kinetic energy was around 50,000 (see figure 5.2).

Doubling the kicking field and the drift kinetic energy should roughly double the mass resolving power of the spectrometer, so one of the primary goals of this thesis project was to install a high voltage system capable of floating the power supplies for ion optics in

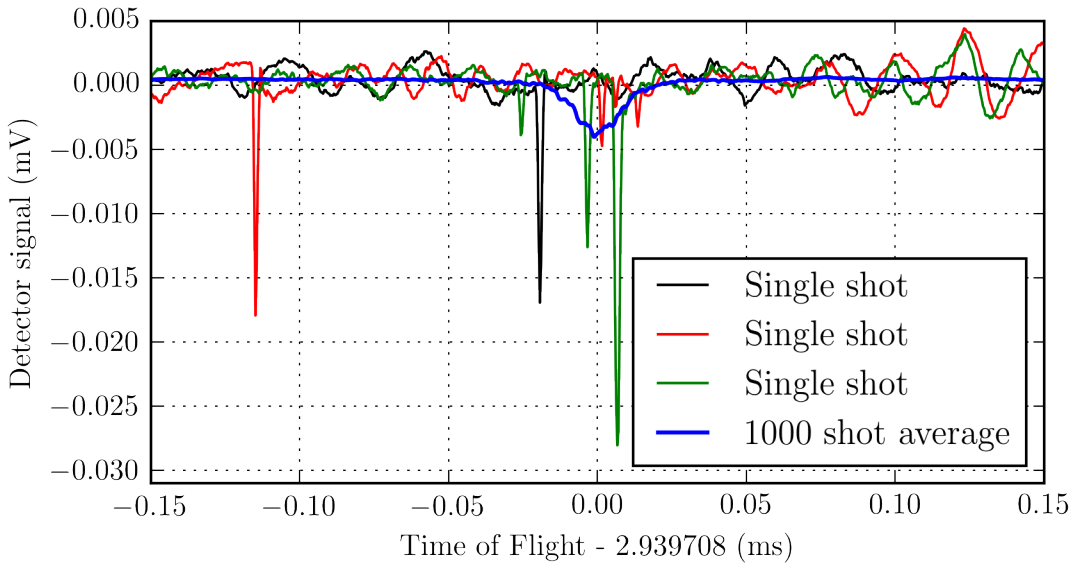

Figure 5.1: Single-shot and averaged oscilloscope signals from the MCP. This is a broad, poorly tuned peak compared to examples below, and peaks below are shown positive-going to simplify the figures.

the transport system to 1.3 kV in order to bring the MR-ToF up to its design voltages. We met this goal, however the overall improvement in the mass resolving power to date is better than a factor of two. In addition to installing the high voltage system, we replaced some components in the stabilizers for the mirror voltages, we tuned the resistance and capacitance of switches on the trap to reduce the switching time between trapping and kicking voltages by a factor of three, and we spent time tuning the voltages in the mass analyzer around their design values in order to find the best operating parameters for the real system. As a result, during my thesis work we were able to improve the ultimate mass resolving power of the TITAN MR-ToF from less than 50,000 to 160,000 (see figure 5.2). This is close to the theoretical resolving power calculated in section 2.7; a comparison is shown in figure 5.3.

It's worth noting that it is possible to switch between high and low resolution by changing a few values in the timing control software. In fact, using control software produced by our collaborators in Germany, we generated the data points shown in figure 5.2 simply by selecting a turn number and recording the position and width of an averaged oscilloscope trace. Similarly, no additional tuning is required to generate high resolution sections of wide band spectra. This flexibility is due to the fact that the mass analysis starts with a TFS operation which moves the time-energy focus of ions in the analyzer onto the detector and then continues with multi-turn reflections which maintain the same focus regardless of the number of turns (see section 2.5).

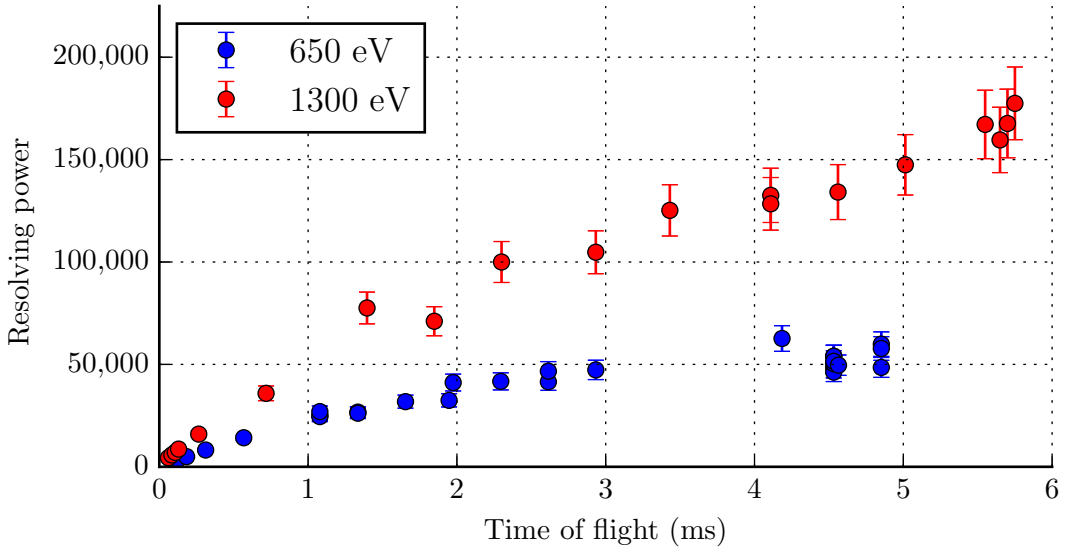

Figure 5.2: Mass resolving power of the TITAN MR-ToF demonstrated with ^{133}Cs ions. 10% error bars are assigned as a conservative estimate of changes due to normal voltage variations. The data collected at 650 eV represent the performance of the mass spectrometer as of fall 2014 and the 1300 eV data represent the current performance of the system. We've improved the mass resolving power by about a factor of three during this project.

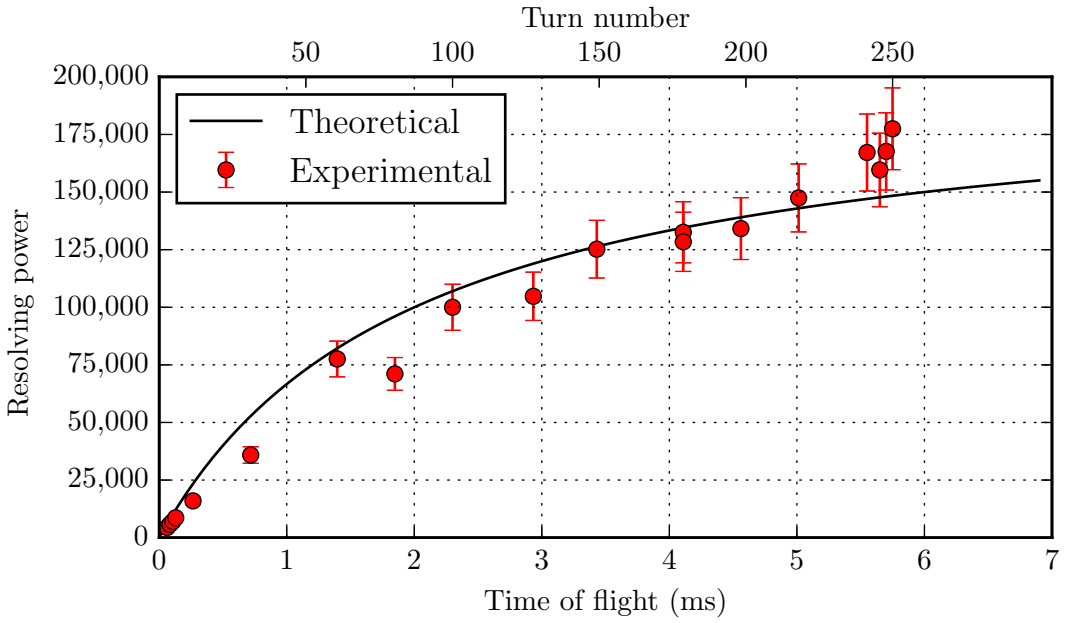

Figure 5.3: Comparison between theoretical mass resolving power calculated for ^{133}Cs (figure 2.16) and experimental results. This figure does not necessarily indicate that the TITAN MR-ToF is better than third order focusing, because the assumptions made in generating the theoretical curve (equation 2.48) were conservative (there is also some uncertainty in estimating the single turn time of flight from figure 2.13).

5.2 Broadband diagnostics

Wide band mass spectra are an important tool for beam diagnostics and for estimating relative intensities between background species and any ions of interest. During online operation for a TITAN mass measurement, "broadband" spectra are typically required over a mass range of about 100 MeV (roughly 0.1 amu) in order to collect data for a single set of isobars. Single spectra covering a greater mass range may be extremely useful in special cases such as possible future development of molecular beams at TRIUMF. In that case, two molecular ions of interest could be separated by tens or hundreds of amu.

Very broad samples covering hundreds of amu can be generated in the TITAN system using hot cathode ion gauges mounted inside the buffer gas encapsulation around the transport system. The buffer gas pressure is typically low enough to operate these gauges, and the hot filaments ionize contaminants present in the buffer gas or on the filaments themselves. Some portion of the contaminant spectrum is captured inside the RFQs and is transported to the analyzer. The mass spectrum from the ion gauges is quite diverse and it has been an excellent commissioning tool when combined with calibrant ions from a thermal source.

Figure 5.4 demonstrates that we can isolate a single mass number in the analyzer using the mass range selector (MRS). As discussed in section 3.4, the MRS is a quadrupole steerer at the center of the analyzer which may be used as a gate to block or pass ions. The switching time required to change the state of the steerer is such that the smallest mass difference seperable with the MRS is less than one amu but greater than the tens of MeV required to separate isobars. Figure 5.5 shows that the ion gauge (IG) spectrum provides isobars at many mass values. While these are typically molecular ions, atomic Argon has been unambiguously identified in this spectrum at high resolution (see figure 5.8).

5.3 High resolution mass spectrometry

The dramatic improvement in mass resolving power demonstrated in figure 5.2 is not limited to a certain mass range. The spatial trajectories of ions in an electrostatic field are mass independent; as long as dynamic fields in the trap are set up to produce good initial phase space, the performance of the TITAN MR-ToF should be the same for nearly all ions. This is demonstrated here by comparing the mass resolving power for ^{133}Cs and ^{39}K (figure 5.6). High resolution ToF peaks for ^{133}Cs and mass 40 isobars are shown in figures 5.7 and 5.8. Note that changing from one ion of interest to another is as simple as changing the resolution of a mass spectrum; assuming that ^{40}Ar, ^{40}K, and ^{133}Cs are all present in a sample, switching between the traces shown in figures 5.7 and 5.8 only requires changing a few timings and the RF amplitude in the transport system. No additional tuning of the mass analyzer is required.

The time of flight of a calibrant ion is shown as an offset to the horizontal axis in figures 5.7 and 5.8. This offset time is the difference between the time at which the control

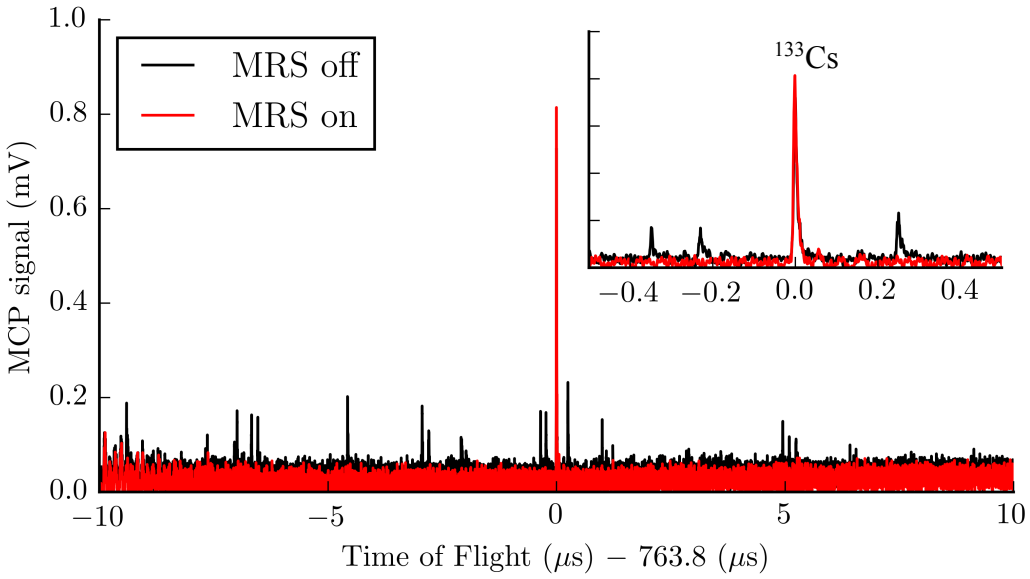

Figure 5.4: Mass spectra of ions from the ion gauges and a thermal ^{133}Cs ion source (see text for details). ^{133}Cs makes 33 turns in the analyzer, and these plots are averaged over 5,000 spectra on the oscilloscope. The black trace shows the complete spectrum including ^{133}Cs and all the ions produced by the ion gauges; the red trace shows the same spectrum after pulsing the MRS during the first 10 turns after an initial time focus shift. The inset details ^{133}Cs and surrounding peaks on the same axes as the larger plot. The fact that all peaks except mass 133 disappear when operating the MRS means that all of the smaller peaks are various other masses; they cannot be identified by their position in this ToF spectrum because most of them make different numbers of turns in the analyzer.

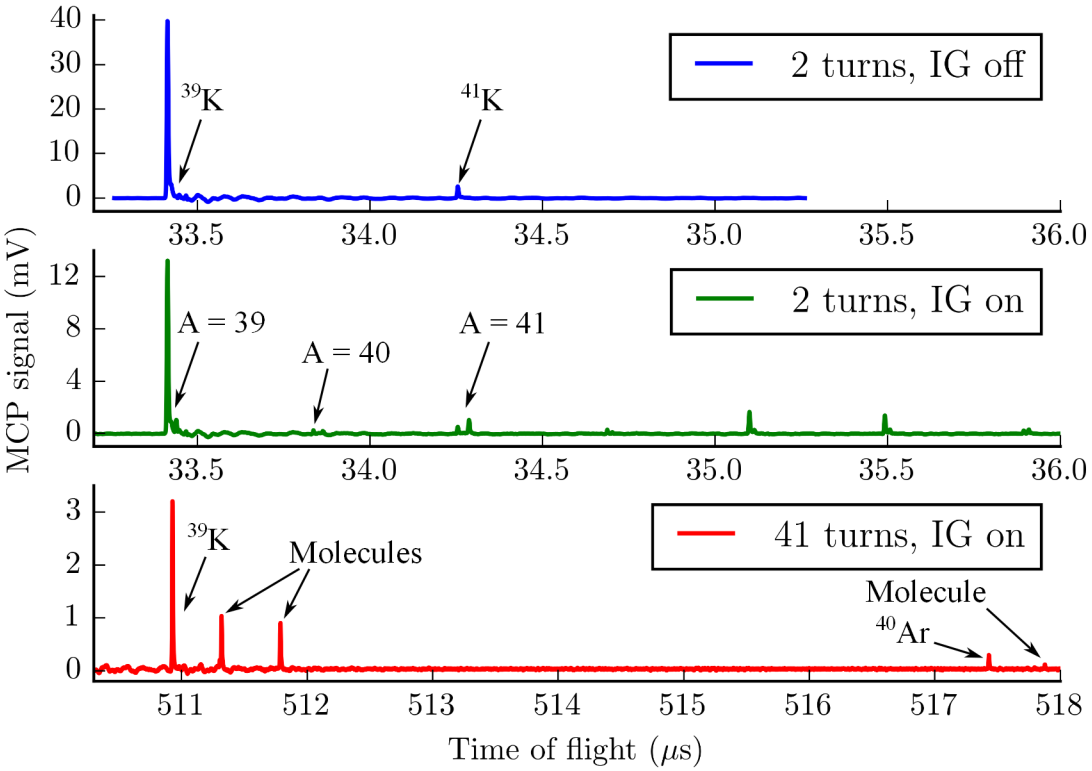

Figure 5.5: Top: mass spectrum from a Potassium thermal ion source. Middle: the same spectrum with the ion gauges on. Sets of isobars are clearly visible at several mass numbers when the gauges are hot. The signal amplitude is smaller in this trace because the bias voltage on the MCP was reduced to compensate for the amount of charge generated by the ion gauges. Bottom: higher resolution measurement of the K/IG mass spectrum. The ^{39}K intensity is smaller again because the ion source power was reduced in order to increase the relative intensity of the IG spectrum. ^{40}Ar is unambiguously identified relative to ^{40}K, which is not visible here (see figure 5.8)

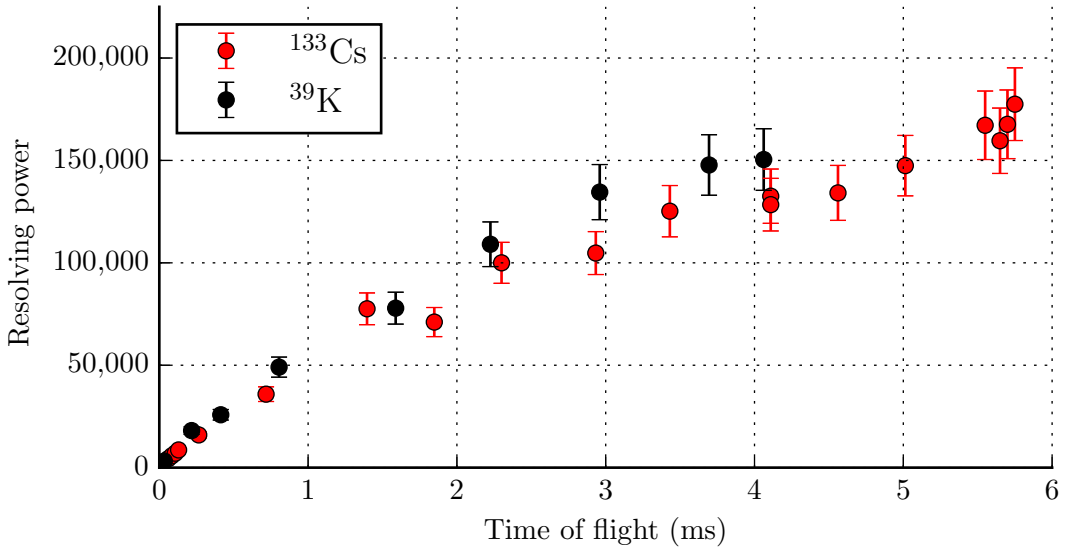

Figure 5.6: Resolving power measured with Potassium and Cesium. The time of flight for Potassium is scaled by $\sqrt{m_{\mathrm{Cs}}/m_{\mathrm{K}}}$ in order to compare the two data sets. 10% error bars are assigned as a conservative estimate of changes due to normal voltage variations.

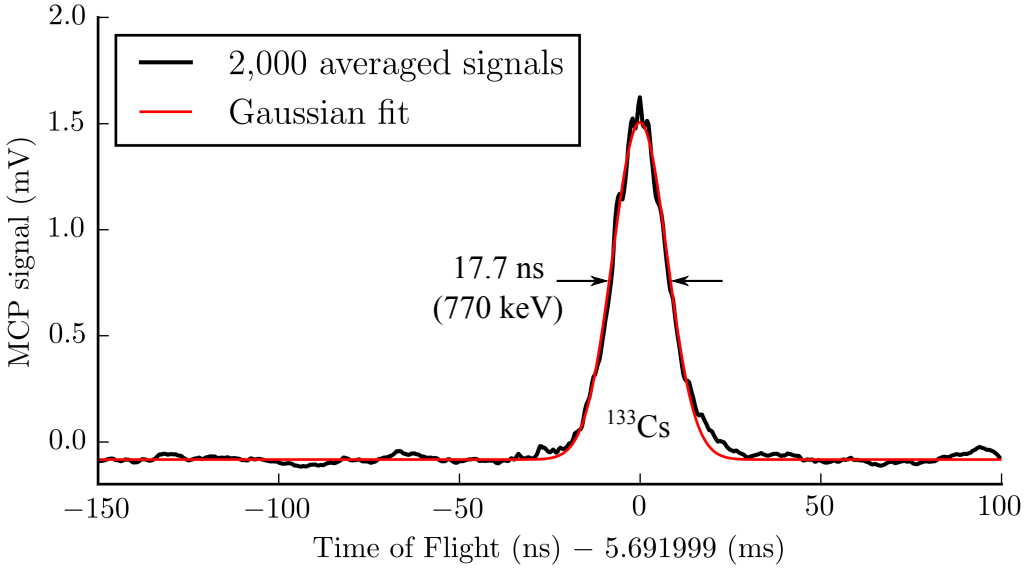

Figure 5.7: A ^{133}Cs time of flight peak after 251 turns in the analyzer. The mass resolving power, $t/(2\Delta t)$, is 161,000.

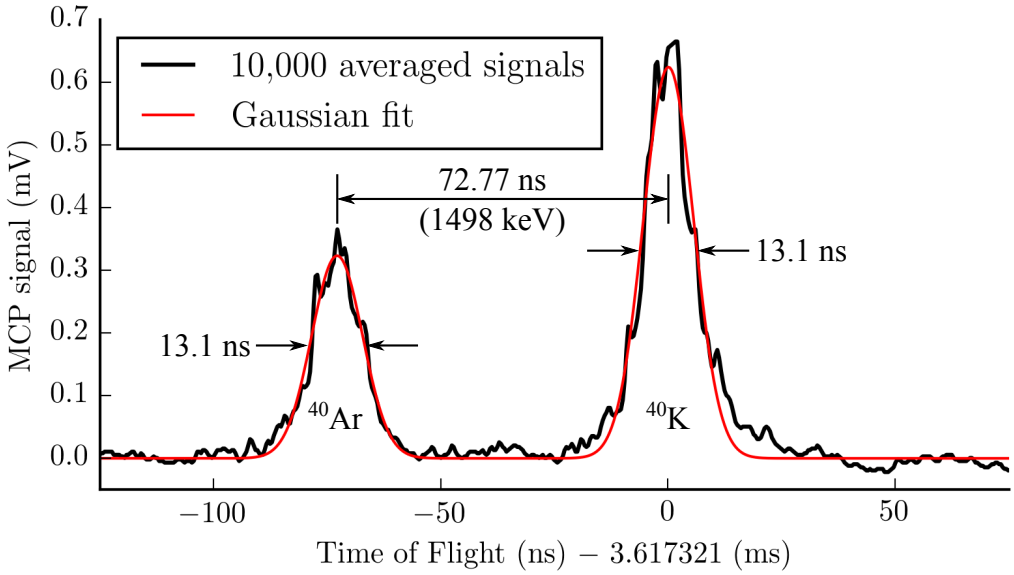

Figure 5.8: A time of flight spectrum showing atomic isobars of mass 40 after 291 turns in the analyzer. The mass resolving power, $t/(2\Delta t)$, is 137,000. This is a high resolution measurement of the same spectrum shown in figure 5.5, however the heating power in the thermal Potassium source is increased to generate ^{40}K at roughly the same intensity as the ion gauges generated ^{40}Ar. ^{40}K is not visible in figure 5.5 because the signal from ^{39}K might damage the MCP at the ion source power used to generate this spectrum. The ^{40}Ar mass value fits well with the literature value (see text), but the peak is also visually identified as an atomic ion because its time of flight is smaller than the time of flight of ^{40}K and it disappears when the ion gauges are switched off.

system triggers the ejection of ions from the trap and the time at which the calibrant ion reaches the detector. This is not the true time of flight; in reality the control electronics must process a request and transmit a signal, and then the switches attached to the trap have to change voltages on the ion optics. That delay between the trigger signal and the time an ion bunch actually starts to move should be included in determination of the mass value as follows:

$$t = c\sqrt{m} + t_s \;\Rightarrow\; m = \left(\frac{t - t_s}{c}\right)^2, \tag{5.1}$$

where c is a conversion constant and t_s is the time required for switching. Since equation 5.1 has two constants, at least two calibration ions are required in addition to the ion of interest. t_s may be calculated from known masses m_1, m_2 and measured times of flight t_1, t_2 for two calibrant ions,

$$t_s = \frac{t_2\sqrt{m_1/m_2} - t_1}{\sqrt{m_1/m_2} - 1}. \tag{5.2}$$

By propagating errors [51] and assuming that the relative uncertainty in the known masses is small compared to the relative uncertainty in the times of flight, we find that the uncertainty in t_s is

$$\Delta t_s = \sqrt{\left(\frac{\Delta t_1}{\sqrt{N_1}(1 - \sqrt{m_1/m_2})}\right)^2 + \left(\frac{\Delta t_2\sqrt{m_1/m_2}}{\sqrt{N_2}(\sqrt{m_1/m_2} - 1)}\right)^2}, \tag{5.3}$$

where Δt_1, Δt_2 are the FWHM of the time of flight peaks for the calibrant ions, and N_1, N_2 are the number of measured ions of each species. To make a mass measurement, an unknown mass m with time of flight t may be calculated relative to a known ion using equation 5.1 for each mass and taking a ratio,

$$m = m_3\left(\frac{t - t_s}{t_3 - t_s}\right)^2. \tag{5.4}$$

m_3 may be one of the two calibrants used to find t_s or it may be a third ion with known mass. Again assuming that the calibrant masses are known much better than the times of flight, the uncertainty in the measured mass is

$$\Delta m = 2m\sqrt{\left(\frac{\Delta t}{\sqrt{N}(t - t_s)}\right)^2 + \left(\frac{\Delta t_3}{\sqrt{N_3}(t_3 - t_s)}\right)^2 + \left(\frac{\Delta t_s}{t_3 - t_s} - \frac{\Delta t_s}{t - t_s}\right)^2}, \tag{5.5}$$

where Δt, Δt_3 are the FWHM of the time of flight peaks for the ion of interest and the calibrant, and N, N_3 are the number of measured ions.

To demonstrate a full time of flight mass measurement, we can calculate t_s from the top trace in figure 5.5 and use figure 5.8 to determine the mass of ^{40}Ar. In that case, t_1, t_2, and t_3 correspond to ^{39}K, ^{41}K, and ^{40}K respectively. Table 5.1 shows the known masses and measured times of flight required to calculate the mass of ^{40}Ar. Known mass values are from the 2012 atomic mass evaluation (AME) [57].

Ion	m [amu]	t [ns]	N
Calibrant 1 (^{39}K)	38.963706487(5)	33410(5)	425
Calibrant 2 (^{41}K)	40.961825258(4)	34252(5)	36
Calibrant 3 (^{40}K)	39.96399817(6)	3617321(13)	508
Ion of interest (^{40}Ar)	Unkown	3617248(13)	261

Table 5.1: Values used to determine the mass of ^{40}Ar from figures 5.5 and 5.8. Masses are from the 2016 AME [57]. Numbers in parentheses are uncertainties in the final digits shown.

The number of detected ions N_i is also required to determine the uncertainty in the mass. In the measurements described here, we typically saw one ion on the detector for about every 13 shots. The rate was chosen to avoid the possibility of multiple ions hitting the detector at once, which would make N_i more difficult to estimate using the averaged peak shape. The peaks used to determine t_s (top trace in figure 5.5) were averaged 6,000 times, representing about 461 ions, and the high resolution peaks near ^{40}K (figure 5.8) were averaged 10,000 times, representing about 769 ions. These numbers are the total number of detected ions in each spectrum; the totals were then distributed among peaks in each spectrum in proportion to the peak areas to find N_i for each species (peak areas were determined with Gaussian fits).

From the first two calibrants in table 5.1 and using equations 5.2 and 5.3, $t_s = 172(33)$ ns. From the third calibrant, equations 5.4 and 5.5, and the calculated value of t_s, the mass of ^{40}Ar should be 39.96238(2) amu. The relative measurement uncertainty is then $5{\cdot}10^{-7}$, or 19 keV absolute, and the relative deviation from the literature value of 39.9623831238(24) amu is $7.8{\cdot}10^{-9}$, or 3 keV.

To further validate the calibration technique, figure 5.9 shows a series of 22 measurements of ^{40}Ar compared to the AME value. These measurements were taken at 3.4 ms time of flight and averaged over 10,000 shots (the last four data points were averaged only 6,000 times). The same value for t_s (172 ns) was used again. The uncertainty in these measurements is larger than in the measurement discussed above because the analyzer was set to a lower turn number. The flight time used here was 3.4 ms instead of 3.6 ms as in figure 5.8, so the resolving power is lower and therefore the uncertainty in the mass and the deviation from the literature value are higher. Figure 5.9 demonstrates that high quality mass spectra are repeatable with the TITAN MR-ToF and that the estimate of N_i discussed above leads to reasonable uncertainties.

For first estimates of mass values, t_s is not required. If t_s is ignored, the unkown mass is determined directly from two ToF centroids (preferably in the same spectrum). The mass of ^{40}Ar could then be estimated from figure 5.8 only. Using the notation from table 5.1, the

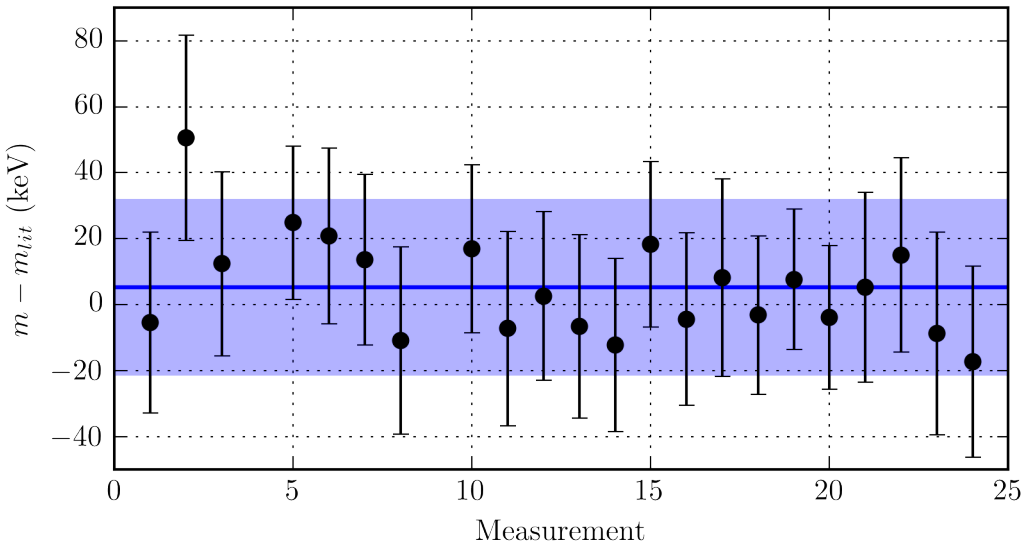

Figure 5.9: 22 mass measurements of ^{40}Ar relative to ^{40}K after a ToF of 3 ms (241 turns). These data were collected over about two hours (see section 5.4). Each mass value is determined using equations 5.4 and 5.5, and the measurements were taken by averaging 10^4 shots on the oscilloscope. The weighted average and average uncertainty in the data points is 5.3 ± 27 keV, indicated in the plot by a blue line with an error band. Missing data points were discarded because either ^{40}Ar or ^{40}K was removed from those spectra for diagnostic purposes; gaps in the series are maintained for comparison with figure 5.10.

mass and uncertainty would be

$$m = m_3 \left(\frac{t}{t_3}\right)^2, \ \Delta m = m\sqrt{\left(\frac{2\Delta t}{t\sqrt{N}}\right)^2 + \left(\frac{2\Delta t_3}{t_1\sqrt{N_3}}\right)^2}. \tag{5.6}$$

In this case the uncertainty and measured value of ^{40}Ar don't change, however it's important to keep track of t_s when comparing data sets because a change in temperature or trigger settings may result in different different values for t_s. It's also important to note that because the calibration is nonlinear, $m \propto (t + t_s)^2$, t_s will have a greater impact on the calibration when calibrants and ions of interest cover a broad mass range.

Based on current performance, regardless of the calibration method, we expect that mass values generated from the TITAN MR-ToF will have a precision better than 1 part per million, resulting in an uncertainty of less than 100 keV for a mass value of 100 amu.

5.4 Stability over time

Any applied voltage has some instability due to noise and temperature drifts at the power supply. In a ToF spectrometer, these voltage instabilities lead to instability in the time of flight of ions. It's best to have a calibrant ion arriving at the detector in the same spectrum as an ion of interest as in figure 5.8 so that there are no voltage drifts between calibration and measurement, however this is not always possible. If calibration spectra are to be taken independently of measurement spectra, one needs to understand how long to wait between calibrations. During online measurements one would like to take as few independent calibration spectra as possible because exotic ions arriving at the spectrometer during calibration are presumably lost, however calibrations must be performed often enough to be sure that measurements are accurate.

Figure 5.10 shows multiple measurements of ^{40}Ar relative to ^{40}K taken with the TITAN MR-ToF, calibrated either with the ^{40}K ions arriving in the same spectrum (as in figure 5.8) or calibrated with the ^{40}K ions collected in the first measurement. The mass values appear stable on time scales of a few minutes. If the system operates at a 50 Hz repetition rate and each spectrum aggregates data from 10^4 shots then a single spectrum takes 3.3 minutes to collect; it would be reasonable in this case to collect two data spectra for each external calibration spectrum.

The drift shown in figure 5.10 has fluctuations on time scales of a few minutes which are due primarily to the precision of the electronics, but it also has a general trend. This trend appears linear in figure 5.10 but in fact it's due to the periodic change in ambient temperature from day to night. We characterized the drift due to the change in temperature using data shown in figure 5.11. The temperature data is taken from a sensor in the ISAC experimental hall, and the change in temperature has an obvious correlation with the drift in the ToF centroid of ^{39}K. From the correlation in figure 5.11, we estimate that the

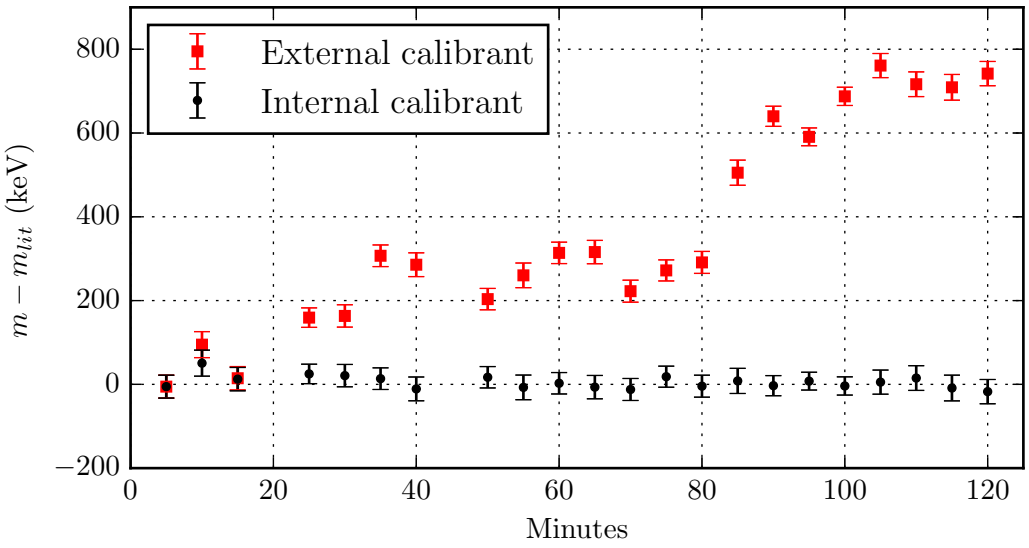

Figure 5.10: 22 mass measurements of ^{40}Ar relative to ^{40}K after a ToF of 3 ms (241 turns). Black points are the same data shown in figure 5.9. With the oscilloscope used to collect these data, it took roughly 5 minutes to average a spectrum, save it, and start a new measurement. The two data sets represent the same spectra calibrated in different ways; "internal" calibration compares each ^{40}Ar peak to the ^{40}K peak in the same spectrum while "external" calibration compares each ^{40}Ar to the ^{40}K peak in the first spectrum.

overall temperature coefficient for time of flight drifts in the MR-ToF is around 8 ppm/K; this coefficient provides a benchmark for future diagnostics or improvements in the power supplies and electronics.

5.5 Relative transmission efficiency

We've attempted to estimate the relative transmission efficiency of ions through the mass analyzer. The efficiency is important when planning an experiment because TRIUMF provides experimenters with rates for available beams; if TITAN is to request an exotic beam then collaborators need to know how many ions will be lost in each optical system in order to estimate how much beam time is required for an experiment. The relative efficiency in the mass analyzer as a function of time of flight at two different analyzer pressures is shown in figure 5.12. In these measurements, the peak area was approximated as the product of the FWHM peak width and the peak amplitude at the MCP.

The important feature to note in figure 5.12 is that the relative efficiency after a couple of milliseconds is approximately doubled when the pressure is reduced by about a factor of two. Since transmission losses at long flight times are roughly proportional to the residual gas pressure and $8{\cdot}10^{-7}$ mbar in the analyzer is typical for the buffer gas pressure we use in the trap, we should be able to double the efficiency again by installing a second turbo

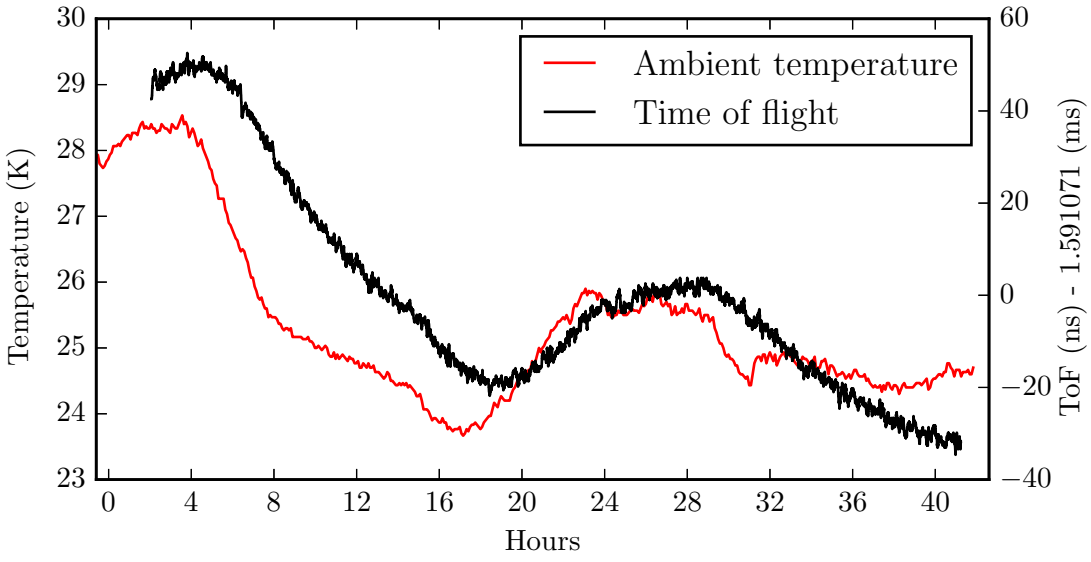

Figure 5.11: Comparison of temperature data (red) collected with a thermometer in the ISAC I experimental hall and the time of flight of a ^{39}K peak (black). The time of flight drifts by about 44 parts per million (ppm) between 6 and 18 hours, and the temperature drifts by around 5.5 K between 5 and 17 hours. The temperature drift coefficient of the time of flight is therefore around 8 ppm/K. This figure is only meant to provide an order of magnitude; it was estimated visually from the plot in order to provide a baseline for comparison after the electronics are temperature regulated.

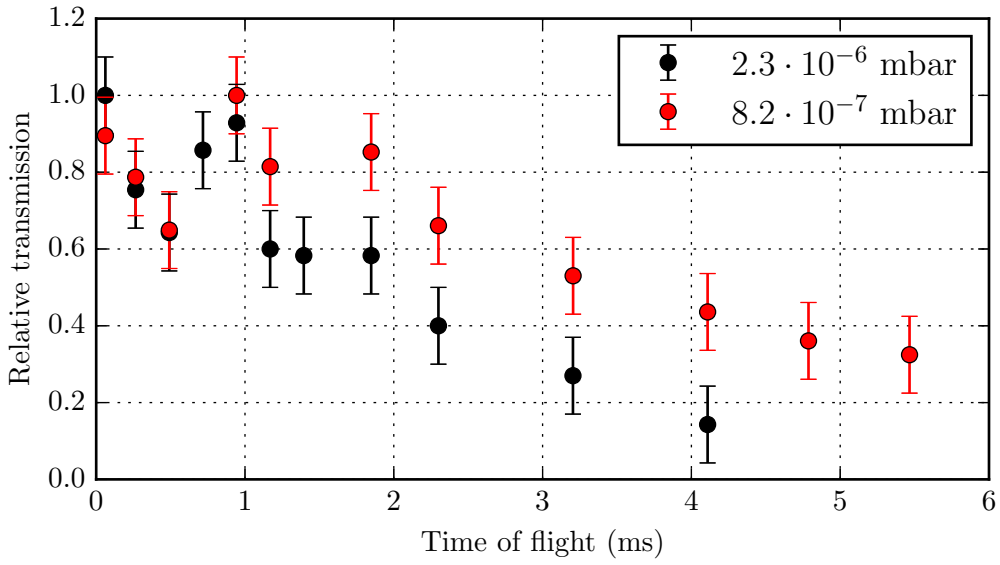

Figure 5.12: Relative efficiency vs. time of flight for ^{133}Cs at two different residual pressures in the mass analyzer. The residual gas is primarily buffer gas which is differentially pumped out of the Paul trap. The efficiency falls off and then peaks near 1 ms time of flight; this pattern is always present but as yet unexplained. It may be due to misalignment of ion optics.

pump near the analyzer. This has been confirmed by replacing the He buffer gas with N_2, which is more massive than He so it cools heavier ions faster and one can achieve the same cooling times with lower buffer gas pressure. We've seen a corresponding increase in the efficiency when using N_2 buffer gas at lower pressures.

5.6 Cooling time

It's important to estimate the minimum cooling time required to thermalize an ion bunch in the Paul trap because the cooling time is a significant fraction of the total time an ion bunch will spend in the MR-ToF. To measure this parameter, we varied the amount of time ^{133}Cs ions were cooled in the trap and compared it to the peak width after 2 turns in the analyzer (see figure 5.13). As a function of cooling time, the peak width decays exponentially to a constant value. The data sets in figure 5.13 were fit with the function

$$\Delta t = e^{-\kappa/\tau + c} + \Delta t_{therm}, \tag{5.7}$$

where Δt is the FWHM time of flight peak width, κ is the cooling time, τ is the characteristic decay time, Δt_{therm} is the ToF width of a thermal ion population, and c is an offset to account for the fact that the peak width is not unity at $\kappa = 0$. The characteristic ^{133}Cs cooling time for He pressures in the high 10^{-3} to low 10^{-2} mbar range is around 160 µs and the ToF peak width of a thermalized ion bunch is 8.3 ns. Data for Potassium is not shown, but cooling times decrease for smaller masses and the smallest measured peak width for ^{39}K is closer to 6 ns. These data suggest that less than two milliseconds of cooling will be required for most ions of interest at TITAN. The cooling time could be decreased by raising the buffer gas pressure in the trap, however this would also increase the residual gas pressure in the analyzer and lead to collisional loss of ions in flight. Ion loss due to residual pressure in the mass analyzer currently sets a lower limit on the cooling time.

5.7 Effect of load resistance in HV switches

As discussed in section 3.8, load resistors are required at the outputs of the high voltage switches in order to protect the switches from high currents. This presents a trade-off in the trap system; the cooled ion cloud is heated in a time dependent field so the switch should be as fast as possible, but faster switching times require higher currents. In order to understand whether the switching time in the trap system was limiting the mass resolving power of the TITAN MR-ToF, we tried several values of the load resistors for the push and pull apertures which apply the kicking field in the trap. The resistors initially installed in the switches were 220 Ω, and the initial switching time for the kicking field was about 160 ns. The switching time was estimated as the rise time between 10% and 90% of the change between the initial and final voltages. We saw significant improvement in system

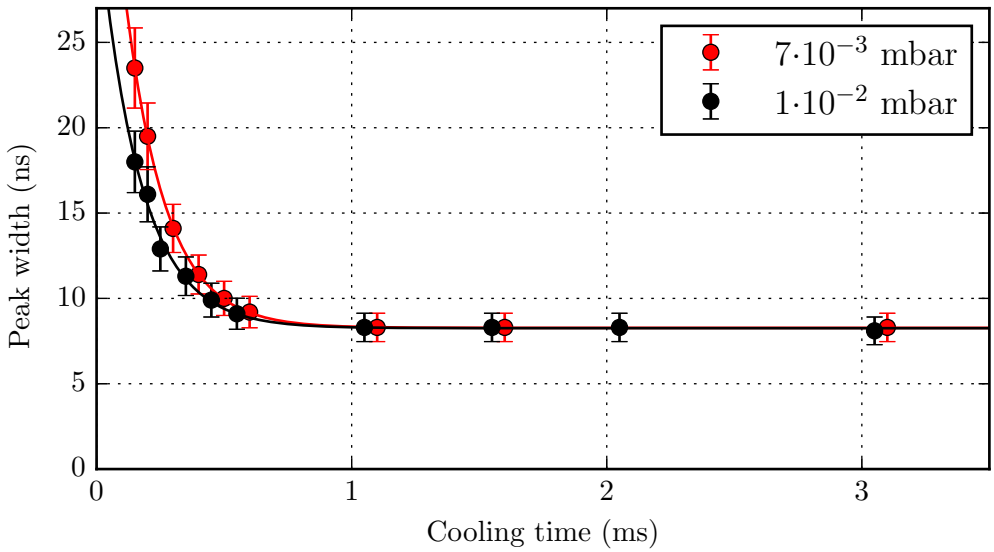

Figure 5.13: Time width (FWHM) of ^{133}Cs vs. cooling time at two different He buffer gas pressures. Ion bunches were flown for 53 µs (2 turns) in the mass analyzer. The cooling time is the amount of time ions were held in the Paul trap before they were kicked into the analyzer. Solid curves are fits to an exponential decay (see text for details); the decay time constants and final peak width are approximately 160 µs and 8.3 ns for both fits.

performance after reducing the load resistors to 73 Ω, which resulted in a switching time of around 90 ns. After changing to 73 Ω, we were able to consistently achieve mass resolving power above 100,000 for the first time (as measured from the ^{133}Cs peak width) and we were able to extend the ^{133}Cs flight time beyond 6 ms without seeing reduction in resolving power. The system performance was also much more stable across different flight times after reducing the load resistance. Results from these tests are shown in figure 5.14. Note that the resolving power shown in these plots is lower than in figure 5.6 because these results were collected at the time we reduced the load resistance; after spending more time with the system we were able to optimize the timings and initial tune to improve overall performance.

Before installing the 73 Ω resistors, we could not increase the flight time by more than about a millisecond without making small adjustments to the analyzer voltages; these tuning adjustments are visible in figure 5.14 when there is a cluster of data points at the same time of flight. With the new smaller load resistors, the system required essentially no adjustment to reach 100,000 resolving power. In the first data series collected with ^{133}Cs after changing the load resistance to 73 Ω, the only time we attempted to adjust voltages was at about 750 ns flight time, and those small adjustments did not give significant improvement in the resolving power.

The right hand plot in figure 5.14 shows the resolving power measured from the ^{39}K peak width at different load resistances. The horizontal axis shows the measured flight time instead of the scaled ToF as shown in figure 5.6. At 220 Ω load resistance, the resolving

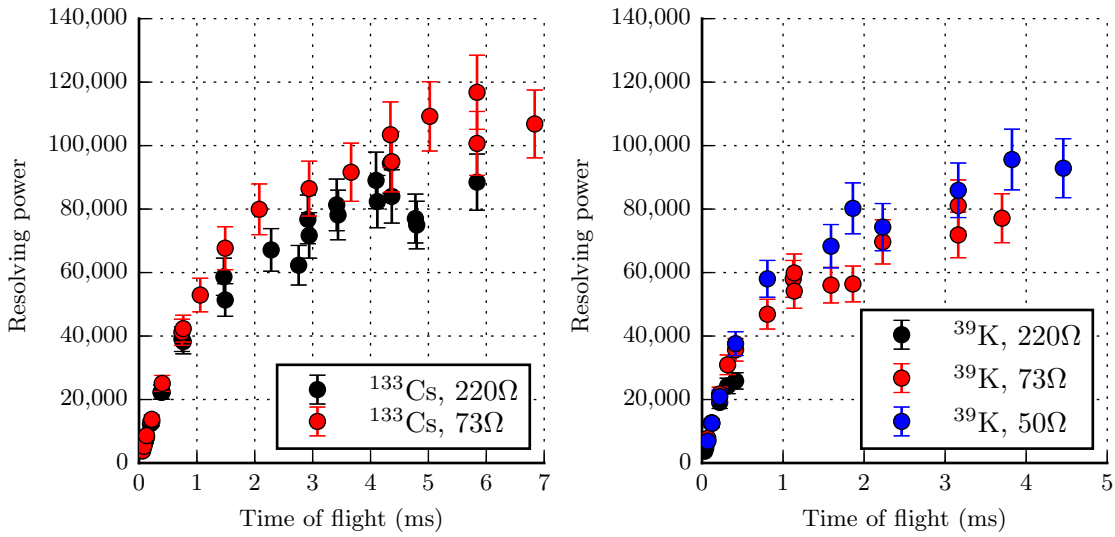

Figure 5.14: Plots of mass resolving power at different times of flight for Caesium (left) and Potassium (right). Steps or sudden variations in the resolution indicate places where voltages were re-tuned to optimize mass resolution. See text for details.

power plateaued at about 500 ns ToF and couldn't be improved beyond that. We saw significant improvement at 73 Ω load resistance, but note that we still had to make regular adjustments to analyzer voltages as we increased the flight time. Since ions of mass 39 fly out of the trap faster than ions of mass 133, a further reduction to 50 Ω load resistance (resulting in faster switching time) produced more consistent performance up to 4.5 ms flight time without adjustments to the tune. After changing to 50 Ω load resistance, there wasn't a significant improvement in the resolving power as measured from the ^{133}Cs peak width.

Reducing the current limit on the switches for the push-pull apertures at the trap resulted in the most significant one-time performance improvement we've seen so far. A simulation afterwards showed that a ^{133}Cs ion starting at rest in the center of the trap flies through the pull aperture about 190 ns after an instantaneous switch to the kicking field, comparable to the 160 ns switching time at 220 Ω load resistance. The rule of thumb we took from these results is that the switching time should be at most half the simulated time for an ion to travel from rest in the trap to the pull aperture after an instantaneous switch.

Chapter 6

Conclusion

Nuclear mass measurements are one of the most precise tests of nuclear theory available. Theorists need precise mass values but they also need masses for many different nuclei, which presents an additional challenge for the experimental community. At ISOL facilities, stable and longer-lived isobars are nearly always produced alongside ions of interest, so specialized methods are required to isolate ions of interest. The Penning trap mass measurement community has recently turned to MR-ToF mass spectrometers for isobar separation, and this thesis has reported on the construction, simulation, and initial commissioning of an MR-ToF spectrometer for the TITAN collaboration at TRIUMF. In addition to these reports, a chapter on theory and design may provide an accessible introduction for students approaching these systems for the first time.

During this work, we demonstrated a mass resolving power of 161,000 was using the FWHM of a ^{133}Cs time of flight peak. We identified two isobars at mass 40 in a single ToF spectrum at a mass resolution of 137,000. These data are presented here with multiple methods for calibration and mass determination. Using these techniques and the data for mass 40 isobars, we determined the mass of ^{40} to be 39.96238(2) amu, in good agreement with the literature value of 39.9623831238(24) [57]. Therefore, if a rare isobar can be identified with the MR-ToF, TITAN may be able to determine its mass to better than one part per million even if it is too short-lived to perform a Penning trap mass measurement.

The TITAN MR-ToF is the product of a collaboration between the TITAN group in Vancouver, Canada and the IONAS group in Giessen, Germany. This work has involved many hands over several years, so a brief account of my contribution to the project is in order. In summer 2013, TITAN provided funding for me to travel to Giessen for a year and assist in the construction of the MR-ToF as an intern. My responsibilities covered prototyping and production of the radio frequency systems discussed in section 3.6 and the cubic RFQ beam switch discussed in section 3.2, as well as development of simulations for the transport section. Particular tasks included the physical layout of the RF generators, design and construction of the in-vacuum circuits separating power supplies from the transport RFQs, and prototyping of the ion optics for the cube. I built the simulations for the transport

section from scratch, beginning with simplified SIMION geometries I produced during the internship. While in Germany, I also assisted with initial assembly of vacuum systems and ion optics for most components of the MR-ToF.

I continued work on the MR-ToF in 2014 after returning to Vancouver in the summer, and I began course work in the Chemistry Department at Simon Fraser University that September. The MR-ToF was shipped to TRIUMF in winter 2014; Christian Jesch, a Ph.D. student from the IONAS group, initialized the system in Vancouver and he demonstrated a mass resolving power of about 50,000 as measured from the ^{133}Cs peak width. I began working on the system full time in summer 2015. Since 2014, I have made substantial improvements to the simulations, including a comprehensive re-write of existing buffer gas code and a multi-layer SIMION geometry for the mass analyzer which enables Monte-Carlo buffer gas cooling in the trap system. I also designed the patch panel discussed in section 3.7 and worked on the implementation with Mel Good (the mechanical engineer for the TITAN group). Operational improvements to the system accelerated dramatically under the supervision of Pascal Reiter, a post-doctoral fellow who arrived in Vancouver at the beginning of 2016; I participated in optimization and data collection until early summer 2016 when I began writing my thesis.

Today, the performance of the TITAN MR-ToF mass spectrometer is comparable to other MR-ToF systems in operation around the world. The nuclear phsyics community employs the highest resolution MR-ToF spectrometers currently available, and these systems typically operate with mass resolving powers between 150,000 and 200,000 [9]. The exception is the IONAS MR-ToF at GSI where typical mass resolving power is substantially higher, and they have achieved a single-spectrum mass resolution of 600,000 [15]. A few publications from authors at Thermo Fisher Scientific indicate that at least one commercial MR-ToF spectrometer is under development for applications in biology and analytical chemistry; the mass resolution for that system was 80,000 in 2014 [22, 25].

6.1 Outlook

My thesis is concerned with the TITAN MR-ToF operated as a mass spectrometer, but the primary objective for this system is to operate as an isobar separator for ultra-high resolution mass spectrometry in the TITAN Penning traps. As discussed in section 2.5, isobar separation in the TITAN MR-ToF is achieved with a mass selective retrapping operation. Major work on retrapping began after I started writing, but isobar separation by mass selective retrapping has been demonstrated at TITAN. Initial results from that work are shown in figure 6.1. Since then, the MR-ToF system has been installed on the TITAN beamline and recommissioned there; the highest resolving power achieved with the system to date is around 250,000.

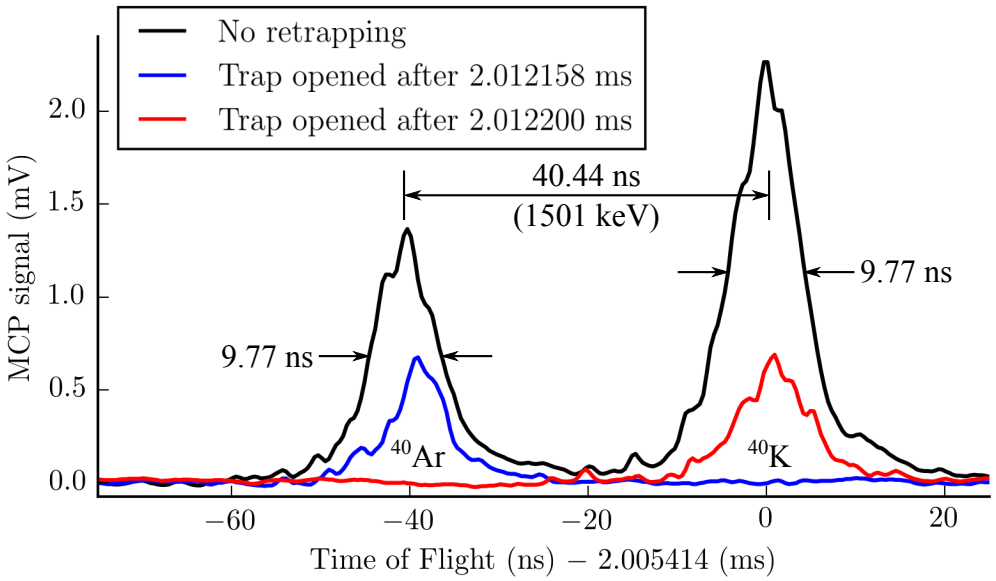

Figure 6.1: First successful isobar separation in the TITAN MR-ToF. The black trace shows a mass spectrum of ^{40}Ar and ^{40}K after 161 turns in the analyzer. The blue and red traces are generated by opening the analyzer mirror closest to the trap, closing the trap at the time ions of interest should turn around, and re-cooling them. After the second cooling stage, a mass spectrum is generated with the captured ion cloud using the same settings as for the black trace in the figure. Overall, the retrapped ions see 1 ms of cooling, 160.5 turns in the mass analyzer, another 1 ms of cooling, and then 161 more turns in the analyzer before hitting the MCP, for a total of about 6 ms in the MR-ToF system.

Bibliography

[1] F. Ames et al. Ion source developments for the production of radioactive isotope beams at triumf. *Rev Sci Instrum*, 89:02B912, 2014. 11

[2] G. Audi et al. The NuBase2012 evaluation of nuclear properties. *Chinese Phys C*, 36(12):1157–1286, 2012. 8

[3] E. Blackmore et al. IEEE milestone ceremony. http://www.triumf.ca/research-program/lectures-conferences/ieee-engineering-milestone-ceremony. 11

[4] K. Blaum. High-accuracy mass spectrometry with stored ions. *Physics Reports*, 425:1–78, 2006. 9

[5] G. Bollen et al. The accuracy of heavy ion mass measurements using time of flight ion cyclotron resonance in a Penning trap. *J Appl Phys*, 68(9):4355–4374, 1990. 13

[6] G. Bollen et al. Resolution of nuclear ground and isomeric states by a penning trap mass spectrometer. *Phys Rev C*, 46(6):R2140–R2143, 1992. 15

[7] P. G. Bricault et al. Rare isotope beams at ISAC—target & ion source systems. *Hyperfine Interactions*, 225:24–49, 2014. 18

[8] A. E. Cameron and D. F. Eggers. An ion "velocitron". *Rev Sci Instrum*, 19(9):605–607, 1948. 4, 5

[9] P. Chauveau et al. PILGRIM, a multi-reflection time-of-flight mass spectrometer for Spiral2-S^3 at GANIL. *Nucl Instrum Meth B*, 376:211–215, 2016. 6, 101

[10] D. Dahl. Simion for the personal computer in reflection. *Int J Mass Spectrom*, 200:3–25, 2000. 62

[11] A. Das and T. Ferbel. *Introduction to Nuclear and Particle Physics*. World Scientific: Hackensack, New Jersey, second edition, 2006. 64

[12] Peter Dawson, editor. *Quadrupole Mass Spectrometry and its Applications*. Elsevier: New York, New York, 1976. 19, 20, 22, 62

[13] H. G. Dehmelt. Radiofrequency spectroscopy of stored ions i: Storage. *Adv At Mol Phys*, 3:53–72, 1967. 22

[14] A. J. Dempster. A new method of positive ray analysis. *Phys Rev*, 11:316–325, 1918. 4

[15] T. Dickel et al. A high-performance multiple-reflection time-of-flight mass spectrometer and isobar separator for the research with exotic nuclei. *Nucl Instrum Meth A*, 777:172–188, 2015. 5, 6, 101

[16] T. Dickel et al. Dynamical time focus shift in multiple-reflection time-of-flight mass spectrometers. *Int J Mass Spectrom*, 412:1–7, 2017. 33

[17] J. Dilling et al. The proposed TITAN facility at ISAC for very precise mass measurements on highly charged short-lived isotopes. *Nucl Instrum Meth B*, 204:492–496, 2003. 11

[18] J. Dilling et al. Mass measurements on highly charged radioactive ions, a new approach to high precision with TITAN. *Int J Mass Spectrom*, 251:198–203, 2006. 11

[19] TRIUMF Science Division. Isac yield database. http://mis.triumf.ca/science/planning/yield/target/U. 16

[20] A. Eddington. The internal constitution of the stars. *Scientific Monthly*, 11(4):297–303, 1920. 9

[21] H. W. Ellis et al. Transport properties of gaseous ions over a wide energy range ii. *Atom Data Nucl Data*, 22:179–217, 1978. 73

[22] A. Giannakopulos. Method of multi-reflecting timeof flight mass spectrometry with spectral peaks arranged in order of ion ejection from the mass spectrometer, 2012. 101

[23] G. Gräff et al. A direct determination of the proton electron mass ratio. *Z Physik A*, 297:35–39, 1980. 11

[24] David Griffiths. *Introduction to Electrodynamics*. Prentice-Hall: Upper Saddle River, New Jersey, third edition, 1999. 62

[25] D. Grinfeld et al. Space-charge effects in an electrostatic multireflection ion trap. *Eur J Mass Spectrom*, 20:131–142, 2014. 101

[26] Ernest Henley and Alejandro Garcia. *Subatomic Physics*. World Scientific: Hackensack, New Jersey, third edition, 2007. 9

[27] Gerald Holton. *Introduction to Concepts and Theories in Physical Science*. Addison-Wesley: Reading, Massachusetts, 1962. 2, 3

[28] W.J. Huang et al. The AME2016 atomic mass evaluation (I). Evaluation of input data; adjustment procedures. *Chinese Phys C*, 41(3):030002, 2017. 7

[29] Damaschin Ioanoviciu. Ion-optical properties of time-of-flight mass spectrometers. *Int J Mass Spectrom*, 206:211–229, 2000. 31

[30] Morio Ishihara. Perfect space and time focusing ion optics for multiturn time of flight mass spectrometers. *Int J Mass Spectrom*, 197:179–189, 2000. 31

[31] Christian Jesch. Bedienungsanleitung zur triggersignalerzeugung mit ni pci-6602 v1.1. Master's thesis, Justus-Liebig-Universitüt Gießen, 2005. 55

[32] Christian Jesch. *Injektions-Ionenfallesystem für ein Multireflektions-Flugzeitmassenspektrometer*. PhD thesis, Justus-Liebig-Universitüt Gießen, 2016. 55

[33] Christian Jesch. *The Multiple-Reflection Time-of-Flight Isobar Separator for TITAN and the Direct Mass Measurements at the FRS Ion Catcher*. PhD thesis, Justus-Liebig-Universitüt Gießen, 2016. 44

[34] Christian Jesch et al. The MR-TOF-MS isobar separator for the TITAN facility at TRIUMF. *Hyperfine Interactions*, 235(1-3):97–106, 2015. 44, 45

[35] E. Jones, T. Oliphant, P. Peterson, et al. SciPy: Open source scientific tools for Python, 2001–. [Online; accessed 2016-06-21]. 22

[36] A. A. Kwiatkowski et al. Titan: An ion trap facility for on-line mass measurement experiments. *Hyperfine Interactions*, 225:143–155, 2014. 11, 14

[37] K. G. Leach et al. Mass measurements of neutron-rich indium isotopes (letter of intent, triumf experiment number s1415loi). https://mis.triumf.ca/science/experiment/view/S1415LOI. 15

[38] Wayne Lippert. *Weiterentwicklung und Anwendung eines Flugzeitmassenspektrometers*. PhD thesis, Justus-Liebig-Universität Giessen, 2016. 6

[39] Louis Lyons. *Statistics for nuclear and particle physics*. Cambridge University Press, 1986. 71, 72

[40] B. A. Marsh. Resonance ionization laser ion sources for on-line isotope separators. *Rev Sci Instrum*, 85:02B923, 2014. 15

[41] E. W. Mcdaniel and E. A. Mason. *The Mobility and Diffusion of Ions in Gases*. John Wiley and Sons, third edition, 1973. 68

[42] W. Paul. Electromagnetic traps for charged and neutral particles. *Rev Mod Phys*, 62(3):531–540, 1990. 22

[43] A. Piechaczek et al. Development of a high resolution isobar separator for study of exotic decays. *Nucl Instrum Meth B*, 266:4510–4514, 2008. 5

[44] W. R. Plaß, T. Dickel, and C. Schedienberger. Multiple-reflection time-of-flight mass spectrometry. *Int J Mass Spectrom*, 349-350:134–144, 2013. 33

[45] William et al. Press. *Numerical Recipes*. Cambridge University Press: New York, New York, third edition, 2007. 65, 72, 110

[46] S. Robertson and Z. Sternovsky. Monte carlo model of ion mobility and diffusion for low and high electric fields. *Phys Rev E*, 67:046405, 2003. 75

[47] T. Sakurai et al. Ion optics for time-of-flight mass spectrometers with multiple symmetry. *Int J Mass Spectrom*, 63:273–287, 1985. 31

[48] P. Schury et al. A multi-reflection time-of-flight mass spectrograph for short-lived and super-heavy nuclei. *Nucl Instrum Meth B*, 317:537–543, 2013. 5

[49] M. Smith et al. First penning-trap mass measurement in the millisecond half-life range: the exotic halo nucleus ^{11}Li. *Phys Rev Lett*, 101:202501, 2008. 14

[50] Mathew Smith. A square-wave-driven radiofrequency quadrupole cooler and buncher for titan. Master's thesis, University of British Columbia, 2005. 68, 70, 73, 110

[51] John R. Taylor. *An Introduction to Error Analysis*. University Science Books: Sausalito, California, second edition, 1997. 91

[52] J. J. Thomson. J.J. Thomson - Nobel Lecture: Carriers of Negative Electricity. http://www.nobelprize.org/nobel_prizes/physics/laureates/1906/thomson-lecture.html. 3

[53] J. J. Thomson. Bakerian lecture: Rays of positive electricity. *P R Soc Lond A A-Conta*, 89(607):1–20, 1913. 2, 3, 4

[54] J. J. Thomson et al. Discussion on isotopes. *P R Soc Lond A A-Conta*, 99(697):87–104, 1921. 2, 4, 7

[55] A. N. Verenchikov and M. I. Yavor. Multi-reflecting mass spectrometer. US Patent 20160035558, 2016. 26

[56] L. A. Viehland and E. A. Mason. Transport properties of gaseous ions over a wide energy range iv. *Atom Data Nucl Data*, 60:37–95, 1995. 73

[57] M. Wang et al. The AME2016 atomic mass evaluation (II) - Tables, graphs and references. *Chinese Phys C*, 41(3):030003, 2017. 7, 16, 91, 92, 100

[58] F. Wienholtz et al. Masses of exotic calcium isotopes pin down nuclear forces. *Nature*, 498:346–349, 2013. 5, 7

[59] W. C. Wiley and I. H. McLaren. Time-of-flight mass spectrometer with improved resolution. *Rev Sci Instrum*, 26(12):1150–1157, 1955. 29, 31

[60] Robert Wolf. *First on-line applications of a multi-reflection time-of-flight mass separator at ISOLTRAP and the mass measurement of ^{82}Zn*. PhD thesis, Ernst-Moritz-Arndt-Universität Greifswald, 2013. 5

[61] H. Wollnik. *Optics of Charged Particles*. Academic Press: San Diego, California, 1987. 5, 25

[62] H. Wollnik and M. Przewloka. Time-of-flight mass spectrometers with multiply reflected ion trajectories. *Int J Mass Spectrom*, 96:267–274, 1990. 6

[63] M. Yavor. *Optics of Charged Particle Analyzers*, volume 157 of *Advances in Imaging and Electron Physics*. Academic Press: San Diego, California, 2009. 5, 19, 25, 26, 41

[64] M. Yavor et al. Ion-optical design of a high-performance multiple-reflection time-of-flight mass spectrometer and isobar separator. *Int J Mass Spectrom*, 381-382:1–9, 2015. 26

[65] Murat Yildrim et al. Designing multi-field linear time-of-flight mass spectrometers with higher-order space focusing. *Int J Mass Spectrom*, 291:1–12, 2010. 31

Appendix A

Implementation of buffer gas collision code

This appendix provides example code to implement buffer gas simulations in SIMION.

A.1 Estimation of maximum impact parameter

The maximum impact parameters for Li^+ and Cs^+ ions in He were estimated as a function of collision energy using a Python 2.7 script. The entire script is shown below with documentation in comments (italics). Provided all the dependencies are available, this code will run verbatim; the script takes about a minute to execute on a 1.2 GHz dual-core laptop.

```
# Python dependencies
import numpy as np
import matplotlib.pyplot as plt
import matplotlib.gridspec as gridspec
from numpy import exp as e
from scipy.optimize import brentq
from scipy.optimize import curve_fit
from scipy.integrate import quad

# minimum scattering angles for calculating the
# maximum impact parameter (bmax)
tMinLi = 0.001
tMinCs = 0.00022

# maximum collision energy for fitting bmax
eMaxLi = 137
eMaxCs = 100
```

```
# interaction potential for lithium ions in helium (Eq 4.12)
def VLi(r):
    return  27.2 * (
        23.2 * e(-43.8 * r) +
        8.74E-9 * e(-32.9 * r) / np.power(r, 6) -
        5.98E-6 * e(-0.116 * r) / np.power(r, 4) +
        0.0529 * (23 * e(-62.5 * r) - 6.44*e(-32 * r))/r -
        29.3 * e(-59.5 * r)
    )

# interaction potential for cesium ions in helium (Eq 4.13)
def VCs(r):
    return  0.0108527*(
        0.000346014 / np.power(r, 8) -
        0.00241738 / np.power(r, 6) -
        0.0221772 / np.power(r, 4)
    )

# these functions implement Eq 4.3 for lithium and cesium
def fLi(r, b, E):
    return 1 - np.power(b, 2) / np.power(r, 2) - VLi(r) / E
def fCs(r, b, E):
    return 1 - np.power(b, 2) / np.power(r, 2) - VCs(r) / E

# this function returns the largest root of another function
# using Numerical Recipies a root finding algorithm defined
# in the Scientific Python libraries
def bigRoot(func, pars):
    try:
        root = brentq(func, 0.01, 4, pars)
    except ValueError:
        s = 0.1
        while True:
            try:
                root = brentq(func, 4-s, 4, pars)
                break
            except ValueError:
                s += 0.08
                continue
    return root

# this is the integrand in Eq 4.2
def integrand(r, b, E, f):
    return 1 / (np.sqrt(f(r, b, E)) * np.power(r, 2))

# this function implements Eq 4.2
def theta(b, E, f):
    # find lower limit of integration
    rm = bigRoot(f, (b, E))
    # calculate the integral using a Numerical Recipies
    # algorithm defined in the SciPy libraries
    i = quad(integrand, rm, np.inf, (b, E, f))
    return np.pi - 2 * b * i[0]
```

```
# roots of this function are intersections between the plots
# in figure 4.5 and a horizontal line defined by the constant
# angle "t" in the function
def toZero(b, E, f, t):
     return theta(b, E, f) + t

# functional form of B(E) for fitting (this is Eq 4.15)
def toFit(e, f, g, h):
    return f / np.power(e, g) - h

# these arrays are the domain over which the maximum impact
# paramtere will be fit (the domain of figure 4.6)
eFitCs = np.linspace(0.1, 225, 1000)
eFitLi = np.linspace(0.1, 225, 1000)

# the following arrays define the energy domain over which the
# maximum impact parameter will be calculated
energiesCs = np.linspace(1, eMaxCs, 15)
energiesLi = np.concatenate([np.linspace(1, 20, 10), np.linspace(23, eMaxLi,
     10)])

# define two empty arrays and then fill them with values of
# the maximum impact parameters at the energies defined in the
# last step
MaxImpactCs = np.zeros(len(energiesCs))
MaxImpactLi = np.zeros(len(energiesLi))
for i in range(len(energiesCs)):
    MaxImpactCs[i] = bigRoot(toZero, (energiesCs[i], fCs, tMinCs))
for i in range(len(energiesLi)):
    MaxImpactLi[i] = bigRoot(toZero, (energiesLi[i], fLi, tMinLi))

# fit B(E) (Eq 4.15) to the maximum impact parameters calculated
# in the last step using the SciPy curve_fit method.
CsFit = curve_fit(toFit, energiesCs, MaxImpactCs, maxfev=2000)
LiFit = curve_fit(toFit, energiesLi, MaxImpactLi, maxfev=2000)

# print the fit parameters (output shown in Eqs 4.16 and 4.17)
print 'Cs fit parameters', CsFit[0]
print 'Li fit parameters', LiFit[0]

# generate figure 4.6, save it as MaxImpacts.png
fig = plt.figure(figsize=(5, 2.5))
ax = fig.gca()
ax.scatter(energiesCs, MaxImpactCs, c='k', s=12, marker='o', label='Cs',
    zorder=10)
ax.plot(eFitCs, toFit(eFitCs, *CsFit[0]), c='k', lw=0.5, label='_nolegend_')
ax.scatter(energiesLi, MaxImpactLi, c='w', s=12, marker='o', lw=0.5, label='
    Li', zorder=10)
ax.plot(eFitLi, toFit(eFitLi, *LiFit[0]), c='k', lw=0.5, label='_nolegend_')
ax.set_ylim((0, 2))
ax.set_xlim((0, 225))
ax.set_ylabel('B(E) (nm)')
ax.set_xlabel('E (eV)')
ax.legend(scatterpoints=1)
plt.savefig('MaxImpacts.png', bbox_inches='tight', dpi=300)
```

A.2 The collision integral

For every collision, the simulation code has to find the largest root of equation 4.3 to get the minimum distance between the two particles and then perform the integration in equation 4.2 to find the scattering angle. Root finding and integration are computationally intensive operations, so they're implemented in C++ for the simulations in this work. The C++ code for these two operations was originally compiled by Matt Smith for his master's work [50], however the version of the code which I received in 2014 did not compile as written, it didn't have any documentation, and Andrew Finlay (another TITAN student) and myself later found several errors in that code. The C++ library compiled for this project is therefore not completely original, however the code presented below has been significantly modified from its original form.

The functions `fx`, `dfdx`, and `integrand` (representing equation 4.3, the derivative of equation 4.3, and the integrand in equation 4.2 respectively) do most of the work in this library. While there were a few errors in these functions which had to be fixed, their structure is the same as intended in the original code by Smith. It's especially worth noting that the variable substitution $r \to r_m/\sin(x)$ is a clever way to make both limits of integration finite in equation 4.2, and that was part of the original C++ code. The interface between this library and Lua is provided by Dave Manura in the example extension `simple.cpp` which is distributed with SIMION.

Finally, I'm not well versed in C++ and I had several problems getting this code to compile on different systems. To simplify the process, I placed all header files outside the standard library in the same directory as this code; `lua.h`, `lualib.h`, `luaxlib.h`, and `remote.h` are all distributed with SIMION 8.1 (the lua headers are included with any Lua distribution), and the rest of the non-standard `#include` statements refer to code from Numerical Recipes [45]. In addition to the dependencies listed in the code, the library `lua51.lib` (a standard Lua library also distributed with SIMION) is required. If all the dependencies are in one folder with the source code below, the code may be compiled with any C++ compiler; I used the Windows SDK compiler with the command line `cl <source filename> /O2 lua51.lib`. The source code is provided below with documentation in italicized comments.

```
// Headers from the standard C++ library
#include <iostream>
#include <iomanip>
#include <math.h>
#include <cmath>
// This definition is required for the interface to Lua, and the
// following headers are standard Lua libraries
#define DLLEXPORT extern "C" __declspec(dllexport)
extern "C" {
#include "lua.h"
#include "lualib.h"
#include "lauxlib.h"
}
// This is a header written by Dave Manura and distributed with SIMION
#include "remote.h"
// This is a header distributed with Numerical Recipies
#include "nr.h"
```

```
/* These are Numerical Recipies 2nd edition routines which are modified
   for functions of multiple scalar arguments. The original Numerical
   Recipies all assume that the function to search, integrate, etc.
   is a function of a single scalar variable. Rather than vectorize
   the functions fx, dfdx, and integrand below so that they take a
   single argument with multiple scalars, the NR routines were
   modified to take multiple arguments. The order of arguments is
   usually the same as in the NR code with the extra arguments
   inserted at the end of the function calls. */
#include "rtsafe2.cpp"  // modified from the NR2ed routine rtsafe
#include "zbrak2.cpp"   // modified from the NR2ed routine zbrak
#include "qromo2.cpp"   // modified from the NR2ed routine qromo
#include "midpnt2.cpp"  // modified from the NR2ed routine midpnt
#include "polint.cpp"   // this is a verbatim NR2ed routine

// This function returns the value of the left hand side of Eq. 4.3.
DP fx(const DP r, const DP E, const DP b) {
  return (1 - b * b/pow(r, 2) - 0.010852713178294573 * (
      0.00034601412071297636 / pow(r, 8) -
      0.0024173801189985495 / pow(r, 6) -
      0.02217718185984001/pow(r, 4)
  ) / E);
}

/* This function is the x derivative of the left hand side of Eq. 4.3
   it takes some arguments by reference rather than returning a value
   because of the structure of the Numerical Recipies routines. */
void dfdx(const DP r, DP &fn, DP &df, const DP E, const DP b) {
  fn = (1 - b * b / pow(r, 2) - 0.010852713178294573 * (
      0.00034601412071297636 / pow(r, 8) -
      0.0024173801189985495 / pow(r, 6) -
      0.02217718185984001 / pow(r, 4)
  ) / E);
  df = ((2 * b * b) / pow(r, 3) + 0.010852713178294573 * (
      0.002768112965703811 / pow(r, 9) -
      0.014504280713991298 / pow(r, 7) -
      0.08870872743936004 / pow(r, 5)
  ) / E);
}

// This function substitutes rmin/sin(x) for r in equation 4.2 and then
// returns the value of the integrand at the point x.
DP integrand(const DP x, const DP E, const DP b, const DP rmin) {
  double radicand = 1 - b * b / pow(rmin / sin(x), 2) - 0.010852713178294573
      * (
      0.00034601412071297636 / pow(rmin / sin(x), 8) -
      0.0024173801189985495 / pow(rmin / sin(x), 6) -
      0.02217718185984001 / pow(rmin / sin(x), 4)
  ) / E;
  if (radicand <= 0) {
    return 0;
  } else {
   return (double) (cos(x) / (rmin * sqrt(radicand)));
  }
}
```

```
/* As per D Manura in simple.cpp: "This is a C function exposed to Lua.
   Lua requires such functions to have this prototype." This function
   does the integration for the scattering angle (Eq. 4.2) and returns
   the result. */
static int result(lua_State *L) {
  /* The next three variables are provided by the code which calls this
     function. b is the impact parameter for this collision, E is the
     kinetic energy available in the collision, and bmax is the maximum
     impact parameter relevant to this collision energy
     (see sec. 4.1). */
  double b = luaL_checknumber(L, 1);
  double E = luaL_checknumber(L, 2);
  double bmax = luaL_checknumber(L, 3);

  const int NBMAX = 3;  // number of possible roots
  const int N = 1000;   // number of subintervals used to bracket roots
  int nb = NBMAX;       // variable number of roots to pass to zbrak
  Vec_DP xb1(NBMAX);    // vector to store minima of root brackets
  Vec_DP xb2(NBMAX);    // vector to store maxima of root brackets
  DP xacc;              // resolution of root search
  DP rmin;              // value of the largest root of Eq. 4.3
  double integral;      // result of the integration

  /* zbrak2 slices fx into multiple subintervals and looks for a change
     of sign in each interval; if it sees a sign change then it puts
     the edges of the subinterval into the bracket vectors. E and b are
     additional arguments, the rest of the arguments are the same as in
     the zbrak routine from Press et. al. */
  NR::zbrak2(fx, 0.0, bmax, N, xb1, xb2, nb, E, b);

  // The resolution of the root search is 10e-8 times smaller than
  // the subinterval used to bracket the largest root
  xacc = (1.0e-8) * (xb1[nb - 1] + xb2[nb - 1]) / 2.0;

  /* rtsafe2 finds a root of dfdx within a given interval and returns
     the value; the interval here is the bracket around the largest
     root found by zbrak2. E and b are additional arguments, the rest of
     the arguments are the same as in the rtsafe routine from
     Press et. al. */
  rmin = NR::rtsafe2(dfdx, xb1[nb - 1], xb2[nb - 1], xacc, E, b);

  /* If the largest root is at r = 0 then set the total integral to
     zero, otherwise use qromo2 to perform the integration in Eq. 4.2.
     The limits of integration are (0, pi/2) rather than
     (rmin, infinity) because of the change of variables from r to
     rmin/sin(x). */
  if(rmin == 0.0) {
    integral = 0;
  } else {
    integral = NR::qromo2(integrand, 0.0, 3.141592653589793238 / 2, NR::
        midpnt2, E, b, rmin);
  }
```

```
  // This puts the return value on the Lua stack.
  lua_pushnumber(L, integral);
  // The return value tells Lua how many values were returned.
  return 1;
}

/* As per D Manura in simple.cpp: "List of C++ functions to
   register in Lua. This must be terminated with {NULL, NULL}." */
struct luaL_reg simplelib[] = {
  {"result", result},
  {NULL, NULL}
};

/* As per D Manura in simple.cpp: "When Lua loads this module, it calls
   this function to do its initialization. It must have the name
   'luaopen_x' where 'x' is the name of the module loading by require
   'x' in Lua. The DLLEXPORT exports this function in the DLL so that
   its visible to outsiders (i.e. Lua)." Note that this code was in a
   file called "cshe.cpp" and it's possible that if your source code is
   in a file with a different name then you might need to change the
   "cshe" bits below to match the filename. */
DLLEXPORT int luaopen_cshe(lua_State *L) {
  /* As per D Manura in simple.cpp: "This sets up the module and
     registers the C++ functions."  */
  luaL_newmetatable(L, "my simple module");
  luaL_openlib(L, "cshe", simplelib, 0);
  return 1;
}
```

A.3 Buffer gas code

SIMION user programs are written in Lua and they are implemented through a set of functions called program segments. These functions are called by SIMION at various points throughout a fourth order Rung-Kutta integration of the equations of motion for each ion. Code used to implement buffer gas collisions in the SIMION program segments is provided in this section; additional details about user programs are available in the SIMION user manual. Lua is a scripting language that allows some flexibility when defining variables, but for clarity I define all new variables in this user program with `local` scope at the beginning of the script. Several variables in this code (such as `ion_vx_mm`) are not declared before they're referenced; these are SIMION variables which are already defined when the program segments are called. Note also that SIMION variables defining speeds are in units of mm/µs.

Once the C++ collision integral discussed in the previous section has been compiled into a library, the code below may be used verbatim as a workbench program for a SIMION run. In that case every ion will see buffer gas at all time steps. This code is written in Lua 5.1 and it's documented in comments (italics). Note that there is a structure to some of the variable names in this script: variables beginning with `v` are speeds of a particle in the reference frame of the simulation coordinate system, variables beginning with `w` are speeds in the center of momentum frame of a given collision, variables ending in `i` refer to properties of the ion, and variables ending in `n` refer to properties of a neutral particle.

```
-- tell SIMION this is a user program and load a SIMION library
simion.workbench_program()
local stats = require 'simionx.Statistics'

local p = 1              -- buffer gas pressure [mbar]
local T = 300            -- buffer gas temperature [K]
local kb = 8.617385E-5   -- Boltzmann constant [eV/K]
local c = 2.997925E8     -- speed of light [m/s]
local e = 1.602177E-19   -- electron charge [C]
local eVamu = 931.502E6  -- conversion from amu to eV/c^2
local mn = 3.756747E9    -- mass of neutral [eV/c^2]
local mi = 0             -- mass of ion [eV/c^2] (defined later)
local u = 0              -- reduced mass of ion-neutral pair [eV/c^2]
-- standard deviation of a 1D Max-Boltz speed distribution:
local MBstd = c * sqrt(kb*T/mn)
-- number density of neutral buffer gas [1/m^3]:
local N = p*100/(kb*T*e)
local tStep = 1 -- requested length of next time step [us]
local rate = 0  -- rate of ion-neutral collisions

--[[ the next two declarations cache a constant and a function so the
script doesn't have to index a module every time the values are
called --]]
local pi = math.pi
local gR = stats.gaussian_rand

--[[ The integral in the scattering angle (Eq 4.2) is implemented in
C++ so it runs faster. The relevant function is cshe.result(b, E, B),
where b is the impact parameter for the collision, E is the collision
energy, and B is the maximum possible impact parameter at this
energy. The function is cached so the C++ library isn't indexed at
every call. --]]
require ("cshe")
integral = cshe.result

--[[ bmaximum calculates the maximum impact parameter for a given
collision energy (Eq 4.16).
input:   center of momentum collision energy [eV]
output:  maximum impact parameter [nm] --]]
function bmaximum(E)
    local b = (1.48456 / pow(E, 0.196523)) - 0.196341
    return(b)
end

-- segment.initialize is a SIMION segment called once per ion before
-- running the simulation
function segment.initialize()

    --[[ ideally the ion mass would be defined above but it's best to
    declare it here because of the structure of the SIMION
    segments --]]
    mi = ion_mass*eVamu     -- mass of ion [eV/c^2]
    u = mn*mi/(mi+mn)       -- reduced mass [eV/c^2]

-- done with segment.initialize
end
```

```
-- segment.tstep_adjust is called once per ion per time step; it's
-- called just before the Runge-Kutta integration.
function segment.tstep_adjust()

    --[[ tStep is initialized to 1 [us] but it's recalculated in the
    next segment after every timestep for each ion. ion_time_step is
    the SIMION variable storing the current Rung-Kutta timestep. --]]
    if tStep < ion_time_step then
       ion_time_step = tStep
    end

-- done with segment.tstep_adjust
end

-- segment.other_actions is called once per ion per time step; it's
-- called after all other calculations.
function segment.other_actions()

    -- Get ion velocity from SIMION internal variables, converting
    -- from [mm/us] to [m/s]
    vxi = ion_vx_mm * 1000
    vyi = ion_vy_mm * 1000
    vzi = ion_vz_mm * 1000
    vi = sqrt(vxi*vxi + vyi*vyi + vzi*vzi)

    -- Get 3D, Maxwell-Boltzmann distributed velocity for a neutral
    -- particle (Eq 4.8) using the normal distribution cached at the
    -- beginning.
    vxn = gR()*MBstd
    vyn = gR()*MBstd
    vzn = gR()*MBstd

    -- Set relative speed
    vrel = sqrt((vxi-vxn)*(vxi-vxn) + (vyi-vyn)*(vyi-vyn) + (vzi-vzn)*(vzi-
        vzn))

    -- Define parameters for collision rate calculation
    E = 0.5*u*(vrel/c)*(vrel/c) -- collision energy [eV] (Eq 4.1)
    B = bmaximum(E)         -- bmax at this energy [nm] (Eq 4.16)
    Xsec = pi*B*B*1e-18     -- max collision cross section [m^2]
    rate = N*vrel*Xsec      -- collision rate [1/s] (Eq 4.19)

    --[[ As a rule of thumb, the time step should stay close to 10
    steps per collision for reasonable results without slowing
    things down too much. The value of dt is the current number of
    microseconds between collisions divided by 10. A shorter time
    step (larger division factor in dt) does appear to increase the
    accuracy of this simulation compared to mobility data.--]]
    dt = (1e6/rate)/10      -- (microseconds between collisions)/10

    --[[ update the value used to set the time step in
    segment.tstep_adjust; tStep stays the same if it's shorter
    than dt --]]
    tStep = min(dt, tStep)
```

```
--[[ This is the Monte Carlo decision (see section 4.2);
rate*time is the collision probability, and if it's greater than
a random number then the program simulates a collision between
an ion and a neutral particle. Testing against a random number
is only valid when ion_time_step is sufficiently small;
"sufficient" being determined by comparison with mobility
data. --]]
if rate*ion_time_step*1e-6 > simion.rand() then

    -- Set center of mass velocity in the simulation frame
    vxcm = (vxn*mn + vxi*mi)/(mi + mn)
    vycm = (vyn*mn + vyi*mi)/(mi + mn)
    vzcm = (vzn*mn + vzi*mi)/(mi + mn)

    -- Now boost the ion velocity into a center of momentum
    -- reference frame.
    wxi = vxi - vxcm
    wyi = vyi - vycm
    wzi = vzi - vzcm
    wi = sqrt(wxi*wxi + wyi*wyi + wzi*wzi)

    --[[ Without additional calculation or loss of
    generality, the program assumes that the center of
    momentum coordinates are aligned such that the z
    axis is parallel to the particle velocities. This
    c.o.m. reference frame is not parallel to the
    simulation axes. (See section 4.1) --]]

    -- Set random impact parameter (Eq 4.20)
    b = B*sqrt(simion.rand())

    -- Calculate the longitudinal scattering angle (Eq 4.2)
    theta = pi - 2*b*integral(b, E, B)

    -- Set random transverse scattering angle
    tau = 2*pi*simion.rand()

    -- Set scattered ion velocities in the c.o.m. frame
    -- (Eq 4.4)
    wxs = wi*cos(tau)*sin(theta)
    wys = wi*sin(tau)*sin(theta)
    wzs = wi*cos(theta)

    --[[ Now rotate to a new center of momentum frame whose
    axes are parallel to the reference frame of the
    simulation. The rotation angles are defined using
    the fact that we previously assumed that wi was a
    vector parallel to the original c.o.m. z axis. --]]

    -- Set rotation angles (Eqs 4.5)
    alpha = acos(wzi/wi)
    beta = atan2(wyi, wxi)
```

```
        -- Rotate scattered velocity into c.o.m. frame parallel
        -- to the reference frame of the simulation.
        vxi = wxs*cos(alpha)*cos(beta) - wys*sin(alpha) + wzs*sin(alpha)*cos
            (beta)
        vyi = wxs*cos(alpha)*sin(beta) + wys*cos(alpha) + wzs*sin(alpha)*sin
            (beta)
        vzi = -wxs*sin(alpha) + wzs*cos(alpha)

        -- Boost back to the reference frame of the simulation
        -- (Eq 4.7)
        vxi = vxi + vxcm
        vyi = vyi + vycm
        vzi = vzi + vzcm

        -- Convert from [m/s] to [mm/us] and update SIMION
        -- internal velocity variables
        ion_vx_mm = vxi / 1000
        ion_vy_mm = vyi / 1000
        ion_vz_mm = vzi / 1000
    -- done with Monte Carlo ion-neutral collision
    end
-- done with other_actions segment
end
```